CORA Cork Open Research Archive
Cartlann Taighde Oscailte Chorcaí

Title	SOA enhanced optical line terminal for future optical access network
Authors	Jamali, Fariba
Publication date	2026-02-28
Original Citation	Jamali, F. 2026. SOA enhanced optical line terminal for future optical access network. PhD Thesis, University College Cork.
Type of publication	Doctoral thesis
Rights	© 2026, Fariba Jamali. - https://creativecommons.org/licenses/by-nc-nd/4.0/
Download date	2026-11-07 12:21:59
Item downloaded from	https://hdl.handle.net/10468/18807

UCC
University College Cork, Ireland
Coláiste na hOllscoile Corcaigh

SOA Enhanced Optical Line Terminal for Future Optical Access Network

Fariba Jamali
120222712

Thesis submitted for the degree of Doctor of Philosophy



NATIONAL UNIVERSITY OF IRELAND, CORK

School of Engineering and Architecture

Department of Electrical and Electronic Engineering

Tyndall National Institute

Photonics Systems Group

February 2026

Head of Department: Prof. Jorge C. Oliveira

Supervisors: Prof. Paul Townsend
Dr. Cleitus Antony

Contents

List of Figures . . . iii
List of Tables . . . viii
Acknowledgements . . . x
Abstract . . . xi

1 Introduction 1
1.1 Technological Transitions in Broadband Access . . . 1
1.2 Research Motivation for Optical Domain Equalisation . . . 7
1.3 Structure of the thesis . . . 9

2 Advancements in Passive Optical Networks 12
2.1 High-Capacity PON Techniques and Requirements . . . 14
2.1.1 Functional Requirements . . . 14
2.1.2 IM/DD Pathway to Higher Speeds . . . 16
2.1.2.1 Performance Metrics in IM/DD . . . 19
2.1.2.2 Tradeoffs and Limitations . . . 22
2.1.3 Scaling Capacity by Coherent Technology . . . 24
2.2 Physical Layer Impairments . . . 26
2.2.1 Burst Power Equaliser: Transimpedance Amplifier . . . 27
2.2.2 Bandwidth Limitation . . . 29
2.2.3 Noise Sources . . . 31
2.2.4 fibre Optic Degradations . . . 35
2.2.5 Optical Amplification . . . 40
2.3 Equalisation and Signal Post Processing . . . 44
2.3.1 IM/DD . . . 44
2.3.2 Coherent PON DSP Blocks . . . 48
2.4 SOA-Based Power equalisation Methods . . . 52
2.4.1 Variable Bias . . . 54
2.4.2 Control Light Injection . . . 55
2.5 Summary . . . 56

3 SOA Output Power Control through Dynamic Gain Adjustment 58
3.1 SOA for High-Speed PON . . . 59
3.1.1 SOA Gain Mechanism . . . 59
3.1.2 Experimental Devices in This Thesis . . . 62
3.1.3 Frequency Response . . . 64
3.1.4 Gain Response to Optical Bursts . . . 65
3.1.5 BPF for ASE Suppression . . . 66
3.1.6 Impact of SOA Amplification on Modulated Signal . . . 67
3.2 Method A: Variable Bias . . . 71
3.2.1 Gain Control Mechanism . . . 71
3.2.2 Features: Gain Change and Target Output Power . . . 72
3.3 Control light injection . . . 73
3.3.1 Gain Control Principle . . . 74
3.3.2 Optimisation of Control Light Wavelength . . . 74

3.3.3 Injection Direction of Control Light 75
3.3.4 Dynamic Range and Target Output Power 77
3.4 Comparison of two methods 78
3.5 Real Implementation Complexity Analysis 81
3.6 Summary 83

4 SOA-Based Power equalisation on a 100G IM/DD PON 85
4.1 Rationals and Research Aims 86
4.2 Continuous Mode Analysis with an Ideal Receiver 87
4.2.1 Experimental Setup 87
4.2.2 Results and Discussions 88
4.3 Realistic Condition: Burst-Mode Analysis 89
4.3.1 Allocation of the Physical Layer Overhead Time 89
4.3.2 Experimental Setup 92
4.3.3 Results and Discussions 94
4.4 Integration: Transfer Printing SOA 97
4.4.1 Micro-Transfer Printing Technology 97
4.4.2 Under Test TP-SOA 99
4.4.3 System-Level Test 101
4.5 Increasing Capacity: PAM8 Signal Quality 102
4.5.1 Experimental Results 103
4.6 Summary 104

5 SOA-based Power equalisation over a 400 Gb/s Coherent PON 106
5.1 Functional Overview 107
5.1.1 Frequency Comb Source as Local Oscillator 108
5.1.2 Optical Amplification for Low Power LO Compensation . 110
5.2 Experimental Setup 114
5.3 Experimental Results 117
5.4 Summary 120

6 Conclusion 122
6.1 Summary of Contributions 123
6.2 Future Research Directions 124

Acronyms 127

List of Figures

1.1 Internet architecture. 2
1.2 The evolution of the PON standards.[4] 4

2.1 Upstream transmission scheme for future PONs, considering IM/DD and coherent technologies operating in the O- and C-bands, respectively. 13
2.2 Maximum reach versus splitter ratio for given PON power budget of 29 dB. 15
2.3 Dynamic range between "soft" and "loud" burst packets. 16
2.4 Power spectral density envelope for randomly-generated NRZ, PAM4, and PAM8 signal. 18
2.5 Example of BER estimation for PAM4 using Gaussian PDFs. Histograms of received samples (bars) are overlaid with Gaussian fits (curves). Vertical dashed lines indicate decision thresholds. The shaded regions represent the probability of error for each level. 20
2.6 Eye diagrams of NRZ and PAM4 with normalised vertical full swing level. Arrows indicate the level-to-level amplitude differences in each eye diagram. 22
2.7 Modulation level impact on receiver sensitivity. 23
2.8 Constellations of the inphase and quadrature phases of lightwave carrier under modulation formats QPSK, 16QAM with three rings, and dual polarisation QPSK. 24
2.9 PSD of randomly generated 4QAM (QPSK), 16QAM, and DP-QPSK at the same bit rate. 25
2.10 (a) Constellation diagram with error vectors (green). EVM is computed as the RMS distance normalised to the reference symbol power. (b) Symbol error probability for M-QAM, plotted using the expression in [41]. 25
2.11 (a) IM/DD simulation setup for receiver bandwidth and chromatic dispersion analysis of M-PAM signals. (b) Baseband-equivalent coherent M-QAM simulation model for phase-noise and chromatic dispersion analysis. 27
2.12 The latest state-of-the-art BM-TIA architecture [19] 28
2.13 Frequency response of the entire transmission system using BM-TIA at sensitivity and overload levels (redrawn based on [49]). . 29
2.14 Eye diagram and histogram of a simulated 100 Gb/s PAM4 transmission after applying 18.75 GHz Bessel filter. 30
2.15 Simulated phase-noise-induced distortion of QPSK and 16QAM constellations at a symbol rate of 50 Gbaud for different transmitter and LO laser linewidths. 34

2.16 SBS threshold power in standard single-mode fibre. Solid lines show the analytical SBS threshold P_{th} evaluated using Equation (2.24). Dashed curves indicate representative reference values inferred from the exact noise-initiated theory reported in [54] and are included for qualitative comparison. 36
2.17 Eye diagrams from simulation of 50 Gbaud transmission over 5 km (dispersion $D \approx 17\ \mathrm{ps}/(\mathrm{nm}\cdot\mathrm{km})$): (a) PAM4 and (b) PAM8. . . 38
2.18 Simulated constellations for 50 Gbaud 16QAM using the coherent transmission setup in Figure 2.11.(b), for different lengths of C-band SMF. 39
2.19 SOA gain compression effect on a PAM4 pulse 43
2.20 Schematic illustration of SOA saturation effects for a BPSK signal. 44
2.21 (a) Schematic of a GRU unit, and (b) the concept of combining modular GRUs for addressing multiple impairments is shown, where each "module" is exposed to a single isolated impairment during training. 47
2.22 Functionality of the digital filtering stage. For linear filtering, the order of the two sub-blocks may of course be reversed. 50
2.23 Simulation results showing the impact of SOA bias adjustment on (a) gain and noise figure, and (b) saturation input power. 54
2.24 Simulation results showing (a) the SOA material gain coefficient spectra at different carrier densities and (b) the SOA gain spectra at different input powers. 55

3.1 (a) Schematic energy band diagram of an InP-based SOA under forward bias, showing carrier confinement in the quantum-well active region, quasi-Fermi level separation, and the optical transitions responsible for (i) absorption, (ii) stimulated emission, and (iii) spontaneous emission. (b) Single quantum-well (SQW) and (c) multiple quantum-well (MQW) band structures illustrating how MQWs increase the effective active region and enhance optical gain compared to SQW. 60
3.2 Relationship between carrier density and injection current in an SOA. N_0 and I_{th} are the number of carriers and bias current at transparency. 62
3.3 Experimentally measured (a) ASE spectra comparison of *CIP-SOA-S* and *CIP-SOA-L* with EDFA, (b) *CIP-SOA-S* (biased at 100 mA) and *CIP-SOA-L* (biased at 500 mA) gain at increasing input power. -8.7 dBm and +4 dBm are saturation input powers for SOA-S and SOA-L at 1535 nm, respectively. 63
3.4 Experimental frequency response measurements of *CIP-SOA-S* at varying input power levels. The SOA is biased at 100 mA for all input power levels. 65
3.5 The impact of optical filter bandwidth on the receiver sensitivity in an experimental 100 Gb/s PAM4 transmission at BER = 10^{-2}. 66

3.6 Experimental measurement of *CIP-SOA-S* gain variation with increasing input power in three regions: the OSNR-limited regime, the linear operation regime, and the nonlinear (saturation) regime. 68
3.7 Experimental evaluation of the impact of reduced OSNR and gain saturation in *CIP-SOA-S* on 50 Gbaud M-PAM transmission. . . . 69
3.8 Experimental constellation diagrams showing the impact of *CIP-SOA-S* amplification on DP-QPSK and DP-16QAM signals at increasing input power levels. 70
3.9 Experimentally measured (a) *CIP-SOA-S* gain spectrum highlighting the effect of bias current on gain change, and (b) gain measurement as a function of increasing input power at multiple bias currents, solid black line is gain versus saturation input power levels and dashed black line shows the required gain to fix the output power at -2 dBm by increasing the input power. 73
3.10 Experimental measurement of (a) *CIP-SOA-S* gain spectrum highlighting the peak gain wavelength shift at high input powers, (b) signal gain at -30 dBm input power to the SOA for a signal placed at 1535 nm, measured for various control light power levels at different control light wavelengths. 75
3.11 (a) Co-propagation injection scheme, (b) counter-propagation injection scheme. The SOA is longitudinally divided into n sections of equal length, and the carrier density graphs correspond to the case where the control light power is much higher than the input power. (c) Experimentally measured OSNR comparison of the two propagation schemes as a function of control light power at an SOA input power of -30 dBm. The loss of the WDM is not taken into account in this measurement. 76
3.12 Experimentally measured SOA signal gain as a function of increasing input power for multiple control light power levels. Solid black line is gain versus signal saturation input power levels and the dashed black line shows the required signal gain to fix the output power at -2 dBm by increasing the input power. 77
3.13 Experimental measurement of (a) SOA signal gain reduction compared to the small-signal gain, with a 3 dB drop defined as the saturation threshold across different operating modes, and (b) Fitted values of saturation power versus small signal gain. . . . 78
3.14 (a) Experimental OSNR measurement as a function of SOA signal input power before and after equalisation using the proposed schemes. The OSNR for control light injected from the SOA output is also included. (b) Experimental Noise figure measurement versus small signal gain after equalisation using the proposed techniques. 80
3.15 The SOA gain controller structure for the two proposed equalisation methods: (A) variable bias, and (B) control light injection. . 82

4.1 Experimental setup emulating PAM4 PON upstream back-to-back transmission using ideal transmitter and receiver to study the two SOA gain control schemes A and B. 87
4.2 BER performance versus SOA input power for the three modes of SOA operation: fixed SOA bias with no power equalisation and the two SOA gain control schemes to maintain a constant output power of -2 dBm. 88
4.3 Logical structure of the burst frame. 90
4.4 Effect of inserted inter-packet idle intervals (guard-time emulation) on the performance of a continuous-wave 100 Gb/s PAM4 transmission using the experimental setup shown in Figure 4.1. The receiver input power is fixed at -2 dBm using the equalisation techniques. 91
4.5 Experimental setup for high-speed burst-mode traffic analysis with SOA preamplified receiver performing optical equalisation using two schemes, (A) variable bias, and (B) control light injection. . 93
4.6 Burst-mode (loud (ONU1), and soft (ONU2)) and continuous mode (ONU1) BER measurements using SOA-based equalisation techniques in a 100 Gb/s back-to-back PAM4 transmission. Eye patterns are provided for both ONU1 and ONU2 at an input power of -2 dBm to the SOA. 95
4.7 (a) Signal traces of burst signals before and after equalisation with two techniques, captured after the SOA preamplifier. (b) BER measurements for 100 Gb/s burst-mode PAM4 transmission using SOA-based equalisation at various dispersion levels. Markers indicate counting errors, and solid lines represent stochastic errors. 96
4.8 Overview of the micro transfer printing process for integrating prefabricated III–V devices onto silicon photonic circuits [30]. . 97
4.9 TP-SOA chip layout and probe station connection. 99
4.10 Measured spectra of the TP SOA at (a) low and (b) high input powers for multiple bias currents, used to assess potential parasitic lasing. 100
4.11 Measured TP-SOA gain as a function of input power for several bias currents, illustrating a gain variation of approximately 17 dB. 100
4.12 (a) BER comparison of TP-SOA and *CIP-SOA-S* at a fixed bias current of 100 mA for 100 Gb/s PAM4 transmission over a wide dynamic range, and (b) bias reduction impact on the BER performance improvement at high input powers. 101
4.13 Eye diagrams at increasing input powers for multiple bias currents. 102
4.14 150 Gb/s PAM8 burst-mode back-to-back transmission employing SOA-based power equalisation is analysed. Continuous-mode operation using a linear SOA is included for comparison, and EDFA preamplification serves as an ideal reference case. 103

5.1 Simplified system model of the upstream transmission using a low-cost DFB laser at the ONU and a frequency-comb source at the OLT as the LO [60]. Power spectra at different stages are included. 108
5.2 OLT receiver architecture showing two possible configurations when a frequency-comb source is used as the LO: (A) SOA-based signal pre-amplification and (B) SOA-based LO power boosting. 110
5.3 Dual-channel TIA–AGC architecture in automatic adjustable mode. This diagram represents X channel only. Y channel has the same diagram. 111
5.4 Experimentally measured BER versus input optical power for a continuous-mode 50 Gbaud DP-16QAM back-to-back transmission using the integrated coherent receiver, without optical amplification and with an LO power of +10 dBm. 112
5.5 BER measurements for a 400 Gb/s DP-16QAM continuous-mode signal, where the receiver analogue gain is adjusted for each input power, comparing two configurations: (a) an SOA in the LO path with a fixed bias and input powers of 0 dBm, –5 dBm, and –10 dBm, resulting in different LO power levels, and (b) an SOA used as a preamplifier with a fixed bias and two different LO powers. . . 113
5.6 Experimental setup of a 20 km optical upstream link in a flexible coherent PON supporting a net data rate of up to 312 Gb/s. The packet frame structure is also shown. 115
5.7 Experimental results of 50 Gbaud DP-QPSK and DP-16QAM signals in continuous mode operation after 20 km transmission, measured at different LO power levels using an SOA preamplifier biased at 120 mA and a variable analogue-gain receiver. 118
5.8 Constellation diagrams for both modulation formats measured at an SOA input power of 0 dBm and an LO power of -3 dBm, comparing the back-to-back configuration with 20 km fibre transmission. 119
5.9 Experimental results of 50 Gbaud DP-QPSK and DP-16QAM continuous mode signals at different values of LO power in a 20 km transmission using variable gain SOA and fixed, low receiver analogue gain. Constellation diagrams are for -3 dBm LO power at SOA input power of 0 dBm. 120

6.1 Schematic of an integrated optical equaliser in a coherent receiver employing an integrated comb source as the LO for future ultra-high-speed PONs. 126

List of Tables

2.1 SOA simulation parameters 53

3.1 Comparison of the CIP-SOA characteristics used in this study . . 64

4.1 TP-SOA (excluding coupling loss) and *CIP-SOA-S* characteristics. 100

I, Fariba Jamali, certify that this thesis is my own work and has not been submitted for another degree at University College Cork or elsewhere. All external references and sources are clearly acknowledged and identified within the contents. I have read and understood the regulations of University College Cork concerning plagiarism and intellectual property.

Fariba Jamali

Acknowledgements

Writing this thesis marks the end of a long journey shaped by persistence and dedication, and made possible by the support of many people. During my PhD, I have been fortunate to receive guidance, encouragement, and patience from my supervisors, colleagues, friends, and family. I would like to express my sincere gratitude to them for helping me reach this point.

Thank you to my supervisors, Prof. Paul Townsend and Dr. Cleitus Antony, for the opportunity to pursue this PhD and for encouraging a questioning mindset. Paul, thank you for shaping the direction of this research, helping me develop the ideas that underpin this thesis, and strengthening my understanding of the physics behind this work. Cleitus, thank you for your practical support and thoughtful feedback, which greatly improved this thesis.

I joined during the COVID-19 pandemic and lockdowns, so meeting colleagues in person was a rare and meaningful moment. Stephen and Hilmi were the first PSG team members I met in the lab, and I am very grateful for the welcome and support they gave me. I feel incredibly fortunate to have worked with Stephen during my PhD. Thank you for teaching me how to work with the lab equipment, for the confidence you gave me throughout this journey, and for always helping me whenever I got stuck. I still keep the troubleshooting diagram you drew for my setup, which helped me resolve problems when things were not working as expected. Even after you graduated and left the group, you continued to support me, and I truly appreciate it. Hilmi, although we worked together only briefly, I learned a lot from you. Thank you for taking the time to answer my questions and for your help and guidance. I also thank all PSG members and the many people at Tyndall for their kindness, support, and contributions, both direct and indirect, to my PhD experience.

To my family in Iran, thank you for your constant love and support throughout my PhD. Even from afar, your belief in me gave me strength during the most challenging moments, and it has meant more to me than I can express. I am especially grateful to my mum and dad, and to my sisters, for always encouraging me to keep going. I would also like to thank my friends, both those I have known for many years and those I met here in Ireland, for their kindness and emotional support. Thank you for being there for me, for listening, for reassuring me when things felt overwhelming, and for helping me feel at home in Cork.

Finally, I thank my husband, Ehsan, my best friend who has also been on his own PhD journey alongside me. Thank you for always being there for me, for listening to my concerns and thoughts, and for the many technical discussions we shared on the way home. Your constant encouragement gave me confidence at every stage of this PhD, and you always celebrated even the smallest progress I made. I am deeply grateful for your patience, support, and belief in me, and I am excited for the next chapter we will begin together after the PhD.

Abstract

Future passive optical networks (PONs) aim to deliver data rates of 100 Gb/s per wavelength using intensity-modulation direct detection (IM/DD) and up to 400 Gb/s per wavelength using coherent technology. Achieving these targets requires overcoming the large dynamic range of burst-mode upstream packets, typically around 20.5 dB, caused by differential loss between optical network units (ONUs). Conventional burst-mode receivers rely on transimpedance amplifiers (BM-TIAs) that adjust electrical gain for each burst, but their limited linearity and bandwidth restrict scalability to higher speeds. As IM/DD systems approach and exceed 100 Gb/s per wavelength, they also struggle to meet the 29 dB optical power budget defined by the International Telecommunication Union (ITU-T) G.9804 standard. Coherent transmission is therefore seen as a promising solution for extending PON capacity, offering superior receiver sensitivity, higher spectral efficiency, and inherent chromatic dispersion tolerance.

This thesis investigates Semiconductor Optical Amplifier (SOA)-based optical burst power equalisation as a promising approach to dynamic range management across both IM/DD and coherent PON architectures. By regulating optical gain before photodetection, SOA-based equalisation mitigates gain saturation effects, suppresses nonlinear distortions, and reduces the need for complex digital signal processing. Two novel techniques are developed and experimentally demonstrated: (A) variable bias and (B) control light injection. Both methods achieve a 24 dB dynamic range in 100 Gb/s 4-level pulse amplitude modulation (PAM4) burst-mode transmission with bit error rates below the soft-decision forward error correction threshold using a simplified low-gain receiver.

The optical-domain equalisation concept is further extended to coherent PONs employing dual-polarisation 16-quadrature amplitude modulation (DP-16QAM). In this case, a low-power local oscillator (LO) configuration is implemented to demonstrate compatibility with potential comb-source-based architectures. This design relaxes the wavelength alignment requirement between the ONU and the LO, addressing one of the main challenges in coherent PONs where ONU wavelengths can drift by a few nanometers. SOA gain control enhances linearity and enables high-fidelity burst detection without requiring fast BM-TIAs.

These findings show that SOA-based equalisation eliminates the need for high-gain BM-TIAs, thereby preventing bandwidth, gain, and dynamic range limitations associated with the TIA in both coherent and IM/DD systems. Furthermore,

the results demonstrate that complex digital signal processing is unnecessary to achieve high dynamic range using an SOA preamplifier, and that simple linear equalisation is sufficient to compensate for low-cost 25G-class receiver bandwidth limitations and moderate fibre dispersion in IM/DD systems.

To explore manufacturable integration, a transfer-printed SOA preamplifier is demonstrated for the first time in a 100 Gb/s PON context, confirming its potential for scalable, and low-cost receiver designs. Overall, this work establishes SOA-based optical power equalisation as a key enabler for next-generation high-speed PONs. It provides a pathway to support 100 Gb/s IM/DD and 400 Gb/s coherent operation while maintaining high dynamic range, receiver sensitivity, and system simplicity, enabling fully integrated, energy-efficient, and cost-effective optical access networks.

Chapter 1

Introduction

This chapter introduces Passive Optical Networks (PONs) as a cost-effective fibre access technology and traces their evolution towards supporting ever-increasing broadband demands. It highlights their role in modern high-speed connectivity and motivates the need for optical power equalisation as a key enabler of future PON generations. Finally, the chapter provides an overview of the thesis structure.

In today's digital landscape, the increasing need for high-bandwidth services such as high-definition video streaming, teleconferencing, and the expansion of the Internet of Things (IoT) has led to a global shift from copper-based broadband to more advanced fibre-optic networks. These networks, often built on Passive Optical Network (PON) technologies, offer significantly higher speeds and greater capacity, essential for meeting modern data demands [1]. It is therefore crucial to enhance optical communication technologies, not only to meet current needs but also to expand the capabilities of these networks, ensuring they can support future digital services without compromising performance.

1.1 Technological Transitions in Broadband Access

The transition to optical access networks has been driven by the increasing demand for higher data rates, lower latency, and improved scalability in broadband services. Before optical fibre became the dominant transmission medium in access networks, digital subscriber line (DSL) and cable networks were widely used.

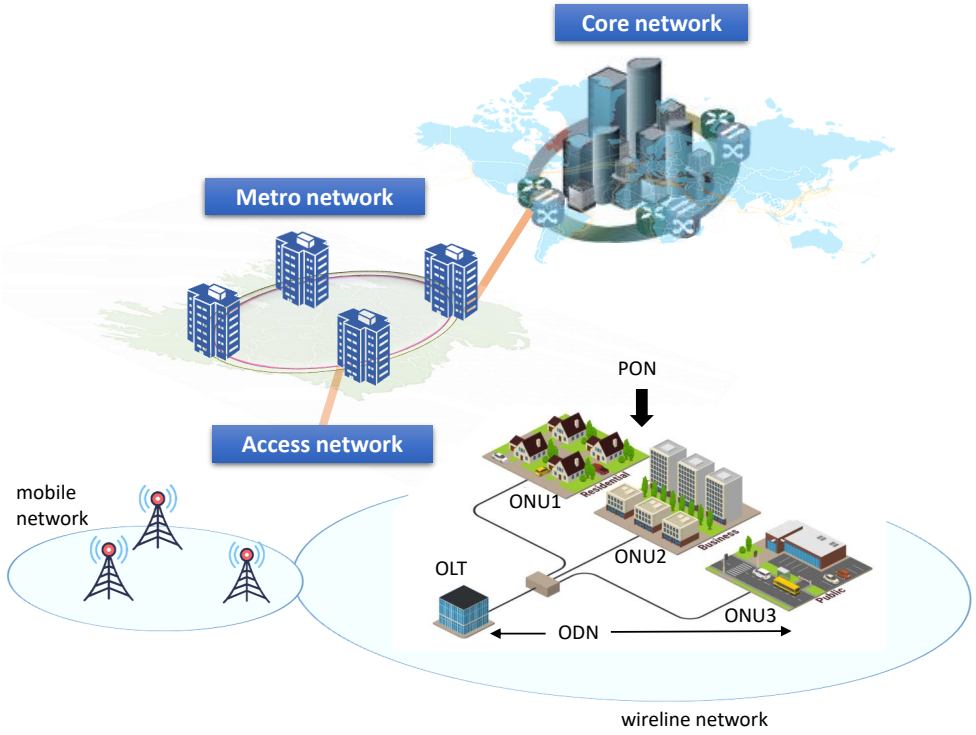


Figure 1.1: Internet architecture.

DSL, introduced in the late 1980s, provided data rates ranging from 128 kb/s to 1.5 Mb/s over copper telephone lines, while cable networks offered higher speeds of up to 10 Mb/s using coaxial cable infrastructure. However, as internet usage grew, particularly with the rise of video streaming and cloud-based applications in the early 2000s, these technologies struggled to meet bandwidth demands.

To address these limitations, optical fibre was introduced into access networks through hybrid architectures such as fibre to the Node (FTTN) and fibre to the Curb (FTTC). In FTTN, fibre was deployed to a neighbourhood node, with the remaining distance to users covered by copper-based Very High-Speed DSL (VDSL), which provided data rates of up to 100 Mb/s within 400 meters of the node. Similarly, FTTC brought fibre closer to users but still relied on copper for the last segment. While these solutions improved performance, the inherent limitations of copper transmission, such as high attenuation and signal degradation over distance, prevented them from scaling to gigabit speeds.

The need for higher-capacity broadband access led to the development of fibre to the Home (FTTH), where optical fibre extends directly to residential and business premises. Unlike copper-based solutions, FTTH eliminates bandwidth bottlenecks and supports symmetrical data rates of 1 Gb/s and beyond. How-

ever, deploying dedicated fibre to each user was initially costly, leading to the adoption of PON technology, which optimises fibre utilisation through a point-to-multipoint (P2MP) architecture.

A conventional PON, as illustrated in Figure 1.1, consists of three key components: the Optical Line Terminal (OLT) at the central office, the Optical Distribution Network (ODN), and the Optical Network Unit (ONU) at the end-user's premises. The OLT manages both downstream and upstream data transmission, while the ODN—comprising optical fibres and passive splitters—distributes signals without requiring electrical power. The ONU, located at the customer premises, converts optical signals into electrical signals for internet, voice, and video services.

Since PON operates as a shared medium, downstream data is broadcast to all ONUs, with encryption ensuring secure delivery. An ONU receives all downstream data, selects data destined to its users, and drops data to other ONUs. In the upstream, local data from end users will first be buffered at ONUs, the OLT schedules upstream transmission opportunities by assigning dedicated time slots to ONUs. An ONU bursts out buffered data to the OLT in the time slots pre-assigned by the OLT. This avoids transmission collision, and multiple ONUs are able to share the upstream wavelength channel. This efficient structure has made FTTH-PON the dominant choice for modern fibre access networks, supporting increasing bandwidth demands while maintaining cost-effectiveness.

The journey of PON began in the late 1990s when telecom operators and industry groups recognised the need for a scalable fibre-access solution. Initial standardisation efforts were led by the International Telecommunication Union (ITU) and the Institute of Electrical and Electronics Engineers (IEEE), resulting in the first-generation PON architectures. The earliest systems were based on Asynchronous Transfer Mode (ATM), leading to the development of APON (ATM PON) and its improved version, BPON (Broadband PON) [2]. However, BPON was soon replaced by Gigabit PON (G-PON), which offered higher bandwidth, improved efficiency, and broader adoption. As a result, G-PON became the dominant standard, expanding the global PON market and surpassing earlier systems in deployment. G-PON's specifications were defined by the Full Service Access Network (FSAN) group and later standardised as ITU-T G.984. It has been widely deployed across North America, Europe, the Middle East, Australasia, and Asia [3]. Meanwhile, the IEEE introduced Ethernet PON (E-PON) under IEEE 802.3, which leveraged Ethernet technology for data transmission and gained significant traction, especially in Asia. Both E-PON and G-PON have the same general

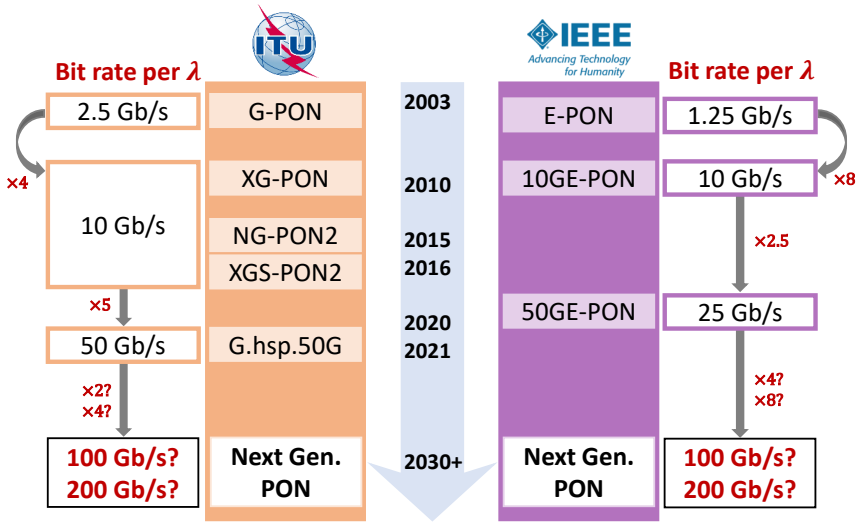


Figure 1.2: The evolution of the PON standards.[4]

principle in terms of framework and applications, but their operation is different due to the implementation of the physical and data link layers.

The evolution of PON standardisation has followed a continuous path of innovation, adapting to increasing bandwidth demands and advancing optical technologies. Figure 1.2 illustrates this progression, starting from G-PON and E-PON and extending to potential future developments. The transition beyond G-PON led to the introduction of 10G-PON, standardised in two versions: XG-PON (ITU-T G.987), which provided 10 Gb/s downstream and 2.5 Gb/s upstream, and XGS-PON (ITU-T G.9807), which supported symmetrical 10 Gb/s transmission [5], [6]. Although the standard for XG-PON was established in 2010, large-scale deployments did not take off until 2016, largely due to the slow pace at which network operators adopt new technologies. This delay highlights a pattern observed in broadband evolution, where major access network upgrades tend to occur in roughly 10-year cycles.

Once XG-PON was in deployment, the focus shifted to achieving at least 40 Gb/s, leading to the development of Next-Generation PON 2 (NG-PON2) [7]. This standardisation effort within ITU-T G.989, completed in 2015, sparked significant debate regarding the best technological approach. Initially, Wavelength Division Multiplexing PON (WDM-PON) was considered, replacing optical splitters in the ODN with an Arrayed Waveguide Grating (AWG). However, this approach faced two major obstacles:

- It was incompatible with existing Time Division Multiplexing PON (TDM-PON) systems.

- It required significant modifications to the ODN infrastructure, making deployment costly and impractical.

As a result, NG-PON2 adopted Time and Wavelength Division Multiplexing (TWDM) instead, utilising four wavelengths per direction to achieve the targeted 40 Gb/s downstream capacity [8]. However, technical challenges emerged, including burst-mode wavelength drift and out-of-band optical interference, requiring new tuning mechanisms for ONUs [9].

Although NG-PON2 struggled in the market, its development influenced the next phase of PON standardisation. Recognising the need for higher data rates while maintaining cost efficiency, IEEE initiated the 802.3ca project, leading to the specification of 100-Gigabit Ethernet PON (100GE-PON) [10]. Around the same time, advancements in 25 Gb/s per wavelength transmission were driven by 100-Gigabit Baseband Long-Reach, 4-lane Ethernet (100GBASE-LR4) optics in data centres, which combined four 25 Gb/s wavelengths over a single fibre. However, directly adapting 100GBASE-LR4 for PON was not feasible due to fundamental differences in network architecture:

- LR4 operates over two fibres, while PON must function over a single fibre.
- The power budget for PON systems is 29 dB in the N1 class, with even higher allowable losses in other classes, which is significantly greater than the 18 dB power budget of LR4.

Given these constraints, IEEE 802.3ca revised its objectives, ultimately settling on a 50GE-PON specification using two 25 Gb/s wavelengths to strike a balance between cost, feasibility, and performance. The finalised standard, completed in 2020, defined two downstream bands and three upstream bands, ensuring coexistence between 10GE-PON and 50GE-PON. Enhancements such as low-density parity-check (LDPC) forward error correction (FEC), high-power transmitters, and improved avalanche photodiode (APD) receivers were introduced to support higher power budgets [11], [12].

In parallel, interest in a single-wavelength 25G-PON grew as a simplified alternative to 50GE-PON. A Multisource Agreement (MSA) emerged to specify such a system by combining elements of ITU-T G.9807.1 with the physical layer from IEEE 802.3ca. Although not formally standardised, 25G-PON was positioned as the fastest single-wavelength PON system achievable without digital signal processing (DSP) for adaptive equalisation. Despite several proposals to ITU-T Q2, consensus on standardising 25G-PON was never reached, as major operators

did not consider it a priority for near-term deployment.

As the 50GE-PON project progressed, research into higher-speed PONs became more concrete. In 2016, ITU-T began investigating next-generation PON technologies, leading to a formal standardisation project in 2018. This effort took a top-down approach, focusing on key operator requirements: coexistence with existing PON deployments, low-cost implementation, and at least four times the capacity of existing systems with target deployment around 2025.

Given this timeline, 50G-PON (ITU-T G.9804) was selected as the next step, supporting 50 Gb/s per wavelength in both upstream and downstream directions. Unlike its predecessors, 50G-PON incorporated DSP, allowing for channel equalisation to compensate for signal degradation at high data rates [13]. The standard, approved in 2021, sought to reuse many design elements from IEEE 802.3ca, including its wavelength allocation and FEC strategy, while diverging in its assumption of DSP-based equalisation for handling high-speed transmission challenges.

Looking forward, the next evolution of PON is expected to reach 100G-PON (100 Gb/s per wavelength) and 200G-PON (200 Gb/s per wavelength). Figure 1.2 outlines these future possibilities, with 100G-PON expected to be feasible using intensity modulation and direct detection (IM/DD) [14], [15], [16], while 200G-PON will likely require coherent detection because of its spectral efficiency, higher receiver sensitivity, and built-in dispersion compensation [17], [18]. Given the four-times bandwidth scaling pattern, 200G-PON aligns with long-term trends, though 100G-PON remains a popular intermediate step.

As optical access networks continue to evolve, the industry must balance higher speeds, cost efficiency, and backward compatibility, ensuring that future PON generations meet the growing demands of broadband services, 5G backhaul, cloud computing, and industrial networking. This thesis proposes optical-domain power equalisation as a highly effective solution to enable up to 400 Gb/s transmission in PONs, while maintaining system efficiency and scalability for future deployment.

1.2 Research Motivation for Optical Domain Equalisation

In upstream transmission, differences in distance and optical losses between users and the central office's OLT create a wide range of power levels in upstream packets. The conventional solution to address these fluctuations is to use burst-mode trans-impedance amplifiers (BM-TIAs), which adjust their gain for each incoming packet to ensure proper receiver operation [19], [20]. An alternative approach currently under investigation is to perform power equalisation directly in the optical domain by adjusting the gain of preamplifiers according to the incoming burst power. By stabilising packet powers before electrical detection, optical-domain equalisation reduces the burden on the BM-TIA. Semiconductor Optical Amplifiers (SOAs) are particularly attractive for this purpose, as they are compact, cost-effective, and readily integrable with other receiver components. Building on the concept of optical-domain equalisation, different approaches have been investigated to mitigate the large dynamic range of burst-mode upstream signals in PONs. Early attempts relied on cascaded SOAs to provide power equalisation in 10 Gb/s EPON systems, which partially reduced packet-to-packet variations but suffered from incomplete equalisation and pronounced gain saturation at high input powers [21], [22]. To overcome these limitations, SOA gain control through injection current modulation was proposed as an alternative. This approach has been experimentally validated in 10 Gb/s non-return-to-zero (NRZ) PONs, where current-controlled SOAs demonstrated improved equalisation of burst signals and extended reach [23], [24]. More recently, the same technique has been applied to 25 Gb/s 4-level pulse amplitude modulation (PAM4) PONs, where an SOA operated with dynamic gain control successfully equalised burst-mode inputs while maintaining compatibility with cost-effective 10G-class optics [25].

While these approaches demonstrated that SOA gain could be dynamically adjusted to reduce burst-to-burst power variations, these solutions were never adopted in commercial systems. The reason was not lack of feasibility, but lack of necessity; as preamplification was not required and at rates up to 25 Gb/s using simple IM/DD modulation, electronic burst-mode receivers (BMRx) were still able to provide the required bandwidth, linearity and dynamic range. Consequently, SOA-based equalisation remained a technically interesting but non-essential alternative.

This situation is now changing. As PONs evolve toward higher line rates ($\geq$100 Gb/s) and more spectrally efficient modulation formats, initially multi-level IM/DD (e.g., 50 Gbaud PAM4) and eventually coherent detection, the traditional BMRx is approaching fundamental limits. Achieving wide dynamic range, high linearity, and higher bandwidth simultaneously is becoming increasingly challenging, with state-of-the-art BM-TIAs offering $\approx$15 dB dynamic range [19], far short of the required 20.5 dB according to the latest 50G-PON standard [13]. Taken together, these factors, along with the use of SOAs as preamplifiers at the OLT to meet the 29 dB optical power budget required to compensate for the maximum expected loss in IM/DD-based PON systems [26], [27], motivate our investigation into whether SOA-based power equalisation can effectively support the higher data rates and multi-level modulation formats required for future PONs.

Another motivation is that using SOAs as preamplifiers introduces gain-saturation effects that distort the signal, and these distortions usually require complex DSP to correct [28], [29]. If adjusting the SOA dynamics can reduce these nonlinear effects at the source, then SOA-based power equalisation could both handle the dynamic-range problem and lessen the DSP requirements at high data rates.

Bias current modulation has been widely used for SOA gain control, but its performance degrades under the high input powers and bandwidths required in future high-speed PONs, where lowering the bias can worsen noise figure, and reduces the saturation power. To address these limitations, this thesis also investigates a novel approach that controls SOA gain without operating at low bias, thereby preserving better noise and linearity and offering the potential to more effectively suppress saturation induced nonlinear effects, which are highly disruptive for multi-level modulation formats such as 50 Gbaud PAM4 and beyond. Examining both approaches provides insight into the trade-offs between speed, linearity, noise, and implementation complexity.

In addition to evaluating equalisation techniques using discrete SOAs, this thesis also examines their relevance to integrated photonics by demonstrating high-speed PON operation with a transfer-printed SOA (TP-SOA). Transfer printing is an emerging integration method that enables combining high-performance III–V SOAs with low-cost silicon photonics platforms [30]. This allows assessment of whether SOA-based equalisation remains effective when implemented in a compact, integrated form factor which is an important consideration as future PON transceivers move toward increased integration to reduce cost.

Beyond IM/DD systems, SOA-based power equalisation has also been explored in coherent PONs, where combining SOA preamplification with DSP enabled real-time burst-mode reception of 20 Gb/s single-polarisation quadrature phase shift keying (QPSK) signals with wide dynamic range [31]. At this rate and with this modulation format, SOA nonlinearities are relatively weak, and conventional BM-TIAs still offer sufficient dynamic-range performance, so optical-domain equalisation is not essential. Looking ahead, 200G/400G coherent PONs will demand much higher bandwidths and more advanced modulation formats such as M-aray quadrature amplitude modulation (M-QAM), where SOA nonlinearity becomes a dominant impairment. This emerging challenge motivates a fresh examination of SOA-based gain control within coherent architectures.

Moreover, although coherent receivers do not conventionally rely on SOA preamplification for sensitivity enhancement, there are still architectural and performance-driven reasons to introduce an SOA into next-generation coherent PON designs. Identifying and addressing these reasons, particularly in the context of coherent PON optimisation, is investigated as part of our coherent PON study.

Motivated by these challenges, this thesis investigates the feasibility of SOA-based power equalisation for high-speed PONs. It experimentally evaluates two equalisation techniques, referred to in this thesis as variable bias and control-light injection, using 100 Gb/s PAM4 upstream signals, analyses their impact on dynamic range, linearity, saturation behaviour, and noise, and examines their relevance not only to advanced IM/DD systems but also to emerging coherent PON architectures. Through this study, the thesis establishes key performance trade-offs and integration considerations, demonstrating that optical-domain equalisation is a promising and scalable solution for enabling burst-mode reception in future high-speed IM/DD and coherent PON systems.

1.3 Structure of the thesis

This thesis introduces a novel optical access system for next-generation passive optical networks, leveraging SOA-based optical power equalisation. By implementing two proposed gain control techniques within the SOAs, it demonstrates how to effectively manage and mitigate nonlinear effects, allowing for improved signal stability and integrity. These techniques enable the SOAs to handle variations in incoming signal strength with negligible nonlinearities, significantly

extending the dynamic range without requiring complex DSP compensation algorithms.

The primary achievements of this research include the development of these optical gain control techniques and their validation through extensive theoretical analysis and experimental setups, culminating in the publication of two papers [A1], [A2]. Beyond the published results, this thesis further investigates the practicality of SOA-based equalisation in integrated platforms by demonstrating high-speed PON operation with a transfer-printed SOA, and it extends the discussion to assess how the proposed equalisation approaches can translate to future coherent PON architectures, where dynamic range and linearity requirements are even more stringent. In addition to the published works, two journal manuscripts are in advanced preparation: one on the TP-SOA, developed in collaboration with the III-V Materials and Devices Group at Tyndall National Institute, and a separate coherent-PON manuscript prepared for submission to *Photonics Technology Letters*.

Chapter 2 establishes the technical foundations of the thesis. It begins with a concise overview of PON architectures and transceiver operation, followed by the signal and system models used throughout. The chapter motivates the transition from NRZ to multilevel IM/DD formats (e.g., PAM4) and, for coherent PON, to phase- and polarisation-modulated schemes (PSK/QAM), highlighting the resulting gains in spectral efficiency and the associated complexity trade-offs. It then defines the performance metrics, and reviews channel and component impairments, including noise sources, analogue bandwidth limitations, chromatic dispersion, fibre and optical preamplifier nonlinearities. Equalisation and digital signal post-processing are subsequently analysed, including a simple feed-forward equaliser (FFE) and an overview of more complex DSP algorithms published by our own research group for IM/DD systems, as well as the principal DSP blocks for coherent reception, such as I/Q imbalance compensation, chromatic dispersion compensation, frequency-offset estimation, and carrier-phase recovery. Finally, the chapter introduces SOA-based optical equalisation techniques, presenting the latter from first principles via SOA carrier dynamics, gain saturation, and ASE to establish a clear link between device physics and the equalisation schemes used in later chapters.

Chapter 3 focuses on SOA-based power equalisation techniques developed and evaluated in this thesis. An initial analysis is presented of fundamental SOA characteristics, including the gain mechanism, frequency response, noise, and

patterning effects on modulated signals, establishing the physical basis for the equalisation schemes that follow. Two distinct approaches are considered for regulating the SOA gain in order to stabilise the packet output power and mitigate saturation-induced distortions. The first approach relies on varying the SOA bias current as a function of input power, and the second employs external control light injection at a different wavelength. Each method is introduced with its theoretical gain control mechanism, followed by detailed analyses of its operation, including optimisation of control parameters, achievable output power stability, and impact on signal quality. Comparative discussion highlights the advantages and limitations of each approach.

Chapter 4 presents the experimental validation of the proposed SOA-based equalisation schemes in a 100 Gb/s IM/DD PON. The chapter begins with continuous-mode back-to-back transmission experiments, establishing a baseline performance using commercial SOAs. It then extends the analysis to realistic burst-mode operation with multiple ONUs, where the techniques are evaluated against the requirements of the latest 50G-PON standard, including optical power budget, dynamic range, and dispersion tolerance. The chapter also explores the integration potential of transfer-printed SOAs through system-level demonstrations, comparing their performance with commercial devices. Finally, higher-order modulation (50 Gbaud PAM8) is investigated to reveal the limitations of IM/DD transmission and to motivate the transition toward coherent PON architectures, which form the focus of the following chapter.

Chapter 5 focuses on the application of SOA-based power equalisation in coherent PON. It introduces a new architecture that employs a frequency comb source at the OLT to maintain wavelength alignment between the ONU and local oscillator (LO), thereby motivating the integration of SOAs in coherent systems that would not typically require preamplification. The chapter analyses the system model, including the expected losses and LO power range associated with frequency comb operation, and presents a proof-of-concept experimental demonstration. Using a variable bias equalisation scheme, the results show wide dynamic range transmission at line rates up to 400 Gb/s, with reduced dependence on high-gain, high-dynamic-range burst-mode TIAs.

Chapter 6 concludes this thesis by summarising the key achievements and offering perspectives on potential future research directions.

Chapter 2

Advancements in Passive Optical Networks

This chapter provides the technical basis for the thesis. It first presents an architecture for future high-speed PON. It then explains the shift from NRZ to multilevel IM/DD formats such as PAM4, and, where relevant, to coherent dual-polarisation M-level quadrature amplitude modulation (DP-M-QAM). The discussion compares spectral efficiency with implementation complexity and the required OSNR. The chapter defines the key performance metrics and analyses the main impairments: thermal, shot, and amplified spontaneous emission (ASE) noise, analogue bandwidth limits, chromatic dispersion, and fibre and SOA preamplifier nonlinearities. Finally, it develops the SOA device physics (carrier dynamics, gain saturation, ASE, and noise figure) that support SOA-based optical power equalisation, and introduces the receiver-side digital signal processing used in later chapters.

Future access networks are converging on two credible technologies. On the one hand, the standardisation of 50G-PON in the O-band reflects a push to limit chromatic dispersion and preserve low-cost optics, making PAM4 IM/DD the near-term workhorse around 100 Gb/s per wavelength at practical symbol rates [32]. On the other hand, the growing demand for higher speeds and existing infrastructure in the C-band supports a transition to coherent detection with phase/amplitude/polarisation modulation, enabling 200–400 Gb/s per wavelength at comparable analogue bandwidths [33], [34], [35]. This thesis

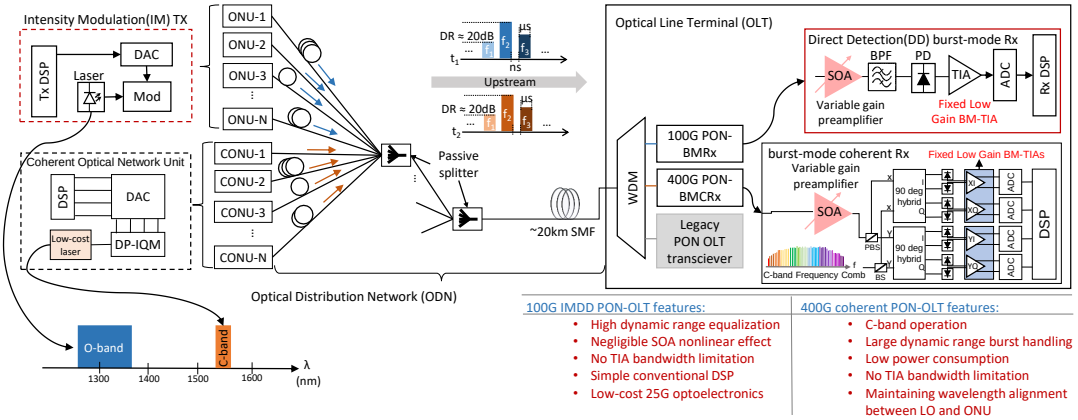


Figure 2.1: Upstream transmission scheme for future PONs, considering IM/DD and coherent technologies operating in the O- and C-bands, respectively.

addresses both directions and proposes receiver design solutions that make these speeds practical in either case.

Figure 2.1 demonstrates our proposed architecture for upstream PON and overlays an O-band IM/DD path and a C-band coherent path. Wavelength-domain separation allows IM/DD and coherent bursts to overlap in time. The focus on upstream transmission is motivated by its burst-mode nature, which makes it the most challenging direction to engineer and the primary limitation for PON scaling. The architecture places SOA-based optical-domain burst power equalisation at the OLT as the central enabling mechanism. The SOA provides ≥ 20 dB small-signal gain and regulates its gain with the instantaneous burst level, stabilising packet power before detection. This removes the need for large dynamic-range burst-mode TIAs, improves sensitivity within typical access power budgets, and avoids deep SOA saturation that would otherwise require the use of heavy DSP for nonlinear impairment mitigation[28], [29], [36]. In the O-band IM/DD case, this equalisation allows 100 Gb/s operation with multilevel PAM despite residual dispersion, SNR degradation, and limited component bandwidths. In the C-band coherent case, the same preamplified, burst-aware front end supports rapid acquisition in the presence of ONU laser frequency/phase drift and sustains higher spectral efficiency at manageable symbol rates. The in-depth architectural proposals and their comparative evaluations are presented in later chapters.

2.1 High-Capacity PON Techniques and Requirements

One effective approach to achieving higher data rates in PONs without increasing the symbol rate, or the required bandwidth, is to employ advanced modulation techniques that encode more bits per symbol. This is accomplished by transmitting data using multiple discrete levels of amplitude (e.g., PAM4), phase (e.g., QPSK), or even polarisation states (e.g., DP-QAM). By exploiting these additional physical dimensions of the optical signal, it is possible to significantly enhance spectral efficiency, enabling higher-speed transmission within the bandwidth constraints of existing optical components. This strategy is particularly attractive for next-generation access networks, where upgrading bandwidth is costly, but maximising the data throughput over the existing infrastructure is essential. These principles are applicable to both upstream and downstream PON transmission, although their practical implementation differs due to the continuous nature of downstream transmission and the burst-mode operation of the upstream.

This section explains how it is possible to achieve a higher data rate while maintaining the same symbol rate, as well as the associated trade-offs and functional requirements.

2.1.1 Functional Requirements

In designing solutions for next-generation PONs, compliance with the functional specifications defined by standardisation bodies such as ITU-T and IEEE is essential. These requirements are not merely performance benchmarks; they are fundamental to ensuring interoperability, reliability, and cost-effectiveness in large-scale deployments. This subsection outlines the critical parameters, sensitivity, power budget, and dynamic range, and discusses why achieving the specified targets is essential for the viability of any proposed system.

Receiver Sensitivity

Sensitivity is defined as the minimum optical power at the receiver input required to achieve a bit error rate (BER) at the FEC threshold. In the latest ITU-T G.9804 50G-PON standard for high-speed systems, this value is specified as –22.7 dBm (at the soft decision FEC (SD-FEC)). This ensures that even the weakest optical signals, attenuated by long fibre spans and multiple splitting stages, can still be

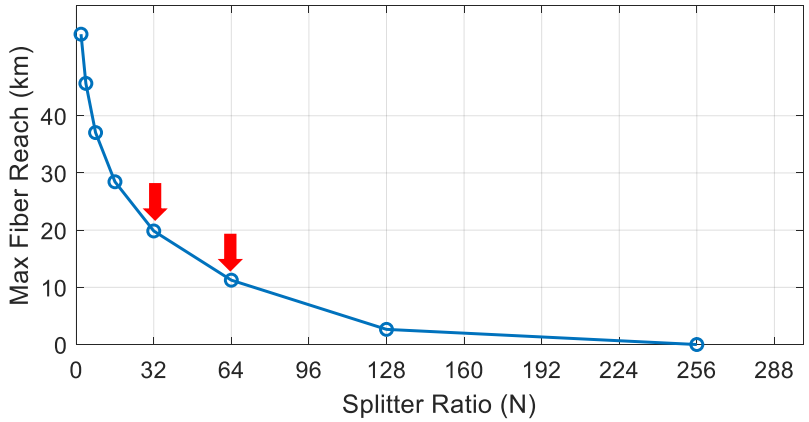


Figure 2.2: Maximum reach versus splitter ratio for given PON power budget of 29 dB.

recovered reliably. Insufficient sensitivity reduces the maximum allowable optical path loss, which in turn limits the network reach or split ratio. For cost-sensitive PON deployments, this is a critical constraint.

Several factors influence sensitivity including Modulation formats, fibre impairments, receiver bandwidth and optical amplification which will be discussed in the following sections.

Power Budget

The power budget represents the maximum allowable loss between the OLT transmitter and the ONU receiver, calculated by:

$$\text{Power budget } [dB] = P_{\text{launch}}\ [dBm] - P_{\text{sensitivity}}\ [dBm] \tag{2.1}$$

where P_{launch} is the transmitter launch power and must be between 9-11 dBm. This limitation is to ensure the system remains in the linear region of fibre transmission as will be discussed in subsection 2.2.4. For future high-speed PONs, the required budget is around 29 dB, taking into account losses from fibre, splitters, connectors, splices and extra margin. A higher power budget allows for higher split ratios (more users per OLT port) or longer reach, enabling cost-effective scaling without additional active equipment in the field. Figure 2.2 shows the relationship between split ratio and physical reach based on typical splitter loss characteristics assuming 29 dB power budget in C-band. With ideal 1:32 (adding ≈15 dB of insertion loss) and 1:64 (adding ≈18 dB of insertion loss) static split ratios, realistic operating ranges are roughly 20 km and 10 km respectively.

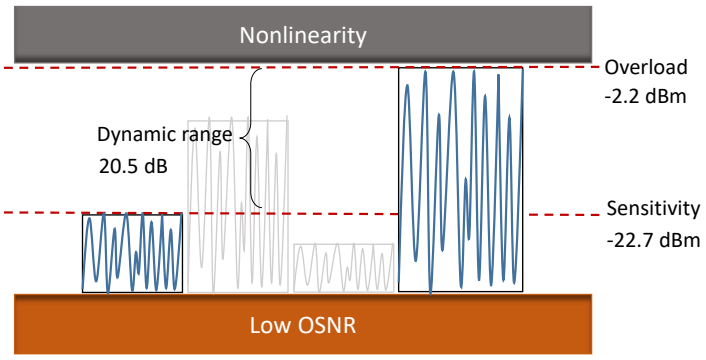


Figure 2.3: Dynamic range between "soft" and "loud" burst packets.

Dynamic Range

In a PON, upstream data from multiple ONUs is transmitted in short, time-slotted bursts. Each burst represents a packet of optical data that begins and ends within its allocated slot. Because ONUs are deployed at varying distances from the OLT and are subject to different optical losses, their bursts often reach the OLT with different power levels. This variability creates a challenge for the BMRx, which must quickly adapt to large power fluctuations between consecutive bursts while still ensuring error-free detection. Downstream PON transmission, however, typically employs continuous transmission from the OLT and therefore does not face the same burst-mode challenges as the upstream.

As illustrated in Figure 2.3, the BMRx must correctly process both the weakest incoming burst (the “soft” packet, limited by receiver sensitivity) and the strongest burst (the “loud” packet, bounded by overload tolerance). The dynamic range is therefore defined as the ratio between these two extremes, reflecting the receiver’s ability to accommodate burst-to-burst power variations. A narrow dynamic range would result in loss of weak signals or saturation by strong ones, while a sufficiently wide range ensures reliable operation across diverse deployment scenarios. According to the latest standard, with a sensitivity of –22.7 dBm and an overload threshold of –2.2 dBm, the BMRx achieves a dynamic range extending from 0 dB up to 20.5 dB.

2.1.2 IM/DD Pathway to Higher Speeds

In IM/DD PON, the conventional NRZ format transmits a single bit per symbol using two distinct optical intensity levels. While NRZ is simple to implement, it becomes inefficient as system data rates increase. To achieve higher bit rates with NRZ, the symbol rate must be increased proportionally. This directly increases the

required analogue bandwidth, which in turn is a key factor that increases system cost. This is a critical consideration in PONs, where, in contrast to most other optical network applications, transceiver cost is shared across a relatively small number of end users, only one in the case of the ONU. As a result, PON standards have historically developed with the aim of utilising the lowest possible analogue bandwidth optical and electronic components needed to achieve a given target bit rate. This has often been aided by leveraging components that have been developed for higher volume markets, such as data centres, to benefit from the cost reduction that results from the associated economies of scale.

A more bandwidth-efficient approach is to use multilevel modulation, where each symbol carries more than one bit by adopting multiple optical amplitude levels. This scheme is referred to as M-level pulse amplitude modulation (M-PAM). In M-PAM, the number of bits per symbol is given by:

$$\text{Bits per symbol} = \log_2(M). \tag{2.2}$$

In practical digital communication systems, M is typically chosen as a power of two so that each symbol conveys an integer number of bits, i.e., $\log_2(M) \in \mathbb{N}$. Increasing M allows more bits to be transmitted per symbol without increasing the symbol rate. Accordingly, the relationship between the bit rate R_b and the symbol rate R_s is

$$R_b = R_s \cdot \log_2(M) \tag{2.3}$$

For a fixed bit rate R_b, increasing M reduces the required symbol rate R_s, and hence the minimum one-sided baseband Nyquist frequency. Under ideal Nyquist signalling (zero excess bandwidth), the Nyquist frequency f_{Nyq} corresponds to the highest baseband frequency component of the transmitted signal and is equal to the minimum required one-sided baseband bandwidth. It is given by

$$f_{\text{Nyq}} = \frac{R_s}{2} = \frac{R_b}{2\log_2(M)} \tag{2.4}$$

The Nyquist bandwidth represents the minimum baseband bandwidth needed to transmit the signal without inter-symbol interference (ISI) when ideal pulse shaping is used. For example, to transmit $R_b = 100$ Gb/s:

- PAM4 (2 bits/symbol): $R_s = 50\,\text{Gbaud} \Rightarrow f_{\text{Nyq}} = 25\,\text{GHz}$
- PAM8 (3 bits/symbol): $R_s \approx 33.3\,\text{Gbaud} \Rightarrow f_{\text{Nyq}} \approx 16.7\,\text{GHz}$

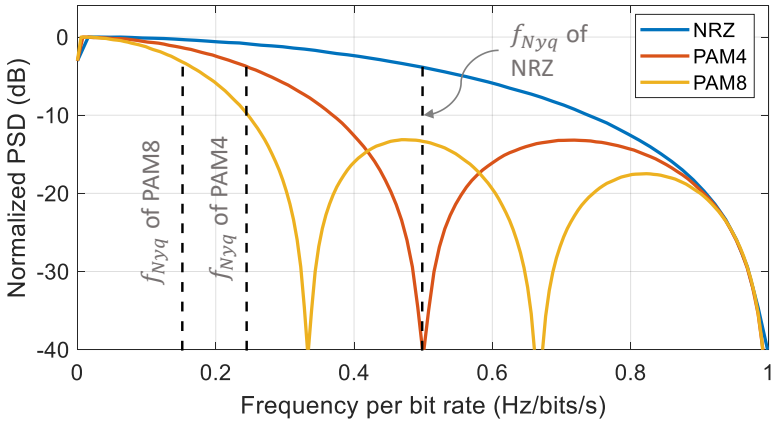


Figure 2.4: Power spectral density envelope for randomly-generated NRZ, PAM4, and PAM8 signal.

Thus, at the same bit rate, PAM8 requires only about two-thirds of the Nyquist frequency of PAM4, and one-third that of NRZ. This bandwidth compression reduces the demands on the analogue front end (AFE), electro-optic components, and high-speed data converters. In the context of PON transceivers, this can enable higher capacity per wavelength without proportionally increasing component speed.

In practice, multilevel signals are mapped to bit patterns using either natural binary or Gray coding. Gray coding is preferred in optical links because it minimises the bit error rate by ensuring that adjacent amplitude levels differ by only one bit. For PAM4, a typical Gray mapping is:

$$\{00, 01, 11, 10\}$$

corresponding to ascending optical intensity levels. For PAM8, the Gray mapping extends to three-bit symbols.

The impact of increasing M on the signal spectrum is illustrated in Figure 2.4, which shows the power spectral density (PSD) versus frequency for NRZ, PAM4, and PAM8 at the same baud rate of 50 Gbaud. The vertical dashed lines mark the Nyquist frequencies for each format. As M increases, the PSD narrows and the Nyquist frequency decreases, reflecting the reduced symbol rate for the same bit rate. For example, PAM4's Nyquist frequency is half of NRZ, a 50% reduction in occupied bandwidth. This spectral narrowing directly corresponds to an increase

in spectral efficiency, defined as:

$$\eta = \frac{R_b}{B} \quad [\text{bits/s/Hz}], \tag{2.5}$$

where B denotes the occupied one-sided baseband bandwidth. Under ideal Nyquist signalling, B is numerically equal to the Nyquist frequency, i.e., $B = f_{\text{Nyq}}$, and the resulting spectral efficiencies are $\eta = 1, 2,$ and 3 bits/s/Hz for NRZ, PAM4, and PAM8 signals, respectively. The figure makes clear that for a given channel bandwidth, increasing M proportionally increases the achievable bit rate. In other words, multilevel modulation formats increase the capacity of IM/DD PON links without exceeding practical symbol-rate and bandwidth limits. However, this increase in spectral efficiency comes with tradeoffs that are explained later in the following sections.

2.1.2.1 Performance Metrics in IM/DD

The performance of an optical transmission link is fundamentally defined by its ability to deliver the transmitted information with high fidelity. Any errors introduced into the original data sequence, whether during modulation, propagation, or reception, directly degrade link quality. Performance metrics therefore quantify how accurately the received signal represents the transmitted data and provide a basis for evaluating and comparing transmission systems. In this thesis, the following metrics are used to assess IM/DD system performance.

Signal to Noise Ratio

In digital communication, the received signal is always impaired by noise, which limits the ability of the receiver to reliably distinguish between modulation symbols. A common measure of transmission quality is the signal-to-noise ratio (SNR), defined as the ratio of the average received signal power to the average noise power within the detection bandwidth. For a general M-PAM format, the SNR can be expressed by comparing the average symbol power to the cumulative noise variance affecting the detected signal. As M increases, the required SNR for reliable detection also increases, since the distance between adjacent levels becomes smaller.

In receivers, the effective noise variance arises from several physical mechanisms. Thermal noise, originating in the electrical circuitry, dominates at low received powers. Shot noise, due to the statistical nature of photo-detection, scales with

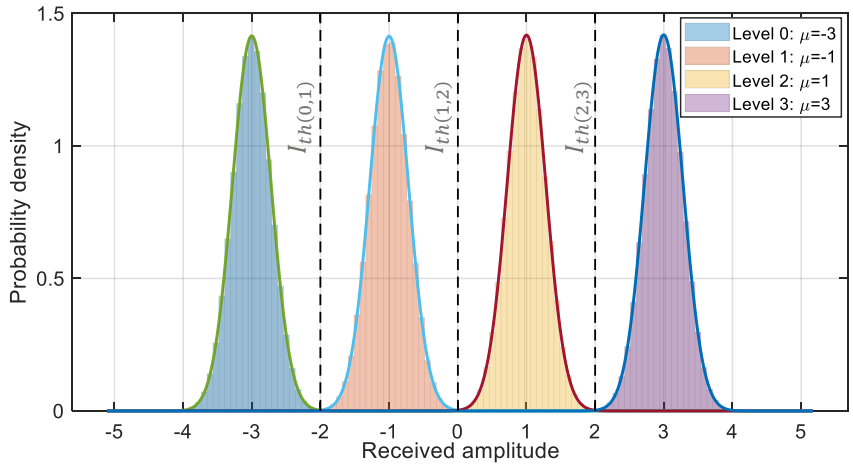


Figure 2.5: Example of BER estimation for PAM4 using Gaussian PDFs. Histograms of received samples (bars) are overlaid with Gaussian fits (curves). Vertical dashed lines indicate decision thresholds. The shaded regions represent the probability of error for each level.

optical power. If an optical pre-amplifier is employed, amplified spontaneous emission (ASE) noise also contributes significantly. The combined effect of these noise sources determines the achievable SNR and, ultimately, the performance limits of the transmission system.

Bit Error Rate

One of the most widely used performance measures is the BER, defined as the ratio of incorrectly detected bits n_e to the total number of transmitted bits n_b. In optical systems, BER can be evaluated either through direct error counting in a long data sequence by

$$BER_{\text{counting}} = \frac{n_e}{n_b} \tag{2.6}$$

or estimated from statistical models of the received signal. In this thesis, both counting and stochastic errors are reported.

Measuring the BER directly by error counting, when targeting very low BER values (e.g., 10^{-6} or below), requires transmitting an extremely large number of bits to collect sufficient errors for statistical confidence. An alternative approach is to estimate BER from a statistical model of the received signal levels. In IM/DD systems, noise at the decision circuit can often be approximated as additive white Gaussian noise (AWGN). Under this assumption, the received amplitude x conditioned on transmitting symbol i is Gaussian with mean μ_i and variance σ_i^2,

with probability density function (PDF)

$$p_i(x) = \frac{1}{\sqrt{2\pi\sigma_i^2}} \exp\left(-\frac{(x-\mu_i)^2}{2\sigma_i^2}\right), \quad i = 0, 1, \ldots, M-1. \tag{2.7}$$

In an ideal M-PAM system with equally spaced levels, the decision threshold between two adjacent levels i and $i+1$ is placed midway between their means:

$$T_{i,i+1} = \frac{\mu_i + \mu_{i+1}}{2}, \quad i = 0, 1, \ldots, M-2. \tag{2.8}$$

More generally, if the variances differ, the optimal thresholds can shift to minimise the total error probability.

Let define the decision region for symbol i as $(T_{i-1,i}, T_{i,i+1})$, using the boundary conventions $T_{-1,0} = -\infty$ and $T_{M-1,M} = +\infty$. The conditional symbol error probability is the probability that x falls outside the decision region:

$$P_{\text{err},i} = 1 - \int_{T_{i-1,i}}^{T_{i,i+1}} p_i(x)\, dx = \int_{-\infty}^{T_{i-1,i}} p_i(x)\, dx + \int_{T_{i,i+1}}^{+\infty} p_i(x)\, dx. \tag{2.9}$$

Assuming equal probability for symbols, the symbol error rate (SER) is given by

$$\text{SER} = \frac{1}{M} \sum_{i=0}^{M-1} P_{\text{err},i}. \tag{2.10}$$

With Gray mapping, adjacent levels differ by one bit and, at moderate/high SNR, errors are typically dominated by nearest-neighbour decisions. Under this condition, a symbol error usually produces one bit error, giving the common approximation

$$\text{BER} \approx \frac{\text{SER}}{\log_2 M}. \tag{2.11}$$

This approximation becomes less accurate when non-adjacent symbol errors are significant (e.g., low SNR, strong ISI, or nonlinear distortion).

Eye Diagram

An eye diagram is a time-domain tool that overlays many symbol intervals of the received waveform on the same horizontal time axis. The result shows the eye opening, which indicates how much vertical and horizontal margin the receiver has for making correct decisions. In an IM/DD system with M-PAM, there are $M-1$ separate eyes: one eye between each adjacent pair of amplitude levels.

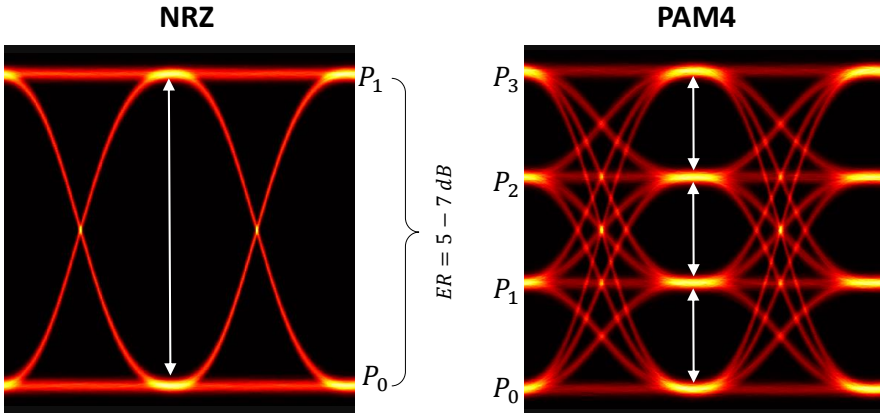


Figure 2.6: Eye diagrams of NRZ and PAM4 with normalised vertical full swing level. Arrows indicate the level-to-level amplitude differences in each eye diagram.

A larger vertical opening and a wider horizontal opening (larger timing margin) reduce BER. For M-PAM, the vertical separations between adjacent levels shrink as M grows, so the eyes close vertically. Conversely, higher M reduces the required symbol rate at a fixed bit rate, which relaxes bandwidth limits that would otherwise cause horizontal closure due to ISI. Eye diagrams therefore visualise the same trade-offs seen in the PSD and Nyquist-frequency analysis.

Figure 2.6 shows ideal eye diagrams for NRZ and PAM4 in the absence of channel impairments. In this thesis, the NRZ eye is analysed to ensure the extinction ratio (ER) which is defined as $ER = P_1/P_0$ falls within 5–7 dB, as specified in the latest 50G-PON standard. For higher-order modulation formats, the vertical eye opening between adjacent levels should be balanced. In case a level mismatch is observed, the symbol amplitudes should be adjusted to restore equal eye heights and improve signal quality.

2.1.2.2 Tradeoffs and Limitations

Multilevel signals like PAM4 exhibit a reduced eye opening at each level, equal to $1/(M-1)$ of the binary case, making them more vulnerable to noise, dispersion, and nonlinearities. The SNR requirement is higher than binary signalling, which affects the receiver sensitivity. In an ideal ISI-free M-PAM system, and considering a thermal noise-limited PIN receiver with equivalent noise current of $I_{\text{noise}}[\text{pA}/\sqrt{Hz}]$, the sensitivity of the reference system is calculated based on

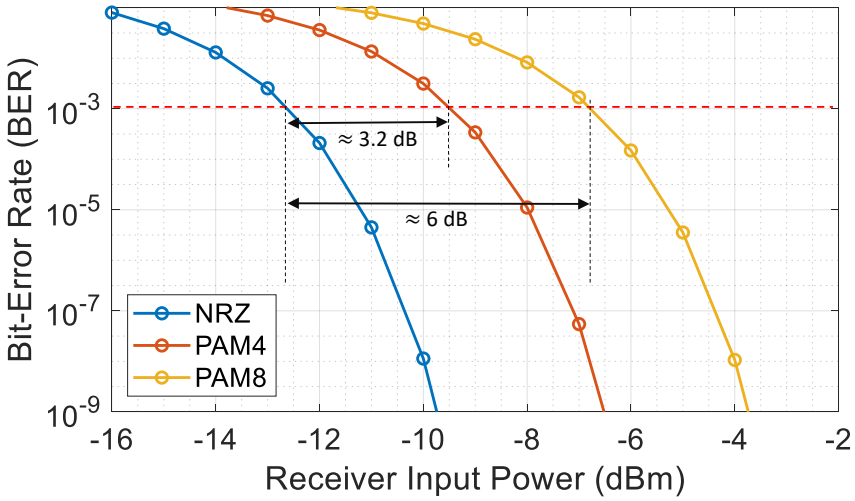


Figure 2.7: Modulation level impact on receiver sensitivity.

the target BER [37].

$$P_{ref} = \sqrt{\frac{R_b N_0 (M-1)^2}{2R^2 \log_2 M}} Q^{-1}\left(\frac{M \log_2 M \times \text{BER}_{\text{target}}}{2(M-1)}\right), \quad N_0 = I_{\text{noise}}^2 \tag{2.12}$$

where R_b is the bit rate and R is the photodiode responsivity. For example, as shown in Figure 2.7, assuming a typical receiver noise current of 40 pA/$\sqrt{Hz}$ and a responsivity of 0.5 A/W, the receiver sensitivity for an NRZ signal at a target bit error rate of $\text{BER}_{\text{target}} = 10^{-3}$ and bit rate of 100 Gb/s is about -12.5 dBm.

For a system dominated by signal-independent noise, such as thermal noise, receiver sensitivity is inversely proportional to the eye opening. Thus, as shown in the figure, the sensitivity power penalty of M-ary compared to binary can be approximated as:

$$P_{\text{penalty}} = \frac{M-1}{\sqrt{\log_2(M)}} \tag{2.13}$$

However, optical amplification, as it will be discussed in Subsection 2.2.5, with a sufficient gain can compensate for this penalty.

Furthermore, at higher order modulation formats, the linearity of the transmission path, including optical amplifiers and transimpedance amplifiers, becomes more critical. As a result, performance is often limited by ISI, receiver noise, and nonlinear distortions, particularly when operating close to the optical power budget limits. Therefore, simply increasing the number of amplitude levels is not a practical route to higher data rates and more advanced schemes are required.

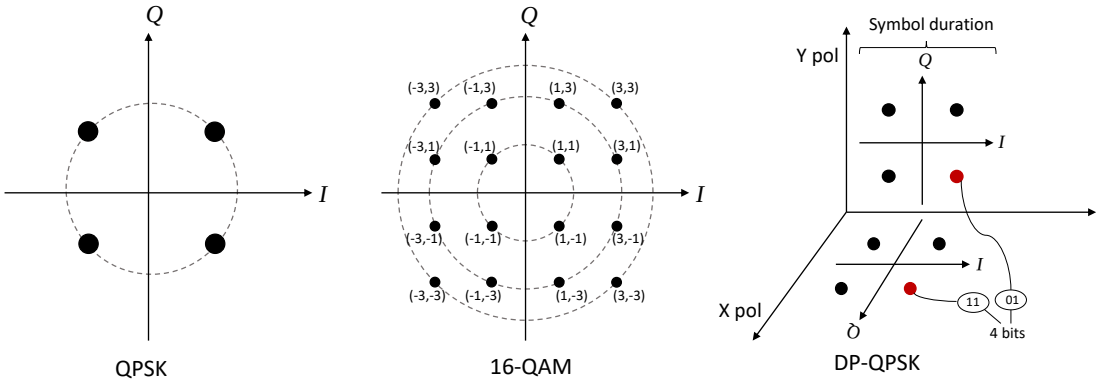


Figure 2.8: Constellations of the inphase and quadrature phases of lightwave carrier under modulation formats QPSK, 16QAM with three rings, and dual polarisation QPSK.

2.1.3 Scaling Capacity by Coherent Technology

Compared with IM/DD PON, where data is carried only in the signal's amplitude (intensity), coherent PON (CPON) uses multiple modulation dimensions—amplitude, phase, and polarisation—to increase capacity and reach. In CPON, advanced formats enable higher spectral efficiency, allowing more bits per symbol in the same optical bandwidth. With Nyquist shaping, dual polarisation QPSK (DP-QPSK) at 25–32 Gbaud can deliver about 100 Gb/s per wavelength, while DP-16QAM at 16–20 Gbaud can achieve the same capacity in less bandwidth or scale up to 200–400 Gb/s per wavelength.

Figure 2.8 shows constellation diagrams for QPSK, 16QAM, and DP-QPSK. QPSK carries 2 bits per symbol within a similar spectral footprint, while 16QAM carries 4 bits per symbol. Dual-polarisation schemes (e.g., DP-QPSK) effectively double this again by using two orthogonal polarisations in the same wavelength channel. The power spectral density plots (Figure 2.9) illustrate how higher-order QAM formats maintain similar occupied bandwidth while carrying more information. Dual polarisation achieves a further 3 dB gain, effectively doubling the spectral efficiency without increasing the occupied bandwidth. For instance, employing DP-16QAM with a spectral efficiency of 8 bits/s/Hz over a 50 GHz channel yields a net data rate of 400 Gb/s.

Recent experimental demonstrations using 16QAM have achieved optical power budgets in the range of 29–35 dB over 20–40 km fibre, depending on receiver architecture and FEC overhead [38], [39]. The CableLabs CPON architecture specification likewise targets up to 35 dB budget, which enables high-split ratios such as 1:512 at 20 km [40].

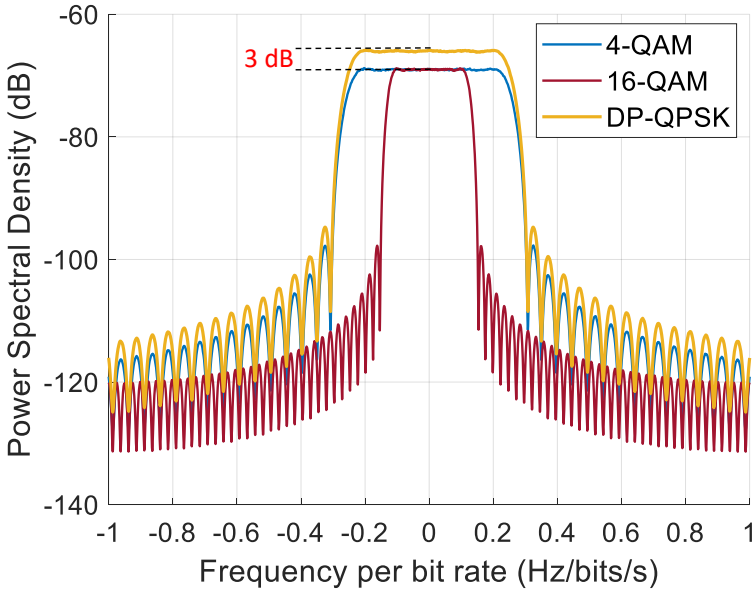


Figure 2.9: PSD of randomly generated 4QAM (QPSK), 16QAM, and DP-QPSK at the same bit rate.

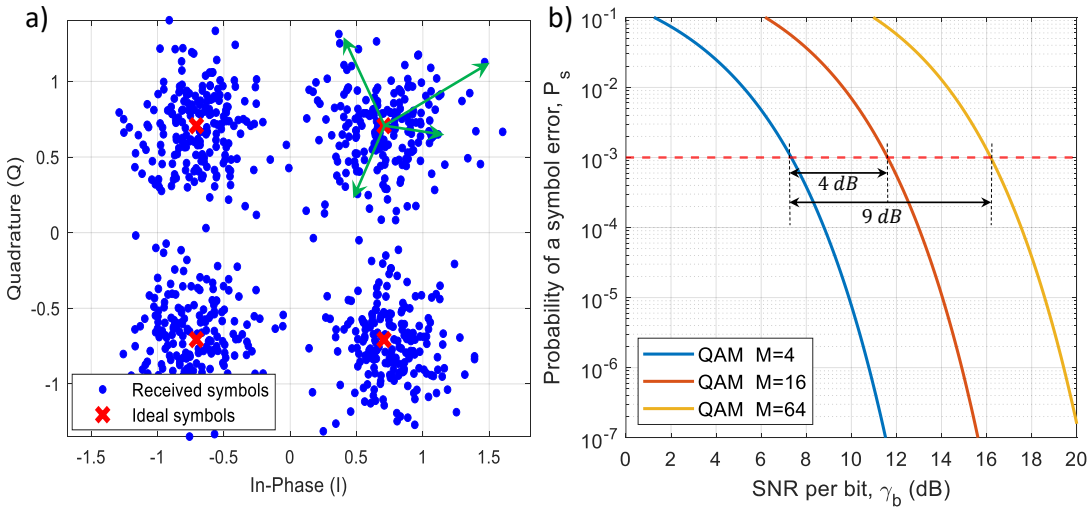


Figure 2.10: (a) Constellation diagram with error vectors (green). EVM is computed as the RMS distance normalised to the reference symbol power. (b) Symbol error probability for M-QAM, plotted using the expression in [41].

Performance Metrics

In coherent detection systems, performance is commonly characterised using error vector magnitude (EVM) and BER, which quantify modulation accuracy and system reliability, respectively. As illustrated in Figure 2.10.(a), EVM measures the root-mean-square (RMS) distance between received constellation points and their ideal locations, normalised to the average symbol power. Since these de-

viations are primarily caused by noise and linear impairments, EVM provides a direct measure of modulation quality in coherent receivers. For an ideal coherent system operating over an AWGN channel, EVM can be directly related to the SNR. Under standard normalisation assumptions and for sufficiently large symbol streams, the RMS EVM is given by

$$\text{EVM}_{rms} = 1/\sqrt{\text{SNR}}. \tag{2.14}$$

BER complements EVM by characterising reliability at the bit level. Figure 2.10.(b) shows the BER performance of M-QAM modulation schemes as a function of SNR, demonstrating that higher modulation orders require increased SNR to maintain a given target BER due to the reduced Euclidean distance between constellation points. Analytical relationships between EVM and BER have been established for AWGN channels, allowing BER to be inferred from measured EVM values [42].

In practice, EVM measurements are widely used to estimate BER at very low error rates, where direct BER testing would require prohibitively long measurement times.

2.2 Physical Layer Impairments

In PONs, the demand for higher bit rates and longer transmission distances introduces significant challenges at the physical layer, arising from limitations in both optoelectronic components (transmitters, receivers, and optical amplifiers) and optical fibre propagation. This section examines the dominant physical-layer factors affecting PON performance, including BM-TIA constraints, receiver bandwidth limitations, noise sources, fibre optic impairments, and optical amplification. While the discussion is framed in the context of upstream transmission, many of the physical layer impairments considered are also relevant to downstream PON operation. To analyse these effects, MATLAB-based simulation setups shown in Figure 2.11 are employed: Figure 2.11.(a) investigates chromatic dispersion and bandwidth limitations in M-PAM IM/DD systems, and Figure 2.11.(b) examines the impact of chromatic dispersion and phase noise on coherent M-QAM constellations. Detailed descriptions of the simulation setups are provided in the corresponding sections.

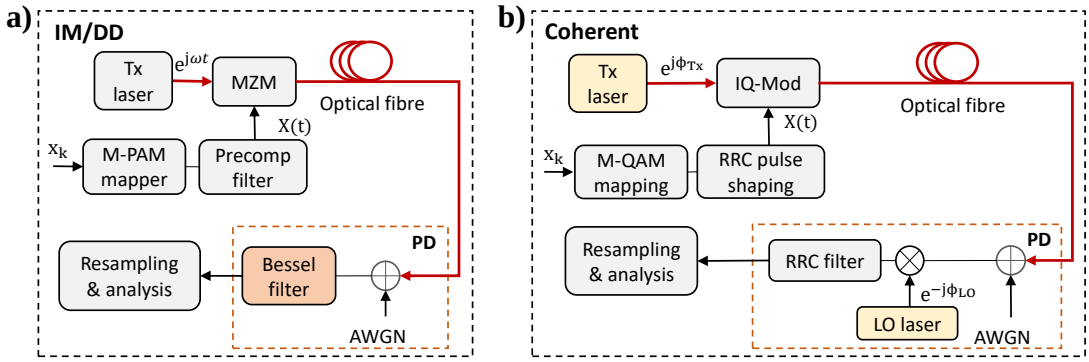


Figure 2.11: (a) IM/DD simulation setup for receiver bandwidth and chromatic dispersion analysis of M-PAM signals. (b) Baseband-equivalent coherent M-QAM simulation model for phase-noise and chromatic dispersion analysis.

2.2.1 Burst Power Equaliser: Transimpedance Amplifier

The conventional approach to address the 20.5 dB dynamic range of upstream packets is to use BM-TIAs. To enable high-speed data transmission, the Silicon–Germanium Bipolar Complementary Metal–Oxide–Semiconductor (SiGe BiCMOS) process is essential for BM-TIA IC fabrication due to its superior high cut-off frequency, low noise characteristics, and fast transient response. This technology integrates high-speed SiGe heterojunction bipolar transistors (HBTs) with CMOS devices, enabling high-bandwidth, low-noise, and highly sensitive receiver front-ends, making it well suited to meet the optical budget requirements of PON applications [43]. However, these performance benefits come at the cost of increased fabrication complexity and higher production expenses compared to traditional CMOS processes. In addition, handling a large dynamic range in the receiver necessitates precise automatic gain and offset control circuits for the TIA, as well as a series of variable gain amplifiers as shown in Figure 2.12. These circuits are essential for regulating the output swing to a constant level but introduce considerable design complexity. The challenge becomes even more pronounced as the receiver bandwidth exceeds 10 GHz, where achieving stable DC offset and gain adjustment while maintaining constant bandwidth becomes increasingly difficult [44]. These factors complicate the practical implementation of BM-TIAs in high-speed PON. The latest state-of-the-art achieves a 15.4 dB dynamic range at SD-FEC threshold for a 100 Gb/s PAM4 PON [19]. This design maintains a total harmonic distortion of less than 5% —an industry-agreed specification for linear optical receivers [45]— but only for bursts with peak-to-peak input powers below -6 dBm, highlighting the constraints of BM-TIA designs in supporting a larger dynamic range.

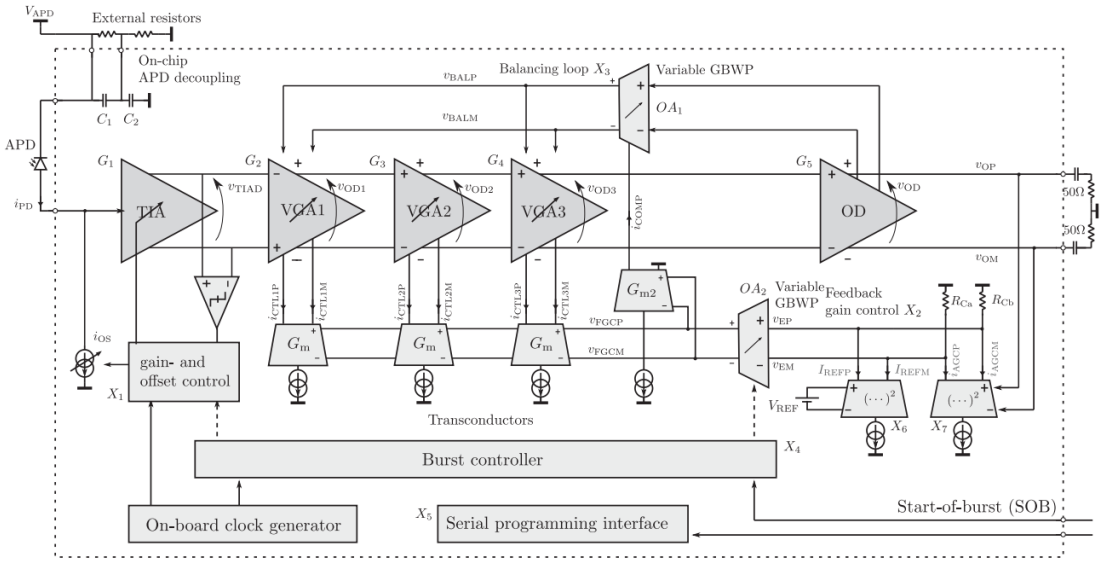


Figure 2.12: The latest state-of-the-art BM-TIA architecture [19]

There is a trade-off between the gain and the bandwidth of a TIA. In SiGe HBT-based TIAs, this trade-off is fundamentally rooted in the physics of charge storage and carrier transit in bipolar devices. Transimpedance gain is achieved by modulating the collector current through variations in the base–emitter voltage, which inherently involves storing and removing charge in the base region. Therefore, increasing gain requires larger signal-dependent variations in stored base charge, leading to increased diffusion capacitance [46]. However, the rate at which this charge can be injected and extracted is limited by carrier transit time and recombination processes, which are determined by device geometry and bias current and ultimately constrain the high-frequency response of the HBT. As frequency increases, an increasing fraction of the device current is consumed in charging internal junction and diffusion capacitances rather than contributing to signal amplification, causing the available gain to roll off and resulting in an approximately constant gain–bandwidth product [47]. This physical limitation manifests in practice as reduced bandwidth at high gain levels and becomes especially pronounced in linear, high-speed, and burst-mode TIAs, where large dynamic range and fast transient response are simultaneously required [48].

This trade-off limits the dynamic range that a BM-TIA can equalise, especially at higher symbol rates. For instance, the most recent state-of-the-art implementation, as shown in Figure 2.13, achieved a normalised 6 dB bandwidth of 17.1 GHz at sensitivity level and 24.6 GHz at overload level.

This thesis proposes burst power equalisation in the optical domain for 100 Gb/s

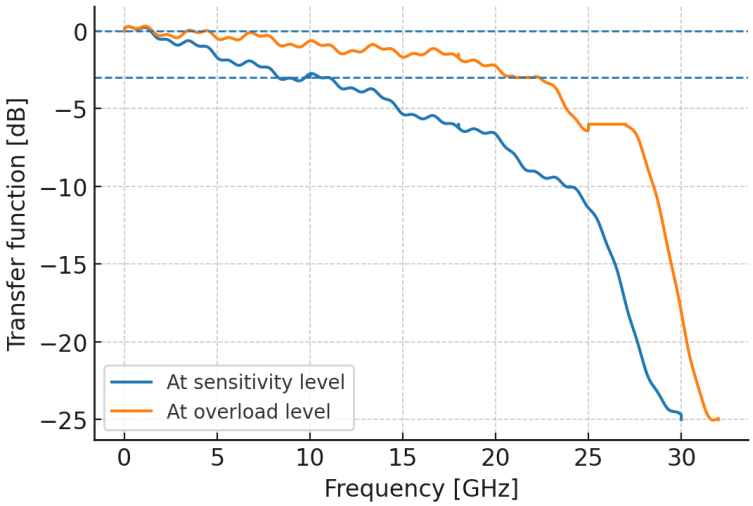


Figure 2.13: Frequency response of the entire transmission system using BM-TIA at sensitivity and overload levels (redrawn based on [49]).

PON that effectively addresses these issues. By regulating a wide range of input power level to the receiver, this approach reduces the need for a high-gain TIA, which can impose bandwidth limitation in the receiver design. Furthermore, it bypasses the need for complex automatic gain and offset control circuits, simplifying the receiver design. Although the approach requires additional components for SOA gain control, these are less challenging to design and are located at the OLT, where the associated costs can be shared among multiple users.

2.2.2 Bandwidth Limitation

Bandwidth limitations in PON transceivers arise from constraints in the optoelectronic components, including AFE, TIAs (as mentioned earlier), modulators, and associated electronic circuitry. These limitations introduce low-pass filtering effects that distort transmitted signals, reducing their spectral integrity and ultimately degrading system performance.

IM/DD

The limited bandwidth of the frequency response of the optoelectronic devices at the transmitter and receiver limits the symbol rate of the data signal that can be supported without introducing a high amount of ISI and the consequent degradation in performance. The bandwidth-critical components in a PON are generally the electronic driver circuitry and modulator at the transmitter, and the photodiode and TIA at the receiver. This thesis focuses mainly on the receiver

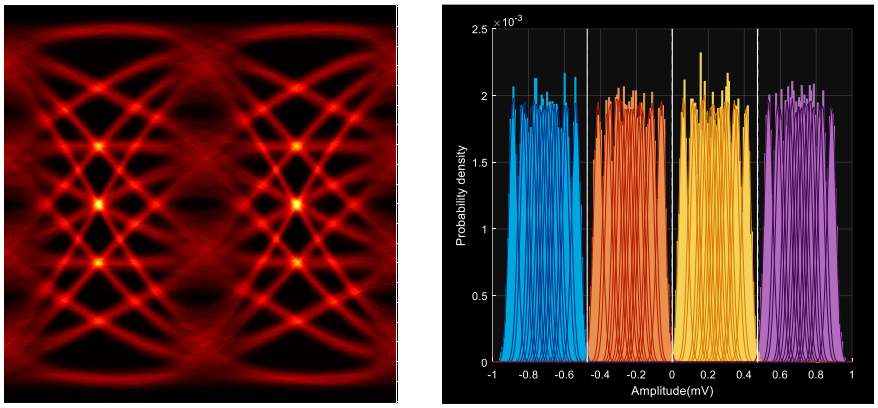


Figure 2.14: Eye diagram and histogram of a simulated 100 Gb/s PAM4 transmission after applying 18.75 GHz Bessel filter.

side and considers an ideal transmitter. Therefore, only the receiver bandwidth limitation has been taken into account.

In IM/DD systems, future solutions must employ low-cost 25G class receivers, for which the limited receiver bandwidth acts as a low-pass filter that attenuates the high-frequency components of the modulated signal, causing temporal pulse spreading and resulting in ISI. In this thesis, an 18.75 GHz fourth-order Bessel filter (3 dB bandwidth) is used to model the receiver bandwidth limitation at the electrical receiver front-end, representing the combined photodiode and TIA response. A 50 Gbaud PAM4 waveform is simulated with 12 samples per symbol, and AWGN is applied at the receiver input. As shown in Figure 2.14, the bandwidth limitation leads to pronounced eye closure, where overlapping symbol transitions reduce the vertical eye opening and increase amplitude uncertainty at the sampling instant. The corresponding histogram further illustrates this effect through significant broadening and overlap between adjacent PAM4 levels compared to the ideal case. This increased level overlap results in a higher probability of decision errors and thus an elevated BER, demonstrating that receiver bandwidth limitation is a dominant performance bottleneck in high-speed IM/DD systems. Mitigation therefore relies on equalisation, with a 13-tap linear FFE employed to partially recover the attenuated high-frequency components.

Coherent

In coherent PON systems, AFE, comprising the optical hybrid, balanced photodiodes, and analogue-to-digital converters (ADCs), determines the effective system bandwidth and thus plays a critical role in overall system performance. Insufficient AFE bandwidth introduces frequency-dependent attenuation and

pulse shaping distortion, leading to symbol broadening and a loss of orthogonality in higher-order QAM constellations. This impairment manifests as increased EVM and a receiver sensitivity penalty, particularly for spectrally efficient modulation formats. While coherent DSP enables powerful adaptive equalisation to mitigate bandwidth-induced distortions, severe bandwidth limitations fundamentally constrain achievable performance and require longer equalisers with increased computational complexity and power consumption. These bandwidth–performance–complexity trade-offs have been extensively studied in coherent optical systems and coherent access networks as investigated in [50], [51], [52].

2.2.3 Noise Sources

In the absence of optical preamplification, receiver performance is fundamentally limited by noise originating within the receiver itself. Two primary noise sources are common to both IM/DD and coherent receivers: thermal noise arising from the front-end electronics and shot noise associated with the photodetection process. The magnitude of these noise contributions and the manner in which they affect SNR, receiver sensitivity, and overload behaviour depend on the receiver architecture. In what follows, their impact is quantified separately for IM/DD and coherent detection.

Thermal noise and shot noise arise from independent physical mechanisms, and their corresponding noise variances. For a given detected signal, their combined effect may therefore be described by an additive-noise-limited SNR, expressed as

$$\mathrm{SNR}_{\mathrm{add}}^{-1} = \mathrm{SNR}_{\mathrm{th}}^{-1} + \mathrm{SNR}_{\mathrm{sh}}^{-1}. \tag{2.15}$$

When one noise contribution dominates, the receiver operates in the corresponding noise-limited regime.

In addition to these additive noise sources, coherent receivers are affected by laser phase noise, which introduces performance degradation through random phase fluctuations in the detected signal. In IM/DD systems, square-law detection removes the optical phase, so laser phase noise does not directly impair detection and is therefore neglected. Although spontaneous emission and other laser nonidealities also give rise to laser intensity fluctuations (relative intensity noise), these effects are not considered here, as the IM/DD analysis is restricted to thermal and shot noise, which dominate in the operating regimes of interest.

Noise arising from spontaneous emission in optical amplifiers (ASE) is treated separately as an additive noise source, as discussed in Subsection 2.2.5.

Receiver Thermal Noise

In IM/DD optical receivers, thermal noise is a fundamental limitation on sensitivity, particularly when it dominates over other noise sources. It originates from the resistive elements in the receiver front-end as well as from the intrinsic noise contribution of the TIA. Unlike signal-dependent noise mechanisms, thermal noise is independent of the received optical power but scales directly with the receiver's electrical bandwidth, becoming more severe as higher data rates are supported. The mean-square thermal noise current can be expressed as [53]

$$\sigma_{\text{th}}^2 = \frac{4k_B T_0}{R_L} F_n B, \tag{2.16}$$

where k_B is Boltzmann's constant, T_0 is the absolute temperature, R_L is the effective load resistance, F_n is the amplifier noise figure, and B is the noise-equivalent bandwidth.

In IM/DD systems, the detected signal current is proportional to the received optical power, $I_{\text{sig,IMDD}} = RP_r$, where R is the photodiode responsivity, and P_r is the received signal power. Since the thermal noise variance is independent of P_r, increasing the received power improves performance in the thermal-noise-limited regime until shot noise becomes dominant. This behaviour defines the thermal-noise-limited SNR contribution, SNR_{th}, for IM/DD receivers.

In coherent optical receivers, thermal noise also arises in the front-end electronics of each detection branch and constitutes a limiting factor in sensitivity, particularly when the LO power is not sufficiently strong to move the receiver into the shot-noise-limited regime. For a balanced homodyne or intradyne configuration, the differential photocurrent scales with the product of the received signal field and the LO field, leading to a signal current amplitude proportional to

$$2R\sqrt{P_{\text{LO}} P_r}, \tag{2.17}$$

where P_{LO} is the LO power. Since each photodiode branch contributes thermal noise independently, the differential noise variance is twice that of a single-ended IM/DD.

Importantly, while the thermal noise remains independent of the LO power, the

coherent signal amplitude increases with $\sqrt{P_{\mathrm{LO}}}$. Consequently, increasing the LO power increases the thermal-noise-limited SNR contribution ($\mathrm{SNR}_{\mathrm{th}}$) for coherent receivers, shifting the operating point toward the shot-noise-limited regime in the overall SNR model.

Receiver Shot Noise

Shot noise originates from the Poisson statistics of photo-electron arrivals at the photodiode and, unlike thermal noise, it is signal dependent. In IM/DD systems, the resulting shot-noise variance is proportional to the average photocurrent and can be expressed as

$$\sigma^2_{\mathrm{sh,IMDD}} = 2qRP_rB, \tag{2.18}$$

where q is the electronic charge. This linear dependence indicates that the shot-noise level increases proportionally with the received optical power, in contrast to thermal noise which is power independent. Thus, in shot-noise-limited IM/DD systems, proportional scaling of signal and noise with received power defines the shot-noise-limited SNR contribution, $\mathrm{SNR}_{\mathrm{sh}}$, in the overall SNR model.

In coherent receivers, the presence of the LO changes the shot-noise scaling relative to IM/DD. For a balanced homodyne or intradyne configuration, each photodiode branch detects an average optical power proportional to $(P_{\mathrm{LO}}+P_r)/2$, so the total differential shot-noise variance is

$$\sigma^2_{\mathrm{sh,coh}} = 2qR(P_{\mathrm{LO}} + P_r)B. \tag{2.19}$$

Using the differential signal current introduced in the thermal-noise analysis, and assuming perfect phase and frequency alignment, the resulting shot-noise-limited electrical SNR is

$$\mathrm{SNR}_{\mathrm{sh,coh}} = \frac{RP_{\mathrm{LO}}P_r}{qB(P_{\mathrm{LO}} + P_r)}. \tag{2.20}$$

For $P_{\mathrm{LO}} \gg P_r$it saturates to an LO-independent limit:

$$\mathrm{SNR}_{\mathrm{sh,coh}} \to \frac{RP_r}{qB}$$

Thus, once the LO power is sufficiently large, further increases in P_{LO} do not improve performance and the receiver operates in the shot-noise-limited regime.

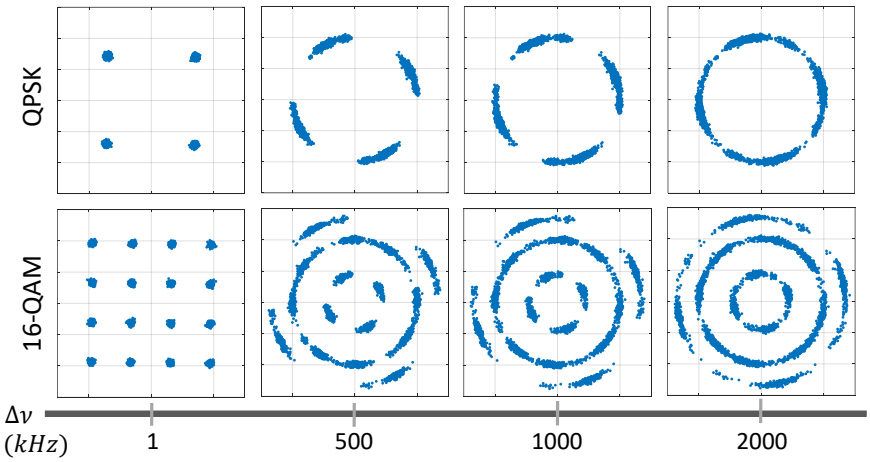


Figure 2.15: Simulated phase-noise-induced distortion of QPSK and 16QAM constellations at a symbol rate of 50 Gbaud for different transmitter and LO laser linewidths.

Phase Noise

Phase noise in coherent transmission arises from the finite linewidths of the transmitter laser, $\Delta\nu_{\mathrm{Tx}}$, and the LO laser, $\Delta\nu_{\mathrm{LO}}$. For standard Lorentzian lasers, the phase evolves as a Wiener process. Over one symbol of duration T_s, the common phase increment has variance

$$\sigma_\phi^2 \;=\; 2\pi\,(\Delta\nu_{\mathrm{Tx}} + \Delta\nu_{\mathrm{LO}})\,T_s. \tag{2.21}$$

Thus, the relevant design quantity is the product $(\Delta\nu_{\mathrm{Tx}} + \Delta\nu_{\mathrm{LO}})T_s$. Larger constellations (e.g., 16QAM) are more sensitive than QPSK because their decision regions are smaller, but both formats experience the same underlying phase rotation and cluster broadening. Figure 2.15 presents simulated received constellations at 50 Gbaud in the presence of laser phase noise, prior to carrier phase estimation. The simulated constellations are obtained using the simplified coherent baseband model introduced at the beginning of this section (see Figure 2.11). QPSK and 16QAM symbol sequences are generated and normalised to unit average power. Laser phase noise from the transmitter and local oscillator is modelled as a Wiener process with a combined linewidth $(\Delta\nu_{\mathrm{Tx}} + \Delta\nu_{\mathrm{LO}})$ producing a random phase rotation that evolves from symbol to symbol. AWGN is included to represent receiver noise, while fibre propagation effects are not considered in order to isolate the impact of phase noise. Increasing the combined transmitter and LO linewidth increases the phase-noise variance, resulting in progressive smearing of the constellation points. At about 1 kHz linewidth, QPSK and 16QAM form near-ideal constellations.

Mitigation is performed entirely in the coherent receiver DSP by compensating for frequency offset of the signal, as will be discussed in Subsection 2.3.2.

2.2.4 fibre Optic Degradations

Signal transmission in PONs is limited by fibre impairments that worsen with higher speeds and longer distances. The dominant issue is dispersion, mainly chromatic and polarisation-mode, which broadens optical pulses and leads to ISI. Nonlinear effects, such as self-phase modulation, further distort amplitude and phase, particularly at high power levels. This section reviews the key impairments that degrade IM/DD and coherent PON performance, highlighting their impact on system reliability as network capacity scales.

Effects of fibre attenuation

Attenuation is the monotonic loss of optical power with distance and directly constrains reach and split ratio in PON. For a fibre span of length L, the wavelength-dependent loss coefficient $\alpha(\lambda)$ (dB/km) relates input and output powers by

$$P_{\text{out}} = P_{\text{in}}\ 10^{-\alpha(\lambda)L/10}. \tag{2.22}$$

In the O-band (1260–1360 nm), typical installed G.652.D fibres exhibit $\alpha \approx 0.32 - 0.36$ dB/km at 1310 nm. In the C-band (1530–1565 nm), attenuation approaches the silica minimum with $\alpha \approx 0.18 - 0.22$ dB/km around 1550 nm. For realistic deployed fibre lengths, the higher attenuation of O-band compared to C-band is non-negligible. For example, over 20 km of fibre, O-band incurs about 2–3 dB more loss than C-band, which ultimately impacts the link power budget.

Engineering practice budgets end-to-end loss as

$$\mathcal{L}_{\text{path}}(\lambda) = \alpha(\lambda)L + \sum \mathcal{L}_{\text{events}} + \mathcal{L}_{\text{margin}}, \tag{2.23}$$

where event terms represent splices and connector pairs (typically a few tenths of a dB each) and the margin covers ageing and repairs.

fibre nonlinearity: stimulated Brillouin scattering (SBS)

SBS limits the maximum launch power in PONs. When the optical field is too strong, it excites an acoustic wave in the fibre. Part of the signal is then shifted in frequency and sent back toward the transmitter (the Stokes wave). This

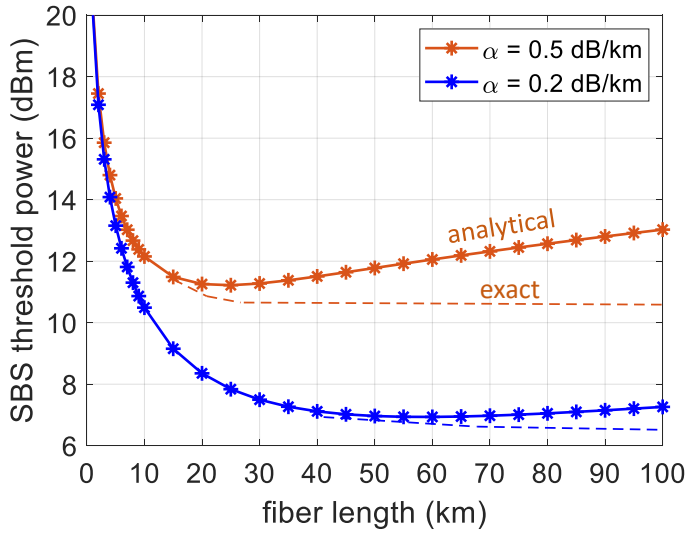


Figure 2.16: SBS threshold power in standard single-mode fibre. Solid lines show the analytical SBS threshold P_{th} evaluated using Equation (2.24). Dashed curves indicate representative reference values inferred from the exact noise-initiated theory reported in [54] and are included for qualitative comparison.

backscatter reduces the forward power and raises noise. The effect appears even on short links (about 10–20 km) when narrow-line lasers and standard single-mode fibres (SMFs) are used.

A convenient estimate of the SBS threshold power, P_{th}, for a fibre of length L and loss coefficient α can be written as [54]

$$P_{\mathrm{th}} = \frac{\mathcal{Q}}{\gamma\, L_{\mathrm{eff}}}, \qquad L_{\mathrm{eff}} = \frac{1 - \exp(-\alpha L)}{\alpha}. \tag{2.24}$$

Here L_{eff} is the effective interaction length that accounts for exponential attenuation of both the pump and the backward-propagating Stokes wave. The parameter γ is a lumped SBS efficiency parameter that incorporates the Brillouin gain coefficient, effective mode area, and polarisation averaging, following the formulation in [54]. The factor $\mathcal{Q}$ (denoted q in [54]) accounts for the noise-initiated nature of SBS and for the reduction of the effective Brillouin gain due to finite pump linewidth and is typically $20 - 25$ for narrow-linewidth continuous-wave sources.

For a fibre attenuation of $\alpha_{\mathrm{dB}} = 0.2\,\mathrm{dB/km}$, corresponding to the standard C-band loss coefficient, and $L = 20\,\mathrm{km}$, the effective length is $L_{\mathrm{eff}} \approx 13\,\mathrm{km}$. Using representative single-mode fibre parameters with a narrow-linewidth source, the expression above gives an SBS threshold of about $8\,\mathrm{dBm}$ (see Figure 2.16).

Launch powers above this level lead to a rapid increase in Stokes backscatter and a corresponding degradation of the received signal. For reference, the dashed curves in the figure indicate representative SBS threshold values obtained from the exact noise-initiated theory reported in [54]. These curves are included for qualitative comparison only and illustrate the expected threshold behaviour predicted by the full theory, in which the SBS threshold is defined by equating the total backward-propagating Stokes power at the fibre input to a fixed fraction of the launched pump power. No independent numerical evaluation of the full integral expression is performed here. Although the accuracy of the analytical approximation decreases with increasing fibre length and/or fibre loss (i.e., the product αL), it remains sufficiently accurate for lengths below 20 km, which is the target reach in PON systems.

Band dependence is modest but relevant. In the C-band the intrinsic fibre loss is lower, which increases L_{eff} and slightly reduces P_{th} compared with the O-band; the Brillouin gain is also marginally higher at longer wavelengths. In practice, this means the allowed per-channel launch power is usually lower in the C-band for the same route.

However, the SBS threshold is higher for modulated signals. This is because modulation (phase or intensity) broadens the optical spectrum, distributing the optical power over a frequency range wider than the narrow Brillouin gain bandwidth. The Brillouin gain bandwidth itself is determined by the finite acoustic phonon lifetime in the fibre, which arises from damping of the acoustically induced density wave and leads to a Lorentzian gain spectrum with a bandwidth inversely proportional to the phonon lifetime [55]. When the optical spectrum becomes broader than this resonance, only the portion of the optical power that lies within the Brillouin gain bandwidth can efficiently drive and amplify the acoustic wave. As a result, the effective Brillouin gain is reduced and a higher total optical power is required to reach the SBS threshold [55], [56].

Chromatic dispersion

Chromatic dispersion (CD) is the wavelength dependence of group delay in an optical fibre. It is described by the dispersion parameter $D(\lambda)$, expressed in units of ps/(nm·km). Over a fibre span of length L, the accumulated dispersion is

$$D_{\mathrm{tot}} = D(\lambda)L. \tag{2.25}$$

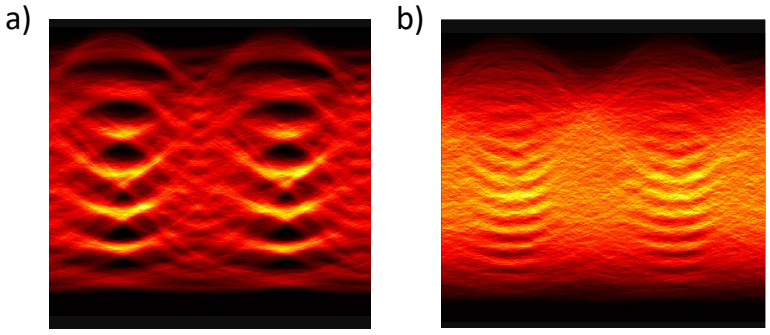


Figure 2.17: Eye diagrams from simulation of 50 Gbaud transmission over 5 km (dispersion $D \approx 17\ \mathrm{ps}/(\mathrm{nm}\cdot\mathrm{km})$): (a) PAM4 and (b) PAM8.

In standard single-mode fibre, chromatic dispersion is small in the O-band around 1310 nm (O-band) ($\approx 0 \pm 3$ ps/(nm·km)) and increases to approximately $16 - 18$ ps/(nm·km) near 1550 nm (C-band) [57]. Thus, for $L = 20$ km, this corresponds to small dispersion in the O-band and $D_{\mathrm{tot}} \approx 320 - 360$ ps/nm in the C-band.

In the simulations, this physical dispersion effect is modelled using a linear baseband-equivalent fibre channel. Chromatic dispersion is represented by a frequency-domain transfer function that imposes a deterministic, frequency-dependent phase shift on the complex optical field,

$$H_{\mathrm{CD}}(f) = \exp\Big(-j2\pi^2\beta_2 L f^2\Big), \tag{2.26}$$

where β_2 is the group-velocity dispersion parameter and f denotes the baseband frequency relative to the optical carrier. The parameter β_2 is directly related to the dispersion coefficient $D(\lambda)$ at the operating wavelength through

$$\beta_2 = -\frac{\lambda^2}{2\pi c} D(\lambda). \tag{2.27}$$

By directly linking the wavelength-dependent dispersion $D(\lambda)$ to the applied phase distortion, this formulation enables accurate modelling of dispersion-induced pulse spreading and constellation distortion, while assuming negligible nonlinear effects and attenuation, which is valid for short-reach PON links.

Future PON solutions target a maximum CD tolerance of 77 ps/nm, which corresponds to about 4.5–5 km of C-band SMF when $D \approx 17$ ps/(nm·km). We use this equivalence in the thesis: a ~ 5 km C-band case reproduces the same dispersion stress level used to verify the proposed IM/DD solution. Figure 2.17 shows eye diagrams from simulations of 50 Gbaud PAM4 and PAM8 signals transmitted over

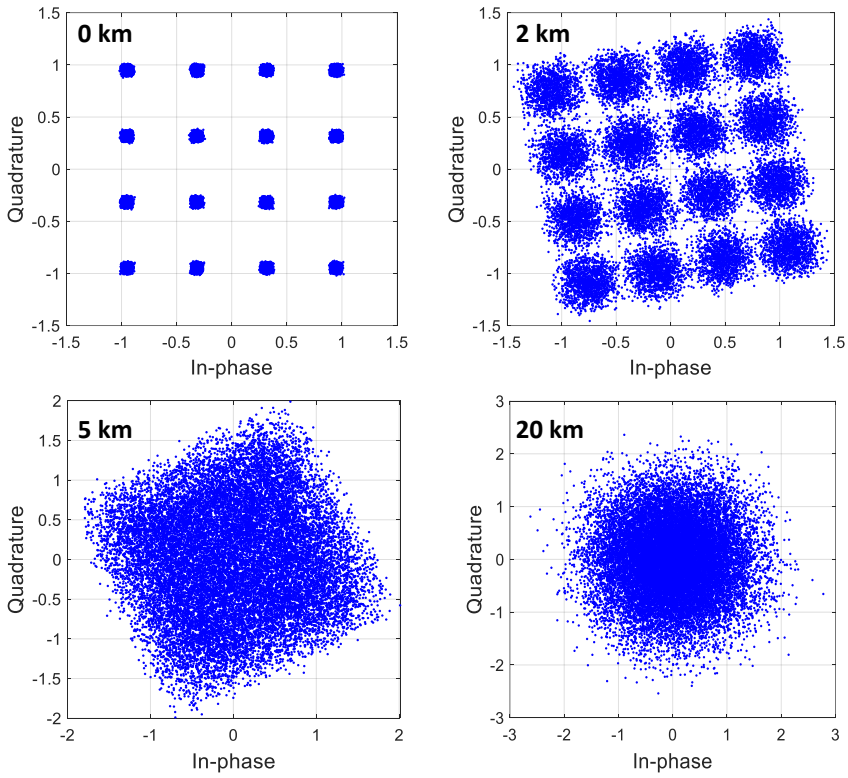


Figure 2.18: Simulated constellations for 50 Gbaud 16QAM using the coherent transmission setup in Figure 2.11.(b), for different lengths of C-band SMF.

5 km of C-band fibre. In IM/DD links with amplitude modulation, CD when combined with square-law detection, results in frequency-selective fading and ISI. As expected, the degradation is more pronounced for the higher-order modulation format (PAM8) due to its reduced symbol spacing and increased sensitivity to ISI. The 50G-PON baseline specifies a 13-tap FFE to mitigate the residual ISI from CD within the operating bandwidth.

Figure 2.18 shows the increasing CD impact on a simulated 50 Gbaud 16QAM coherent PON system. The transmitter and receiver employ root raised cosine (RRC) filters with a roll-off factor of 0.15 to maintain high spectral efficiency by limiting excess bandwidth. Their cascade forms an overall raised cosine response, ensuring zero ISI under ideal conditions. In coherent optical transmission, CD introduces a frequency-dependent phase shift across the signal bandwidth, causing different spectral components of each symbol to accumulate different delays. In the time domain, this results in pulse spreading and inter-symbol interference, while in the complex plane it appears as a systematic distortion and apparent rotation of the received constellation as seen in the figure. Although the dispersion-induced impairment becomes significant over a 20 km C-band fibre

span, it can be effectively compensated by the chromatic dispersion equalisation stage of the coherent receiver DSP, as discussed in Subsection 2.3.2.

2.2.5 Optical Amplification

In PON systems, demanding technical requirements are usually assigned to the OLT since its cost is shared among subscribers, while ONU costs scale with deployment volume. As data rates approach 100 Gb/s and beyond, the OLT receiver must achieve higher sensitivity to constrain ONU launch power. ITU discussions suggest that such sensitivity may require an optically preamplified OLT receiver unless APD technology improves significantly [11]. To meet the higher 29 dB power budget in future PONs, SOAs have therefore been proposed as preamplifiers at the OLT.

Although coherent PON can achieve high receiver sensitivity without relying on a preamplifier to meet the power budget, it still encounters limitations that can be effectively mitigated through optical amplification. One of the key challenges in coherent PON systems is maintaining precise wavelength alignment between the LO and the ONU transmit signal [58]. Low-cost transmitters are prone to wavelength drift by a few nanometers due to fabrication tolerances and temperature variations [59], typically requiring a fast-tunable LO. An alternative uses a frequency comb at the OLT [60], [61], providing multiple narrow lines that tolerate laser drift within the comb's spectral coverage without active LO tuning. This approach, although cost-effective, distributes the total power of the comb across many spectral lines, resulting in low power LO tones. To maintain receiver sensitivity when using N_{comb} comb lines, compared to the case with a single line, the input-referred noise of the TIAs should be reduced by a factor of N_{comb} [62]. However, implementing a low noise TIA is challenging due to the fundamental noise bandwidth trade-off [63]. Consequently, optical preamplification becomes essential to ensure the received signal is strong enough given the relatively low-power LO. SOAs are well-suited for this role, offering low cost, compact size, and scalability, making them ideal for integration with coherent receivers.

Low Power Regime: Amplified Spontaneous Emission

SOAs inevitably add noise because the same population inversion that provides gain also drives spontaneous emission. In an inverted semiconductor medium, the spontaneous emission rate is set by the carrier population (i.e., it depends on the carrier density/inversion), so it cannot be eliminated while the device is

biased for gain. In an SOA, this noise is emitted across the gain spectrum and, when captured by the guided mode, is amplified along the device. The resulting ASE is therefore an inherent consequence of operating the SOA with inversion and is typically the dominant noise mechanism [53].

The single-polarisation ASE spectral density at the output is $S_{\mathrm{ASE}} = \chi\, n_{\mathrm{sp}}(G-1)h\nu$, where $n_{\mathrm{sp}} \geq 1$ is the spontaneous–emission factor, G is intensity gain, h is Plank's constant, and ν is the optical carrier frequency. $\chi \geq 1$ captures excess noise from input coupling loss, residual facet reflections, and internal waveguide loss. With an optical reference bandwidth $\Delta\nu_{\mathrm{ref}}$ (e.g., $12.5\,\mathrm{GHz}$ for $0.1\,\mathrm{nm}$ near $1550\,\mathrm{nm}$), the output optical signal-to-noise ratio (OSNR) of an unsaturated SOA is

$$\mathrm{OSNR} = \frac{P_{\mathrm{sig,out}}}{P_{\mathrm{ASE}}(\Delta\nu_{\mathrm{ref}})} = \frac{G\,P_{\mathrm{in}}}{S_{\mathrm{ASE}}\,\Delta\nu_{\mathrm{ref}}} = \frac{G\,P_{\mathrm{in}}}{\chi\, n_{\mathrm{sp}}(G-1)h\nu\,\Delta\nu_{\mathrm{ref}}}. \tag{2.28}$$

In IM/DD square–law detection produces signal–spontaneous beat noise and spontaneous–spontaneous beat noise inside the electrical bandwidth B. For sufficiently high OSNR and when the optical noise bandwidth $\Delta\nu$, is much larger than electrical bandwidth, the signal–spontaneous beat noise dominates, yielding the approximate mapping [53]

$$\mathrm{SNR} \;\approx\; \frac{\mathrm{OSNR}\cdot\Delta\nu_{\mathrm{ref}}}{2\,B}. \tag{2.29}$$

While the spontaneous–spontaneous beat noise increases linearly with $\Delta\nu$, its contribution remains secondary in this regime. At lower OSNR or for excessively wide optical filtering, spontaneous–spontaneous beat noise becomes significant and the simple OSNR–SNR correspondence no longer applies. In practice, the effective SNR also depends on the modulation format, as schemes such as PAM4 exhibit additional penalties compared to NRZ.

In an optically preamplified coherent receiver, the dominant noise contributions are shot noise introduced by the LO and signal-ASE beat noise generated by the optical amplifier. For practical amplifier noise figures and sufficiently high optical gain ($G \gg 1$), the signal-ASE beat noise is usually much higher than the shot noise and the signal–ASE beat noise dominates over LO shot noise. When the optical filtering bandwidth is sufficiently narrow, the ASE–ASE beat noise can be neglected. Under these assumptions, the electrical SNR can be expressed as

$$\mathrm{SNR} = \frac{R^2 P_{\mathrm{LO}} P_{\mathrm{r}}}{2R^2((P_{\mathrm{LO}}+P_{\mathrm{r}})/2)S_{\mathrm{ASE}}B} \;\approx\; \frac{\mathrm{OSNR}\cdot\Delta\nu_{\mathrm{ref}}}{B}, \tag{2.30}$$

where $P_{\mathrm{LO}} \gg P_{\mathrm{r}}$. This indicates that coherent detection receiver in an optically amplified system improves the required OSNR by 3 dB compared to direct detection.

High-Power Regime: Gain Compression and Nonlinear Distortion

In an IM/DD transmission system, the SOA provides optical gain to meet the 29 dB power budget. However, its amplification capability is fundamentally limited by gain saturation at high input power levels. When the input power, P_{in}, becomes comparable to the SOA's saturation power, P_{sat}, the carrier density in the active region is depleted by stimulated recombination faster than it can be replenished by electrical injection. This carrier depletion lowers the population inversion (and hence the material gain), causing the optical gain $G = P_{\mathrm{out}}/P_{\mathrm{in}}$ to decrease as the input power increases. The static gain–power relationship can be described by

$$\frac{P_{\mathrm{in}}}{P_{\mathrm{sat}}} = \frac{\ln(G_0/G)}{G-1}, \tag{2.31}$$

where G_0 is the small-signal gain. While the gain remains approximately constant in the linear region ($P_{\mathrm{in}} \ll P_{\mathrm{sat}}$), it compresses significantly as P_{in} approaches P_{sat}, marking the onset of nonlinear behaviour.

In IM/DD systems, the modulated optical power varies with time, and thus the SOA gain becomes time dependent [53], [64]:

$$G(t) = \frac{G_0}{G_0 - (G_0 - 1)\exp\left(-E(t)/E_{\mathrm{s}}\right)}, \qquad E(t) = \int_{-\infty}^{t} P_{\mathrm{in}}(t')\,dt', \tag{2.32}$$

where $E(t)$ is the accumulated input energy and E_{s} is the saturation energy. For high-power symbols, $E(t)$ increases rapidly, leading to progressive gain reduction within a single pulse. As shown in Figure 2.19, the leading edge of a PAM4 symbol is amplified more strongly than its trailing edge, producing a slanted waveform rather than a flat-top pulse.

The saturation input power, $P_{\mathrm{in,sat}}$, at which the SOA gain decreases by 3 dB, marks the practical threshold for this transition. Inputs exceeding $P_{\mathrm{in,sat}}$ push the SOA into its nonlinear, gain-saturated regime. However, for PAM4 modulation, BER typically begins to degrade well below this threshold due to its reduced SNR and tighter spacing between voltage levels compared to NRZ modulation.

In coherent transmission systems, symbol transitions are affected by the nonlinear complex response of the SOA, leading to both amplitude distortion and

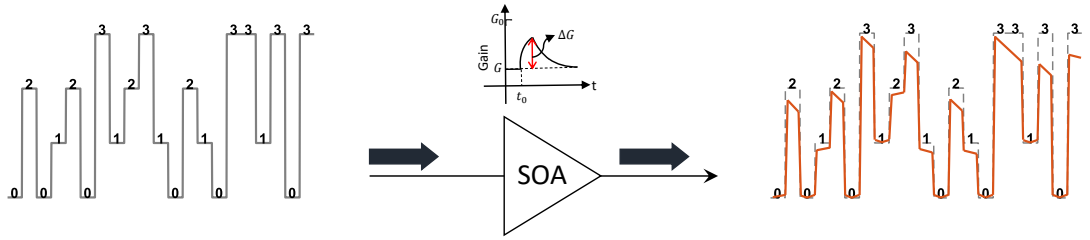


Figure 2.19: SOA gain compression effect on a PAM4 pulse

phase shifts, whose impact on the amplified signal depends on the modulation format. Near saturation, carrier-density variations modulate the optical gain and also change the refractive index, resulting in an additional gain-dependent phase shift. This amplitude–phase conversion is described by effective α_{eff} factor, which links gain changes to phase changes

$$\Delta\phi \approx -\frac{\alpha_{\text{eff}}}{2}\Delta(\ln G), \tag{2.33}$$

so that gain modulation translates into phase modulation [65]. As a result, both the amplitude and phase fidelity of the amplified signal degrade when the SOA operates close to saturation. The extent of this degradation depends on the modulation format and on the value of the α_{eff} factor.

The effect can be illustrated using a binary phase-shift keying (BPSK) signal, as shown in Figure 2.20. In this format, the optical field alternates between two antipodal points on the in-phase axis. During a zero-crossing transition, the optical field passes through zero intensity as it moves from one constellation point to the other. This transition induces a strong temporal variation in the optical power incident on the SOA, which leads to a transient depletion of carriers and a reduction in the optical gain. Due to the coupling between gain and refractive index, this change in carrier density produces a transient phase shift. In many bulk and quantum-well SOAs, the phase shift does not recover immediately because the refractive-index recovery is often governed by slower carrier population dynamics than the gain recovery [66], [67], [68]. Consequently, residual phase errors persist into the following symbol period, distorting the transmitted information. At the output, these effects appear as arc-like spreading of the constellation points around their ideal positions, as illustrated on the right side of the figure.

Compared to BPSK, QPSK and 16QAM experience reduced average saturation-induced phase distortion in an SOA. In an ideal QPSK, the constant envelope constellation results in minimal symbol-to-symbol optical power variations, so

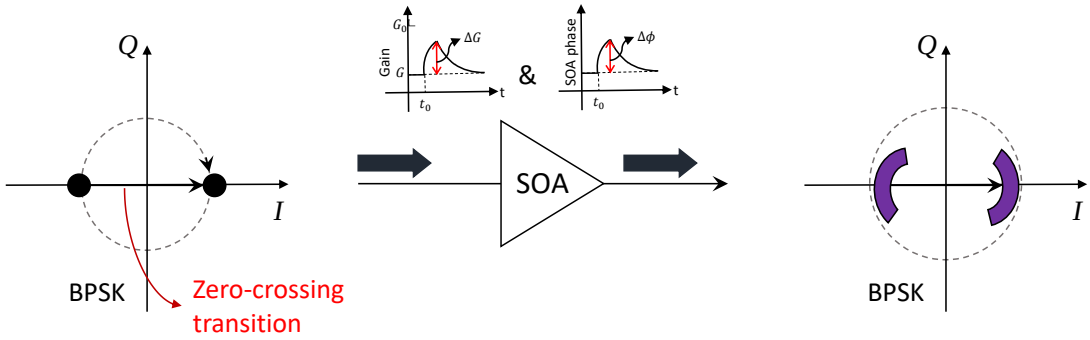


Figure 2.20: Schematic illustration of SOA saturation effects for a BPSK signal.

carrier-density fluctuations and associated phase distortions are less pronounced. In 16QAM, both amplitude and phase are modulated, and the constellation contains multiple amplitude levels. Although extreme transitions between the largest and smallest power levels occur infrequently, the presence of amplitude modulation leads to symbol-to-symbol power variations. As a result, patterning effects occur in the gain-saturated regime, causing both amplitude compression and power-dependent phase shifts through amplitude–phase coupling. These effects reduce the distance between constellation points and limit the achievable signal quality.

2.3 Equalisation and Signal Post Processing

In high-speed PONs, receiver equalisation is needed to mitigate bandwidth limits, ISI, and device nonlinearities. The FFE, introduced in the latest 50G-PON standard, is the conventional approach in IM/DD receivers, but its ability to cope with higher-order modulation and SOA/TIA-induced nonlinearities is limited. Recently, machine learning (ML)-based equalisers have been investigated to overcome these limits, including by our own group. In coherent receivers, DSP blocks already provide dispersion compensation, carrier recovery, and advanced equalisation, though at higher complexity and cost. This section compares conventional FFE and ML-based approaches in IM/DD and reviews coherent DSP blocks, highlighting their effectiveness and trade-offs for future PONs.

2.3.1 IM/DD

In IM/DD receivers, conventional equalisers such as the FFE are often sufficient to mitigate linear impairments and residual ISI. However, the introduction of higher-order modulation formats (e.g., PAM4, PAM8) in next-generation PONs,

combined with device-induced nonlinearities such as SOA gain saturation or burst-mode TIA distortion, poses challenges that exceed the capabilities of linear equalisers. To address these limitations, ML-based equalisers, such as neural networks and recurrent architectures, are being investigated to capture and correct nonlinear effects more effectively.

Standard DSP: FFE

The FFE is one of the most widely adopted digital equalisation techniques in IM/DD PON receivers. In addition to mitigating ISI caused by the limited bandwidth of optical and electrical components, the FFE is commonly employed to compensate for the residual effects of CD in short- to medium-reach PON links.

In IM/DD systems, chromatic dispersion leads to temporal pulse broadening and distortion after square-law photodetection. Although the resulting electrical channel is not strictly linear, for moderate accumulated dispersion the dominant impairment manifests as ISI with finite memory. In this regime, a linear FFE equaliser can effectively mitigate dispersion-induced distortions.

The FFE operates by forming a weighted sum of time-shifted replicas of the received signal samples. By appropriately adapting the tap coefficients, the equaliser reduces the contribution of neighbouring symbols to the current symbol decision, thereby improving receiver performance in the presence of bandwidth limitations and dispersion-induced ISI.

For an FFE with N taps, the equalised output is given by

$$y[k] = \sum_{i=1}^{N} w_i \, r[k-i] \tag{2.34}$$

where $r[k]$ is the received signal sample at time k, w_i are the adaptive filter coefficients. The tap coefficients are adapted to minimise an error criterion, most commonly the mean squared error (MSE) between the equaliser output and a reference symbol sequence. In practical PON receivers, adaptation is commonly performed using the least mean square (LMS) algorithm during an initial training phase or in a decision-directed mode. The LMS update rule is expressed as

$$w_i^{(k+1)} = w_i^{(k)} + \mu \, e[k] \, r[k-i] \tag{2.35}$$

where $e[k] = d[k] - y[k]$ is the error between the desired symbol $d[k]$ and the

equaliser output, and μ is the adaptation step size.

In access network IM/DD PON systems, where the fibre reach is typically limited to around 20 km and the accumulated chromatic dispersion is therefore moderate, the FFE is effective in mitigating dispersion-induced distortions. However, it is inherently limited in its ability to compensate nonlinear distortions such as SOA gain saturation. Nevertheless, owing to its low computational complexity, deterministic latency, and hardware-friendly implementation, the FFE remains a practical and widely adopted baseline equalisation technique in high-speed PON receivers, including 50G-PON.

ML-Based equalisation

ML-based equalisers have been proposed to overcome the fundamental limitations of linear filtering in PON receivers. Unlike the FFE, which struggles with nonlinear impairments, neural network equalisers can model complex nonlinear transfer functions and adapt to diverse packet conditions. The following discussion briefly reviews ML-based equalisation techniques developed within our group to compensate for SOA-induced nonlinearity. My contribution to these works mainly involved the implementation of the experimental setup and the execution of the data acquisition that supported the development and validation of the proposed algorithms. A detailed analysis of these approaches is intentionally out of scope for this thesis. The ML-based results are therefore summarised at a high level to provide an overview of the complex algorithms required to compensate for SOA nonlinearities. In this thesis, the focus is placed on modifying the SOA dynamics to mitigate nonlinear effects at the optical level, which reduces the reliance on complex DSP.

In [A3], [A4], we investigated recurrent neural network (RNN) equalisers based on gated recurrent units (GRUs). A GRU incorporates a feedback mechanism that processes current inputs together with information from previous states, effectively capturing long memory effects such as SOA patterning. Figure 2.21.(a) illustrates the GRU unit, where gating functions regulate how much past information is retained or updated. This structure allows accurate equalisation using only three input taps, compared to the tens of taps required by more traditional fully connected neural networks (FC-NNEs). Experimentally, GRU-RNN equalisation enabled more than 28 dB dynamic range in a 100 Gb/s PAM4 PON link, exceeding the 20.5 dB requirement of ITU-T 50G-PON, while also compensating for bandwidth limitations and fibre dispersion up to 91.8 ps/nm.

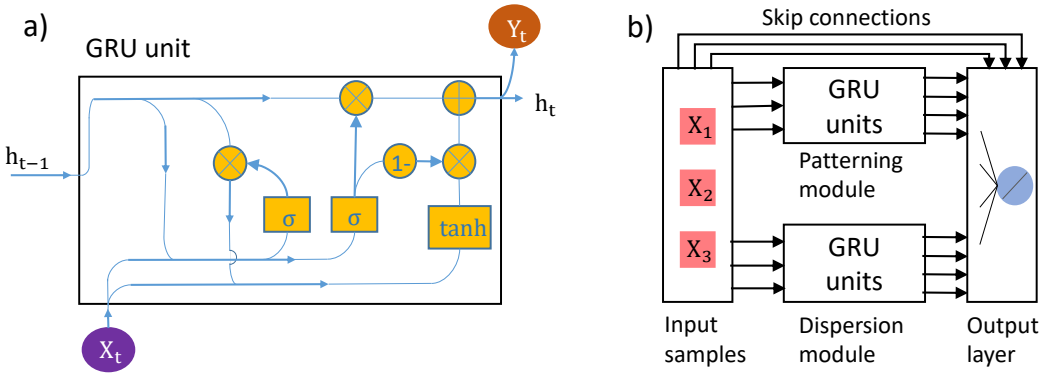


Figure 2.21: (a) Schematic of a GRU unit, and (b) the concept of combining modular GRUs for addressing multiple impairments is shown, where each ”module” is exposed to a single isolated impairment during training.

More recently, we proposed a modular NNE with skip connections for burst-mode adaptation [A5]. The skip connection allows raw input samples to bypass nonlinear hidden layers and combine with their outputs at a trainable linear node (Figure 2.21.(b)). This design enables rapid adaptation using a simple LMS algorithm applied only to the output layer, while the nonlinear layers remain fixed after offline training. As a result, convergence is achieved within 2000 symbols (40 ns at 50 Gbaud). Moreover, by training modular networks on isolated impairments such as SOA patterning or chromatic dispersion, and then combining them, the equaliser can effectively handle multiple simultaneous impairments in a flexible and scalable manner.

In follow-up work [A6], we further demonstrated the practicality of skip-connection architectures by implementing a feed-forward neural network (FFNN) with skip connections on Field Programmable Gate Array (FPGA) hardware. In a back-to-back 100 Gb/s PAM4 scenario, this equaliser achieved robust convergence within the required packet preamble length while maintaining manageable computational cost. This study confirms that neural networks with skip connections can be made hardware-feasible, though they still require careful architectural design to balance performance and resource efficiency.

Across these studies, ML-based equalisers have shown superior capability to extend system dynamic range and mitigate nonlinear impairments compared to FFE. GRU-RNNs provide compact nonlinear modelling, while skip-connection architectures enable fast burst-by-burst adaptation and even practical FPGA implementation. However, these approaches remain computationally complex and still depend on high-performance burst-mode TIAs with large dynamic range, high gain, and wide bandwidth. When a TIA operates in saturation or clipping,

different input signals can produce the same output waveform. This causes a loss of information that cannot be recovered after detection. Neural-network-based equalisers work on the digitised signal and therefore only have access to this distorted output. As a result, they cannot fully compensate for TIA nonlinearities.

These limitations highlight the need for complementary approaches to address a large upstream dynamic range in PON. In particular, SOA-based optical power equalisation, investigated in Section 2.4, offers a promising solution by performing equalisation in the optical domain before electrical detection. This shifts the burden away from the TIA and DSP, enabling simpler, lower-cost receiver design while still supporting the demanding requirements of future high-speed PON systems.

2.3.2 Coherent PON DSP Blocks

Unlike IM/DD systems, which typically rely on simple FFE that can only partially mitigate linear impairments, coherent detection systems employ advanced DSP techniques capable of fully compensating for such effects. In particular, coherent DSP enables effective mitigation of impairments originating from the transmitter, optical channel, and receiver within the electrical domain. A typical coherent DSP chain consists of several functional blocks, including I/Q imbalance compensation, chromatic dispersion compensation, frequency offset estimation, and carrier phase recovery. The following section provides an overview of the functionality of each block and discusses the corresponding compensation algorithms in detail.

I/Q Imbalance Compensation

In a coherent optical receiver, the in-phase (I) and quadrature (Q) components of the signal are ideally orthogonal, separated by exactly 90° in phase and equal in amplitude. In practice, imperfections in the optical hybrid, balanced photodiodes, and transimpedance amplifiers introduce amplitude and phase mismatches between the I and Q channels. These mismatches, often caused by path-length differences or component tolerances, destroy the orthogonality of the received signals. As a result, the constellation points that should ideally form a square lattice become skewed or compressed along one axis, producing an elliptical distortion of the constellation.

To correct this non-orthogonality, coherent receivers commonly use a

Gram–Schmidt orthogonalisation procedure (GSOP) within the digital signal processing chain. Assuming zero-mean, stationary I and Q components and a linear I/Q imbalance, GSOP removes the second-order correlation between the channel and normalises their power. The orthogonalised signals are given by

$$I' = \frac{I}{\sqrt{\langle I^2 \rangle}}, \quad Q' = \frac{Q - \frac{\langle IQ \rangle}{\langle I^2 \rangle} I}{\sqrt{\langle Q^2 \rangle - \frac{\langle IQ \rangle^2}{\langle I^2 \rangle}}}, \tag{2.36}$$

where $\langle . \rangle$ denotes statistical expectation. This transformation ensures that the resulting I' and Q' components are orthonormal in a second-order statistical sense. The constellation thus changes from an elliptical distribution back to a circularly symmetric one, restoring proper signal geometry. As demonstrated in [69], GSOP-based I/Q imbalance compensation significantly reduces the OSNR penalty and improves frequency estimation accuracy, while maintaining low computational complexity, making it well-suited for practical coherent receivers.

Chromatic Dispersion Compensation

In theory, CD can be completely compensated using a static digital filter, as the dispersion in the fibre is a deterministic linear time-invariant effect under the second-order dispersion approximation. The compensating filter is designed as the inverse of the baseband chromatic dispersion transfer function (see Equation 2.26), which can be implemented either in time domain or in the frequency domain. By applying this filter, the quadratic phase distortion accumulated over transmission, dominated by second-order dispersion, is effectively cancelled.

In the time domain, this operation corresponds to convolving the received signal with the impulse response of the inverse dispersion filter. Although the exact impulse response is theoretically of infinite duration, it can be approximated as a finite impulse response (FIR) filter. The FIR filter coefficients represent a truncated, discretised approximation of the ideal inverse impulse response, with the required number of taps depending on the symbol rate and the total accumulated dispersion. While perfect cancellation is not achievable due to truncation, parameter mismatch, higher-order dispersion, and system bandwidth limitations, a sufficiently long filter provides accurate CD compensation in practical systems.

This **static equalisation** approach is highly effective for channels where dispersion does not vary over time, which is true for most fibre links. Once the total link

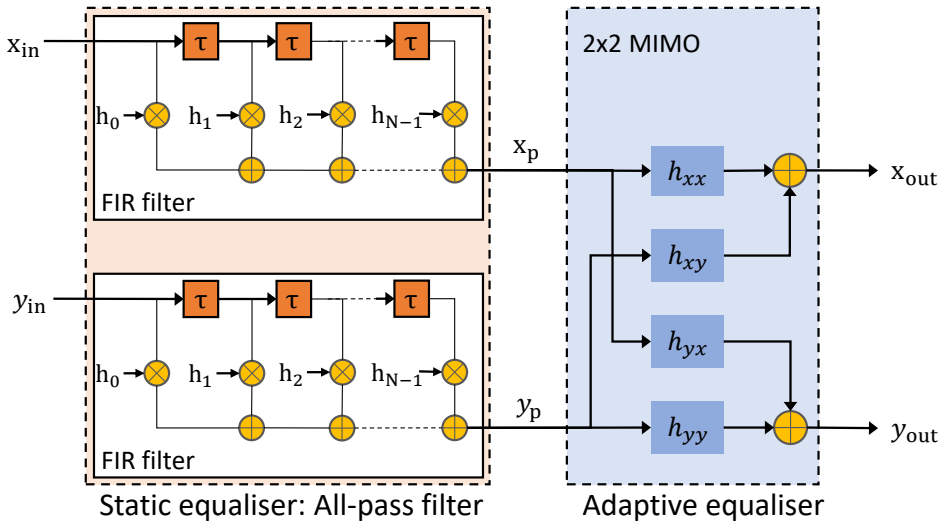


Figure 2.22: Functionality of the digital filtering stage. For linear filtering, the order of the two sub-blocks may of course be reversed.

dispersion is known, the filter can be preconfigured and applied digitally, removing the need for bulky dispersion-compensating fibres and simplifying system design.

While static filters effectively mitigate bulk CD, coherent receivers also employ **adaptive equalisers** to handle time-varying effects such as polarisation rotation and polarisation mode dispersion (PMD). These adaptive filters, typically implemented as 2×2 multi-input multi-output (MIMO) FIR filters, can simultaneously track polarisation changes and residual linear impairments, including any uncompensated or slowly varying CD components.

Although the adaptive equaliser's primary role is compensation for polarisation-dependent effects, it can provide fine-tuning for CD compensation, especially in links where dispersion varies slightly due to temperature or wavelength drift. In coherent DSP implementations, a hybrid approach is often adopted: a static CD equaliser provides bulk dispersion compensation, followed by an adaptive equaliser that refines the signal quality and compensates for residual distortions. Consequently, coherent digital signal processing commonly adopts a hybrid approach, in which a static CD equaliser provides bulk dispersion compensation, followed by an adaptive equaliser that refines signal quality and compensates residual linear distortions. Therefore, the linear digital filtering can be implemented using the architecture shown in Figure 2.22, with adaptive equalisation continuously updating the FIR tap weights.

Frequency Offset Cancellation

In intradyne coherent detection, the transmit and LO lasers are free-running and not frequency-locked. Consequently, a residual carrier frequency offset (CFO) remains within the receiver bandwidth, manifesting as a deterministic rotation of the received signal constellation in the complex plane. If uncompensated, this rotation degrades the performance of carrier phase recovery (CPR) algorithms and leads to increased bit-error rates.

A common and efficient method is the feed-forward phase increment approach originally proposed for optical intradyne receivers in [70]. The algorithm exploits the fact that a constant frequency offset produces a constant phase increment between consecutive symbols. Let $u_{\text{in}}(n)$ denote the complex baseband signal sampled at the symbol period T_{s}. The phase increment is obtained by multiplying the signal with the complex conjugate of a one-symbol-delayed version, $u_{\text{in}}(n)u_{\text{in}}^{*}(n-1)$.

For QPSK modulation formats, the data-dependent phase can be removed by raising this product to the fourth power. Averaging the resulting samples over an observation window of length L yields the estimated frequency offset

$$\Delta\nu_{\text{offset}} = \frac{1}{4} \times \frac{1}{2\pi T_{\text{s}}} \arg\{\frac{1}{L}\sum_{n=1}^{L}[u_{\text{in}}(n)u_{\text{in}}^{*}(n-1)]^{4}\}. \tag{2.37}$$

This digital correction effectively stops the constellation rotation and allows accurate carrier phase estimation. In practice, it enables receivers to tolerate several-gigahertz laser frequency differences.

For 16QAM modulation, the fourth power phase-increment method commonly used for QPSK cannot be directly applied to the full constellation, since 16QAM symbols are not constant modulus and the data-dependent phase cannot be fully removed by a fixed power operation. However, frequency offset estimation can still be achieved by exploiting the inherent phase structure of the 16QAM constellation. In particular, the constellation can be partitioned into symbol subsets that share identical phase values and therefore form QPSK-like constellations with different amplitudes.

Carrier Phase Recovery

Laser phase noise causes random carrier phase rotations that must be accurately tracked and compensated in coherent receivers. Blind approaches such as the

blind phase search (BPS), are capable of estimating these impairments but typically incur high computational complexity and slow convergence. Pilot-aided techniques provide a simpler and faster alternative and are therefore particularly attractive for burst-mode coherent PONs, where frequent burst arrivals and short time slots require deterministic and rapid convergence of the DSP chain [71].

In pilot-aided schemes, known pilot symbols are periodically embedded within the data stream to provide reference points for phase estimation. The carrier phase at each pilot position can be obtained as

$$\psi_{\text{pilot}}(j) = \arg\left(t^*(j)\, p(j)\right), \tag{2.38}$$

where $t(j)$ denotes the transmitted pilot symbol and $p(j)$ is the corresponding equalised received symbol. Between pilot positions, the residual phase noise is refined using a maximum-likelihood estimator that exploits the short-term temporal correlation of the phase noise process,

$$\psi_{\text{ML}}(i) = \frac{1}{2Q+1} \sum_{l=i-Q}^{i+Q} \arg\left(q(l)\, \hat{q}^*(l)\right), \tag{2.39}$$

where $q(l)$ is the pilot-compensated symbol and $\hat{q}(l)$ denotes its detected decision. This hybrid pilot/maximum-likelihood scheme enables robust phase tracking with minimal overhead, making it suitable for future coherent PONs.

2.4 SOA-Based Power equalisation Methods

In this section, we introduce two SOA-based power equalisation techniques developed in this work, referred to as (A) variable bias and (B) control light injection. These methods are designed to equalise packet power levels directly in the optical domain, thereby improving signal uniformity before detection. In addition to power equalisation, both techniques are observed to mitigate the nonlinear patterning effects in the SOA by preventing gain saturation.

Numerical simulations are performed in MATLAB using a steady-state SOA model originally proposed in [72]. The model parameters, L_c, L_t, d, W, Γ, K_0, A_{rad}, A_{nrad}, B_{nrad}, and C_{aug}, are adjusted to match the characteristics of the SOA used in the experimental investigations presented in the remainder of this thesis, while all remaining parameters are taken directly from [72]. The simulations are employed to evaluate Method A by analysing the effect of bias current reduction

on the SOA gain, noise figure (NF), and saturation input power. In addition, wavelength-dependent gain simulations are used to provide insight into Method B. The simulation parameters are summarised in Table 2.1.

Table 2.1: SOA simulation parameters

Symbol	Parameter	Value
y	Molar fraction of Arsenide in the active region	0.892
L_c	Central active region length	$210\ \mu$m
L_t	Tapered active region length	$0\ \mu$m
d	Active region thickness	80×10^{-9} m
W	Central active region width	2.5×10^{-6} m
Γ	Optical confinement factor	0.33
K_g	Bandgap shrinkage coefficient	0.9×10^{-10} eV m
n_1	InGaAsP active region refractive index	3.22
n_2	InP region refractive index	3.167
η_{in}	Input coupling loss	3 dB
η_{out}	Output coupling loss	3 dB
R_1	Input facet reflectivity	5×10^{-5}
R_2	Output facet reflectivity	5×10^{-5}
K_0	Carrier independent absorption loss coefficient	4200 m^{-1}
K_1	Carrier dependent absorption loss coefficient	7500 m^{-2}
A_{rad}	Linear radiative recombination coefficient	1.43×10^{8} s^{-1}
B_{rad}	Bimolecular radiative recombination coefficient	5.6×10^{-16} m^{3}s^{-1}
A_{nrad}	Linear nonradiative recombination coefficient due to traps	1×10^{8} s^{-1}
B_{nrad}	Bimolecular nonradiative recombination coefficient	1×10^{-40} m^{3}s^{-1}
C_{aug}	Auger recombination coefficient	4×10^{-40} m^{6}s^{-1}
D_{leak}	Leakage recombination coefficient	0×10^{48} m$^{13.5}$s^{-1}
m_{e}	Effective mass of electron in the CB	4.1×10^{-32} kg
m_{hh}	Effective mass of a heavy hole in the VB	4.19×10^{-31} kg
m_{lh}	Effective mass of a light hole in the VB	5.1×10^{-32} kg

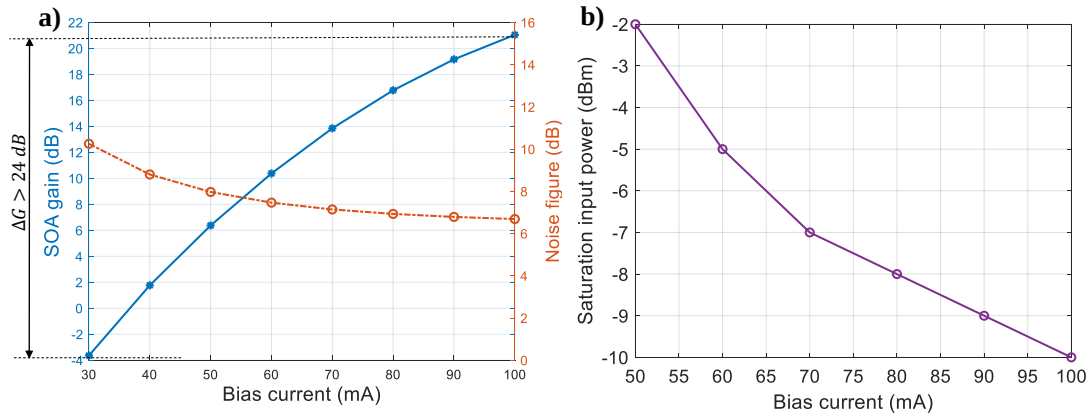


Figure 2.23: Simulation results showing the impact of SOA bias adjustment on (a) gain and noise figure, and (b) saturation input power.

2.4.1 Variable Bias

The variable bias technique equalises burst power by dynamically controlling the gain of the SOA through adjustment of its bias current. In an SOA, optical amplification results from carrier injection into the active region by the bias current, making the amplifier gain strongly dependent on the bias current.

As shown by the simulation results in Figure 2.23.(a), varying the bias current results in significant gain variation, thereby providing a wide dynamic range suitable for burst power equalisation. However, a reduction in bias current is accompanied by an increase in the NF, which is defined as the ratio of the input OSNR to the output OSNR, as illustrated in the figure. This degradation in noise performance may affect signal integrity.

At high input powers, the dominant limiting factor is the patterning effect induced by gain saturation. However, the initial simulation results indicate that reducing the SOA bias current increases the saturation input power (see Figure 2.23.(b)), thereby extending the SOA's linear operating region. This suggests that nonlinear distortion can be mitigated by tailoring the SOA's dynamic response through bias control, even if this comes at the expense of a moderate increase in noise. Overall, these findings show that the variable-bias approach offers a practical trade-off between noise performance and nonlinear distortion suppression, making it a viable solution for achieving the high dynamic range required in future PON systems. The next chapter provides an experimental analysis of this method and discusses its benefits and implementation requirements in more detail.

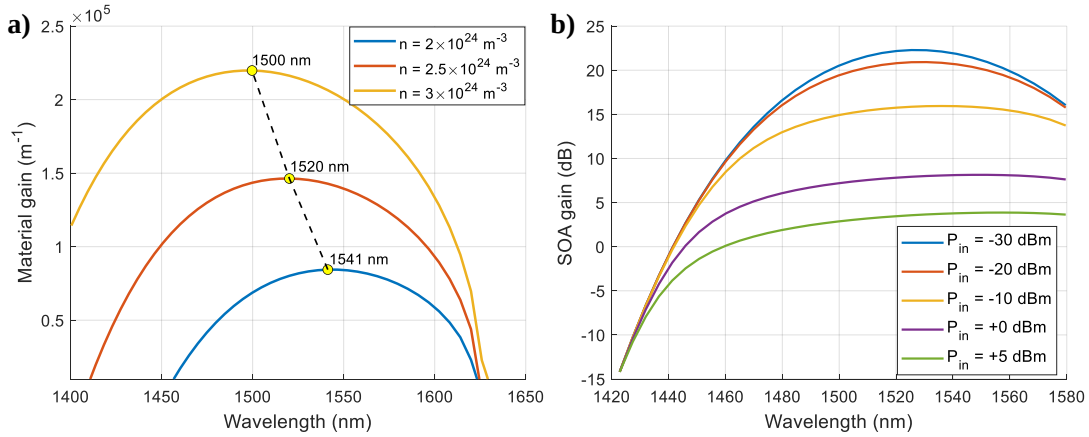


Figure 2.24: Simulation results showing (a) the SOA material gain coefficient spectra at different carrier densities and (b) the SOA gain spectra at different input powers.

2.4.2 Control Light Injection

The idea of control light injection emerges from the carrier-density-dependent gain dynamics of the SOA. The material gain spectrum is simulated using a standard bulk gain formulation based on band-to-band transitions and Fermi's golden rule, in which the gain coefficient is calculated from the three-dimensional joint density of states and Fermi–Dirac carrier occupation probabilities defined by quasi-Fermi levels, with stimulated emission and absorption contributions evaluated separately and combined to obtain the net material gain. This model is widely used for bulk SOA gain simulations and follows the formulations described in [73], [74]. Figure 2.24.(a) shows the simulated gain spectra for different carrier densities. As the carrier density increases, band filling enables optical transitions at higher photon energies, leading to spectral broadening and a blue shift of the gain peak. Under saturated conditions, stimulated emission depletes carriers in higher-energy states, leaving carriers concentrated near the band edge. This results in a narrowing of the gain spectrum and a red shift of the peak gain, as observed in the simulated results. This behaviour suggests that the gain of the SOA can be intentionally modified by introducing an additional optical signal at a wavelength close to the signal wavelength. By doing so, it becomes possible to deliberately increase gain saturation and reduce the available gain. At first, we assume that the control light must be placed very close to the signal wavelength to create strong carrier competition. However, further analysis shows that the relative wavelength separation between the signal and control light must be optimised to obtain efficient gain reduction while avoiding unwanted nonlinear effects.

While developing this concept, a study reported in [75] is identified, where a similar approach of external light injection is employed to control the output power of an SOA for 10 Gb/s NRZ signals. Although that work demonstrates the feasibility of gain control through optical injection, it requires relatively high control-light powers, which limits its practicality for compact or energy-efficient systems.

The simulation in Figure 2.24.(b) illustrates how the SOA gain spectrum evolves with increasing input power and provides the basis for the control-light injection concept. At low power, the gain peaks at the shorter wavelengths of the C-band, but as the input power increases the peak shifts toward longer wavelengths (red shift). Because the control-light power is always higher than the signal power, this peak-gain shift indicates that placing the control light at a longer wavelength induces stronger carrier depletion and therefore a larger gain reduction. Building on these insights, the next chapter presents the experimental investigation and optimisation of the scheme, with the objective of achieving efficient gain control through optimal wavelength selection and reduced control-light power.

2.5 Summary

This chapter establishes the theoretical framework for high-speed PONs and examines the impairments that fundamentally limit their performance. By comparing O-band IM/DD and C-band coherent architectures, it shows that while PAM4 IM/DD offers cost efficiency and implementation simplicity, its performance is strongly constrained by bandwidth limitations, dispersion, and noise accumulation. In contrast, coherent detection provides higher spectral efficiency and improved tolerance to transmission impairments at the expense of increased system complexity.

In practical PON deployments, ONUs experience unequal distribution losses, resulting in burst-to-burst power variations that can exceed 20.5 dB. Conventional receivers struggle to accommodate such a wide dynamic range without sacrificing sensitivity or linearity due to BM-TIA limitations.

A detailed analysis of SOAs demonstrates that, although they provide the required preamplification to meet a stringent 29 dB power budget, their nonlinear gain dynamics introduce significant signal distortions with advanced modulation formats. The gain saturation leads to patterning effects and phase distortions that depend on the modulation format and operating regime. These effects are

particularly detrimental to multilevel IM/DD signals and coherent constellations operating near saturation.

Overall, this chapter outlines the future direction and requirements of next-generation PON systems, examines the key physical-layer impairments, and identifies BM-TIA bandwidth and linearity constraints together with SOA nonlinearities as the primary limiting factors in future high-speed PON receivers. In this context, we introduce two SOA-based power-equalisation techniques: variable bias and control-light injection, and present initial simulation results to assess their feasibility. These results show that, in the variable bias case, the achievable gain adjustment comes at the cost of increased noise, but also increases the saturation input power, thereby extending the SOA's linear operating range. Furthermore, the simulated gain spectrum evolution for the control light injection method indicates that achieving larger gain changes is more effective when the control light is placed at longer wavelengths, due to the red shift of the SOA gain peak at high input powers. These findings reinforce the motivation for optical domain equalisation as a viable pathway to achieving wide dynamic range operation in future PON systems. The following chapter experimentally examines these initial observations and discusses the practical benefits and implementation requirements of both approaches.

Chapter 3

SOA Output Power Control through Dynamic Gain Adjustment

This chapter investigates SOA-based optical power equalisation for high-speed PONs. It begins with an analysis of SOA fundamentals, including its gain mechanism, frequency response, and transient behaviour under burst-mode signals. Two dynamic gain control methods, (A) variable bias current and (B) control light injection, are then examined to maintain constant SOA output power under large input variations. Their performance, drawbacks, and implementation complexity are analysed and optimised in terms of achieving a larger dynamic range.

In PONs, upstream packets can exhibit power variations of up to 20.5 dB due to differential losses between users. Conventional burst-mode TIAs compensate for this by adjusting their gain per packet, but their bandwidth, linearity, and dynamic range limit performance at high speeds.

To meet the 29 dB power budget in PONs, SOAs are employed as preamplifiers at the OLT to enhance receiver sensitivity. Their cost-effectiveness, compactness, and scalability make them ideal for integration with receivers [76], [77], [78], [79]. Leveraging the same SOA for optical power equalisation offers a practical alternative to complex burst-mode receivers, providing higher dynamic range, no bandwidth limitation, and reduced gain saturation distortions.

3.1 SOA for High-Speed PON

SOAs are considered a promising solution for high-speed PONs, serving as optical preamplifiers to enhance receiver sensitivity in IM/DD systems [15], [80]. In coherent detection, they have also gained attention for improving receiver sensitivity without the need to increase LO power, thereby reducing overall power consumption [81], [82]. However, their performance is intrinsically linked to carrier recombination dynamics and nonlinear effects that may induce signal distortions under high optical power conditions. The interplay of these mechanisms defines the amplifier's gain, noise, and dynamic response, thereby constraining its effectiveness in high-speed optical access systems. This section presents an overview of the key physical principles governing SOA operation and discusses their implications for next-generation PON design.

3.1.1 SOA Gain Mechanism

An SOA is a current-driven optoelectronic device that provides optical gain through stimulated emission. Its operating principle is closely related to that of a semiconductor laser. However, the SOA employs low-reflectivity end facets, which strongly reduce optical feedback and prevent self-oscillation (i.e., lasing), allowing the device to achieve significant optical gain.

Figure 3.1.(a) illustrates a schematic energy band diagram of a SOA, highlighting the physical mechanisms responsible for optical absorption and gain. In the absence of electrical injection, the conduction band (CB) states within the active region are sparsely populated, while the valence band (VB) states are nearly fully occupied, with only a small fraction of carriers thermally excited across the bandgap. Under these conditions, incident photons with energy $h\nu$ equal to the bandgap energy E_g are predominantly absorbed, promoting electrons from occupied VB states into available CB states, resulting in optical attenuation.

When the SOA is forward biased, electrons from the n-type region and holes from the p-type region are injected into the active region, leading to the establishment of separate electron and hole quasi-Fermi levels. As the injection current increases, the separation between these quasi-Fermi levels increases, and once it exceeds the energy of the relevant interband optical transition, a population inversion is achieved. Under these conditions, incident photons stimulate radiative recombination, producing additional photons that are coherent in phase, frequency, and direction with the input signal, thereby providing optical gain.

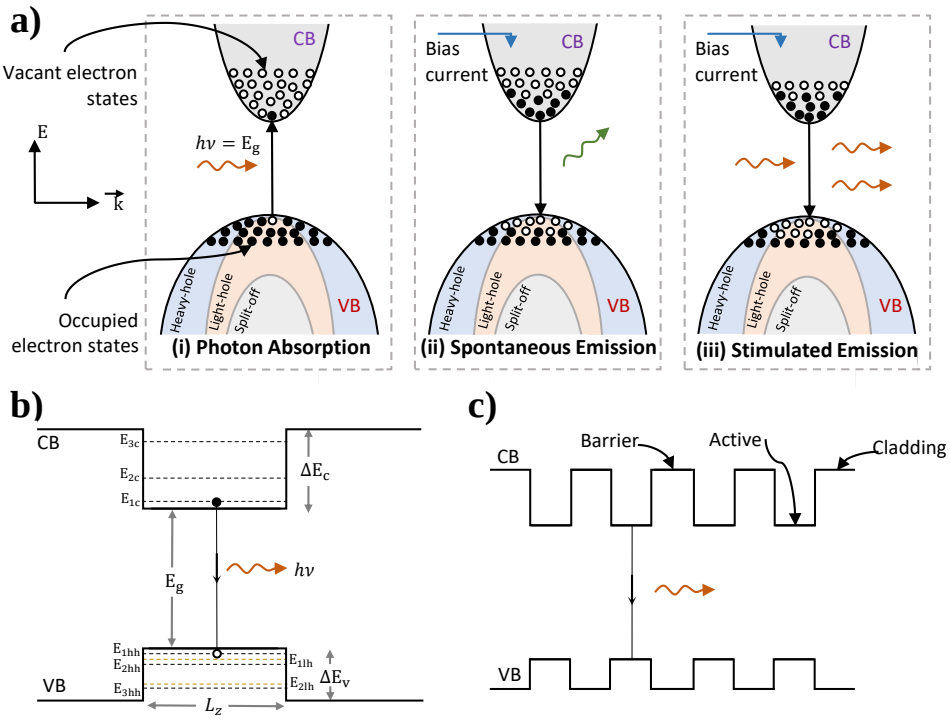


Figure 3.1: (a) Schematic energy band diagram of an InP-based SOA under forward bias, showing carrier confinement in the quantum-well active region, quasi-Fermi level separation, and the optical transitions responsible for (i) absorption, (ii) stimulated emission, and (iii) spontaneous emission. (b) Single quantum-well (SQW) and (c) multiple quantum-well (MQW) band structures illustrating how MQWs increase the effective active region and enhance optical gain compared to SQW.

In modern InP-based SOAs, including the CIP devices used in this work, optical gain is provided by a multiple quantum-well (MQW) active region rather than a bulk semiconductor. Quantum confinement in the growth direction restricts carrier motion and leads to quantised electron and hole energy levels, commonly referred to as subbands, within the active region. A key design objective in many SOAs is to minimise polarisation-dependent gain. This can be addressed through a combination of quantum-well band-structure engineering, where strain engineering is commonly used in strained-MQW designs to reduce polarisation dependence [83], and waveguide or active-region geometry optimisation, in which the waveguide structure (including the active-region geometry) is designed to balance transverse electric (TE) and transverse magnetic (TM) modal confinement [84]. In strained MQW designs, strain lifts the degeneracy of the valence band, resulting in distinct heavy-hole (HH) and light-hole (LH) subbands. In compressively strained MQWs, the HH subband is shifted to higher energy relative to the LH subband, such that optical gain is dominated by transitions involving the

HH subband. As a result, quantum-well band structure and strain engineering influence the relative contributions of TE and TM polarised optical transitions, with strained MQW SOAs exhibiting reduced polarisation-dependent gain and typically favouring TE-polarised amplification [74], [85].

Figures 3.1.(b) and (c) illustrate the evolution from a single quantum-well (SQW) to a strained MQW active region. In an SQW structure, optical gain is provided by a single confined electron–hole system. In contrast, MQW designs employ multiple quantum wells within the same optical mode, increasing the effective active region and improving gain efficiency at moderate carrier densities.

In contrast to the coherent nature of stimulated emission, spontaneous emission occurs continuously within the quantum wells, with carriers recombining randomly to emit photons with uncorrelated phase and direction. These spontaneously emitted photons can subsequently be amplified as they propagate through the gain medium, contributing to ASE noise, which degrades the OSNR of the amplified output.

The electron density N in the conduction band is governed by the balance between carrier injection, recombination, and stimulated emission. Carrier injection increases N by supplying electrons to the active region, whereas recombination processes involving electrons and holes act to reduce it. The temporal evolution of the carrier density can therefore be described by the carrier rate equation

$$\frac{dN}{dt} = \frac{I_{\text{bias}}}{qV} - (AN + BN^2 + CN^3) - \frac{g(N)}{h\nu}P. \tag{3.1}$$

The first term represents carrier generation due to the bias current I_{bias} injected into the active region of volume $V = wdL$, where q is the elementary charge. The second term accounts for carrier loss due to non-radiative (A), radiative (B) and Auger (C) recombination processes. For a small deviation of carrier density from the steady-state value, the recombination term can be linearised and expressed as $\frac{N}{\tau_c}$, where τ_c is the effective carrier lifetime. This approximation is valid under small-signal operation and constant bias conditions. The final term describes carrier depletion due to stimulated emission, where $g(N)$ is the material gain, $h\nu$ is the photon energy, and P is the optical irradiance, defined as the optical power divided by the cross-sectional area of the active region.

Figure 3.2 illustrates the relationship between the carrier density and the injection current in an SOA. As the injection current increases, carriers (electrons and holes) are injected into the active region, causing the carrier density to rise.

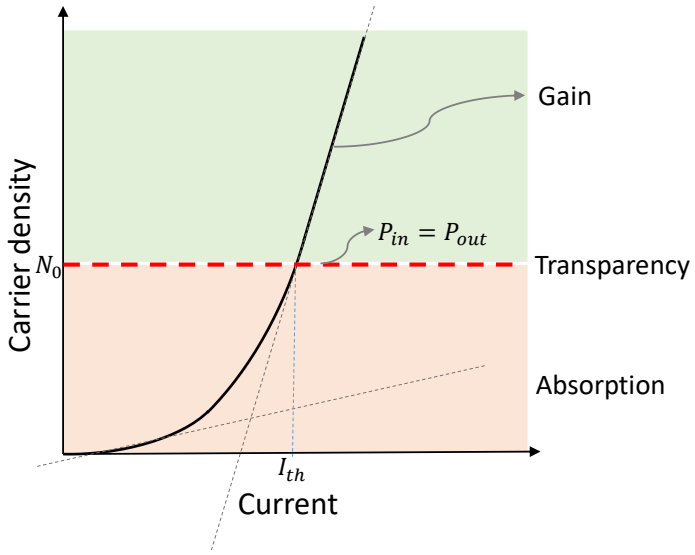


Figure 3.2: Relationship between carrier density and injection current in an SOA. N_0 and I_{th} are the number of carriers and bias current at transparency.

At low injection levels, the carrier density is insufficient to achieve population inversion, and the device exhibits optical absorption, meaning the output optical power is lower than the input power.

As the current approaches a specific value, denoted as the transparency current (I_{th}), the carrier density reaches the transparency carrier density (N_0), at which the optical gain equals the internal optical losses. At this point, the input and output optical powers are equal ($P_{in} = P_{out}$), and the device neither amplifies nor attenuates the signal. When the injection current is increased beyond I_{th}, the carrier density exceeds N_0, leading to population inversion and a net optical gain. In this region, stimulated emission dominates over absorption, and the SOA begins to amplify the optical signal passing through the active medium.

3.1.2 Experimental Devices in This Thesis

Two types of SOAs are used in this work: the *CIP-SOA-S* serves as a preamplifier at the OLT receiver input, while the *CIP-SOA-L* operates as a booster at the ONU side, used exclusively for burst-mode analysis. Although the *CIP-SOA-S* and *CIP-SOA-L* are fabricated using the same material platform and share similar device lengths and active region compositions, they differ in their optical mode confinement and effective mode area, leading to different gain and saturation characteristics [86], [87], [88]. The *CIP-SOA-S* employs a more strongly confined optical mode, resulting in higher net and small-signal gain but lower saturation power, making it well suited to preamplification of weak signals. In contrast, the *CIP-SOA-L*

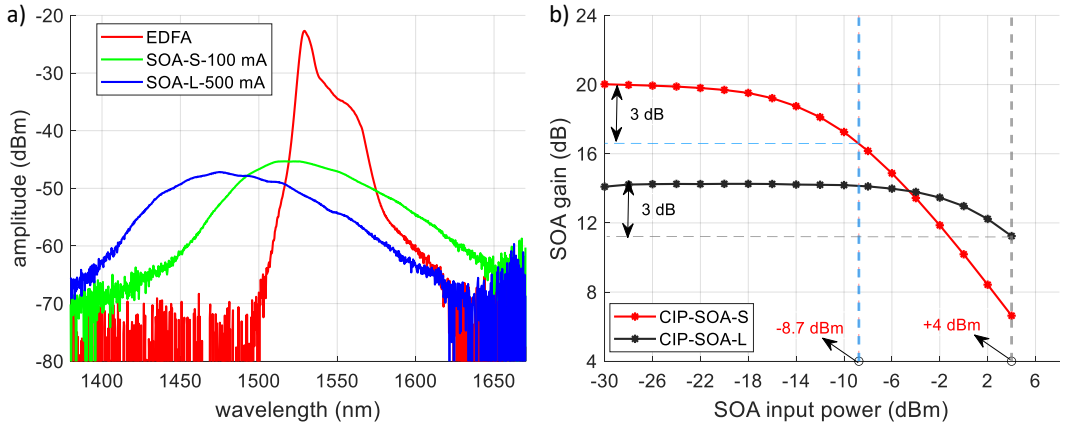


Figure 3.3: Experimentally measured (a) ASE spectra comparison of *CIP-SOA-S* and *CIP-SOA-L* with EDFA, (b) *CIP-SOA-S* (biased at 100 mA) and *CIP-SOA-L* (biased at 500 mA) gain at increasing input power. -8.7 dBm and +4 dBm are saturation input powers for SOA-S and SOA-L at 1535 nm, respectively.

is designed with reduced optical confinement, producing lower net gain but a significantly higher saturation power and reduced gain compression, and is therefore preferred for burst-mode booster operation.

Although erbium-doped fibre amplifiers (EDFAs) offer higher gain and lower noise figures, because of their large size and slow recovery time, they are not considered practical for burst-mode operation and cannot be readily integrated with the receiver [89]. In contrast, SOAs provide compact, bias-tunable gain that can respond rapidly to upstream power fluctuations, making them more suitable for future PON. However, SOAs and doped-fibre amplifiers have different spontaneous-emission (inversion) factors n_{sp} and different residual cavity/waveguide features. Therefore, their ASE spectral densities differ even at the same gain. Figure 3.3.(a) shows the ASE spectra for the *CIP-SOA-S* and *CIP-SOA-L*, compared with a reference EDFA. The EDFA trace shows the minimum-noise benchmark achievable at similar gain; our SOA choices trade some NF/ASE for the fast, bias-tunable gain essential to optical power equalisation in the upstream.

Figure 3.3.(b) reports the measured gain of the SOAs at increasing input power. *CIP-SOA-S* provides a gain exceeding 20 dB and is employed as the preamplifier stage to meet the required power budget. *CIP-SOA-L* offers a lower gain of approximately 14 dB but features a higher saturation input power, which ensures linear operation at elevated input power levels and is therefore utilised as the booster amplifier. Table 3.1 summarises the key experimentally measured parameters of the SOAs considered in this study. Undefined parameters are introduced and

discussed in the subsequent sections of this chapter.

Table 3.1: Comparison of the CIP-SOA characteristics used in this study

	Parameter				
Amplifier	I_{bias} **(mA)**	G_0 **(dB)**	NF **(dB)**	$P_{in,sat}$ **(dBm)**	P_{sat} **(dBm)**
CIP-SOA-S	100	20	6	−8.7	10.6
CIP-SOA-L	500	14	5.1	4	18.4

In the context of the differing optical confinement described above, the higher operating bias current of the *CIP-SOA-L* reflects its dilute-mode design rather than a simple scaling of carrier density relative to the *CIP-SOA-S*. While the carrier rate equation predicts that an increase in injection current leads to an increase in the carrier density in the active region, this relationship depends strongly on the optical confinement factor and the resulting stimulated emission rate. The reduced optical confinement in the *CIP-SOA-L* lowers the net gain per carrier and mitigates self-saturation due to ASE, allowing the device to be operated at higher bias currents without excessive gain compression. In contrast, an SOA with a strongly confined mode similar to that of the *CIP-SOA-S* would be expected to experience significant ASE-induced saturation when driven at comparable current densities. Differences in active region design, such as the number and structure of quantum wells, may further modify the material gain coefficient and transparency carrier density, reinforcing the distinction between the operating regimes of the two devices [88].

From this point onward, unless otherwise stated, all the results presented in this chapter are obtained using the *CIP-SOA-S* device.

3.1.3 Frequency Response

SOAs provide high gain over a broad frequency range, as shown in Figure 3.4. However, their dynamic response is governed by carrier dynamics. When operated in the saturation regime, stimulated emission strongly couples the carrier density to the instantaneous optical power. As the input power increases, stimulated emission introduces an additional carrier depletion channel, effectively reducing the carrier recovery time and making the gain dynamics power-dependent.

At low frequencies, the carrier population is able to follow variations in the optical

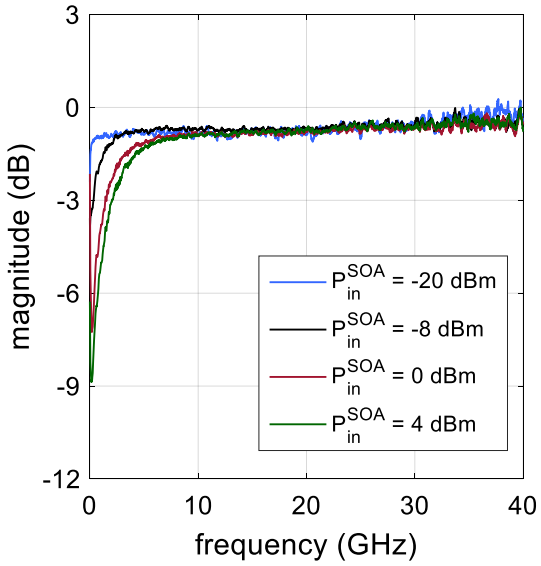


Figure 3.4: Experimental frequency response measurements of *CIP-SOA-S* at varying input power levels. The SOA is biased at 100 mA for all input power levels.

intensity. This results in pronounced gain modulation and compression of slowly varying intensity components. In contrast, at frequencies higher than the carrier response bandwidth, which is determined by the inverse of the effective carrier recovery time, the carrier density cannot respond to rapid intensity fluctuations and remains approximately constant. Under these conditions, the optical field experiences an effectively static gain, and high-frequency components propagate with comparatively little gain-induced distortion.

The apparent suppression of low-frequency intensity variations therefore arises from dynamic gain saturation and the finite carrier response time. Consequently, at high input powers, a saturated SOA acts as a high-pass filter for intensity modulation [90], [91]. In this work, such filtering effects are mitigated using the proposed equalisation techniques.

Consequently, employing SOAs as optical equalisers does not impose additional bandwidth limitations, regardless of the operating gain level.

3.1.4 Gain Response to Optical Bursts

A primary challenge in designing PON receivers is ensuring they can operate in burst mode. Indeed, the upstream preamplifier must be compatible with incoming burst-mode traffic, which can lead to envelope transients or saturation of the amplifier. SOAs are particularly advantageous in this regard due to their

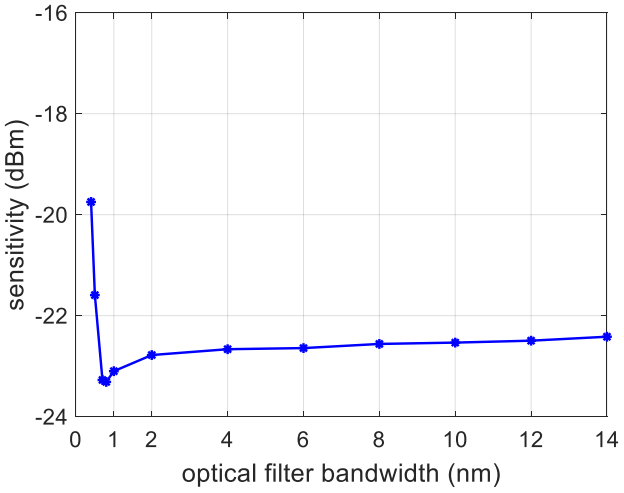


Figure 3.5: The impact of optical filter bandwidth on the receiver sensitivity in an experimental 100 Gb/s PAM4 transmission at BER = 10^{-2}.

significantly faster gain recovery times compared to other optical amplifiers, such as EDFAs. This fast recovery is attributed to the carrier lifetimes (τ_c) in SOAs, which are typically in the order of hundreds of picoseconds [92], whereas EDFAs have carrier lifetimes on the scale of microseconds [93]. The shorter carrier lifetimes in SOAs enable them to quickly return to steady-state gain after experiencing a transient, allowing for rapid adjustments to signal level changes and reducing the duration and impact of gain transients. Consequently, the faster gain recovery time of the SOA simplifies the burst preamble design in PON systems, as the amplifier can more efficiently handle the quick succession of bursts without requiring extensive preamble sequences to stabilise the gain.

3.1.5 BPF for ASE Suppression

The sensitivity of a preamplified receiver is primarily limited by ASE noise generated by the optical amplifier. To mitigate ASE-induced degradation, an optical band-pass filter (BPF) is typically inserted between the preamplifier and the photodiode to restrict noise within a defined bandwidth centred on the signal wavelength. However, the filter bandwidth must be carefully optimised to balance the trade-off between ISI, which increases for narrower filters, and signal–ASE and ASE–ASE beat noise, both of which increase as the filter becomes wider.

As shown in Figure 3.5, receiver sensitivity is evaluated at a BER of 10^{-2} (SD-FEC threshold) for a 50 Gbaud PAM4 PON system emulated with ideal transmitter and receiver components. Measurements are performed for various optical fil-

ter bandwidths using a tunable BPF. However, filter and laser wavelength drifts are not taken into account in these measurements. The optimal sensitivity is obtained with a filter bandwidth of approximately 0.8 nm ($\approx$ 100 GHz), which corresponds to the total optical bandwidth required to pass both sidebands of a 50 Gbaud rectangular-pulse signal. Narrower bandwidths introduce ISI due to spectral truncation, while wider bandwidths lead to only a small BER degradation, as the increase in signal–ASE noise is modest and the contribution of ASE–ASE noise remains limited. This indicates that receiver performance is predominantly governed by signal–ASE beating and that ASE–ASE noise does not become significant within the examined bandwidth range. Consequently, a wideband, wavelength-independent (colorless) optical filter can be employed without causing substantial sensitivity penalties.

3.1.6 Impact of SOA Amplification on Modulated Signal

As mentioned previously, the quality of signals after an SOA is limited by its noise at low input powers, and by signal distortions due to gain saturation at high input powers. This divides the SOA gain operation into three regions: OSNR-limited, linear, and saturation, as shown in Figure 3.6.

When the received optical power is low, the amplifier contributes nearly constant ASE noise that is independent of the input signal level. Consequently, as the amplified signal power decreases, the OSNR degrades significantly, and the receiver operates in an ASE-noise-limited regime.

For large input powers the SOA gain is reduced due to gain saturation. The patterning effect in SOAs, also known as pattern-dependent distortion, arises from the nonlinear interaction between the input signal and the SOA's gain dynamics specifically, gain saturation and finite carrier recovery time. When driven by high-speed modulated data, SOAs operate near or within their gain-saturated regime, where the rate of stimulated emission outpaces the rate of carrier replenishment provided by the bias current. This results in residual carrier depletion that affects the amplification of subsequent bits, causing the SOA's gain to depend not only on the instantaneous input power but also on the history of preceding bits. This temporal memory leads to inconsistent gain across bits of identical logical value but differing contextual patterns, introducing ISI and amplitude fluctuations.

Importantly, variations in carrier density also modify the refractive index of the

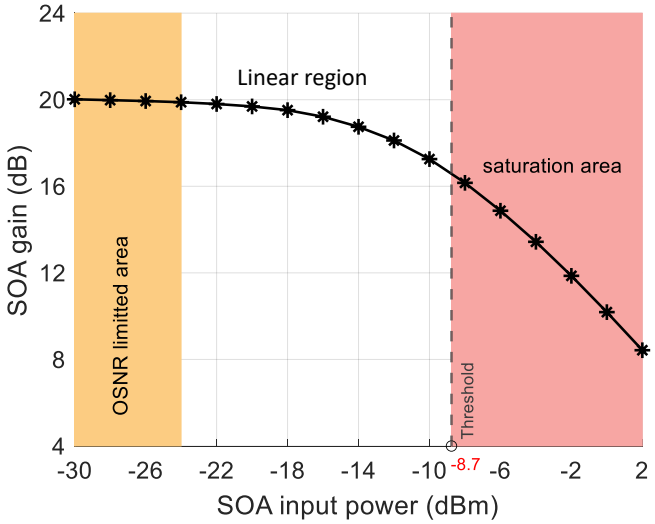


Figure 3.6: Experimental measurement of *CIP-SOA-S* gain variation with increasing input power in three regions: the OSNR-limited regime, the linear operation regime, and the nonlinear (saturation) regime.

SOA active region through amplitude–phase coupling. As a result, the same pattern-dependent carrier dynamics that give rise to gain fluctuations simultaneously induce phase shifts in the amplified optical field.

The severity of this effect is closely linked to the SOA's carrier lifetime, which governs the speed of gain and phase recovery. When the carrier recovery time is on the order of the bit period, the SOA cannot fully recover between pulses, particularly under high-power or closely spaced bit sequences. This mismatch in time scales causes the SOA to respond differently to similar symbols depending on their temporal context, distorting both the amplitude and phase of the output waveform and degrading signal fidelity. The patterning effect is especially critical in burst-mode or dynamically varying traffic scenarios, where varying power levels and data sequences impose additional strain on the amplifier's gain recovery. In essence, the patterning effect reflects the nonlinear, memory-like behaviour of SOAs, posing a fundamental limitation to their use in systems requiring precise and consistent amplitude and phase preservation.

While the patterning effect is fundamentally rooted in the gain dynamics of SOAs, its impact is highly dependent on the modulation format. This is because different modulation schemes encode information in distinct signal domains, amplitude, phase, or both, and interact with nonlinear gain saturation in unique ways. In the following, the effects of reduced OSNR and patterning introduced by SOA amplification are analysed for different modulation formats to clarify their impact on system performance.

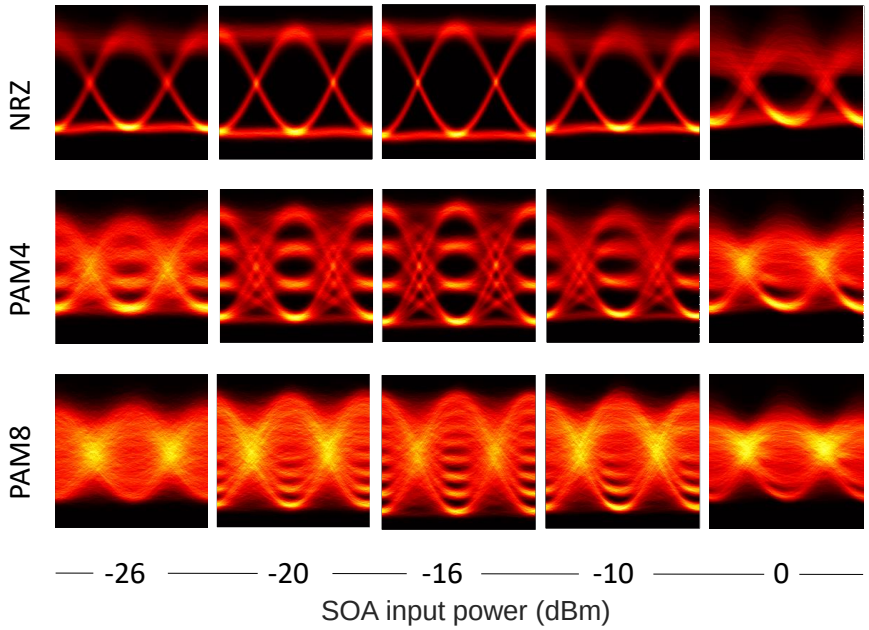


Figure 3.7: Experimental evaluation of the impact of reduced OSNR and gain saturation in *CIP-SOA-S* on 50 Gbaud M-PAM transmission.

M-PAM-IM/DD PON

Figure 3.7 shows the impact of the SOA on signals with different modulation formats, all operating at a symbol rate of 50 Gbaud and evaluated over increasing input power levels. At low input powers, the amplifier operates in the linear regime, but the received signal is affected by a low OSNR. In this regime, the ASE field adds random amplitude fluctuations to the signal, resulting in reduced eye opening between adjacent intensity levels.

As the input power increases, the signal OSNR improves, but the SOA begins to saturate. Gain saturation causes amplitude compression, particularly in the higher power levels, introducing nonlinear distortion and patterning effects. At the highest input powers, deep gain saturation severely distorts the waveform, producing strong level compression and inter-symbol dependence that results in eye closure. The severity of distortion depends on the modulation format: multi-level PAM signals are more susceptible to both ASE noise and gain compression than binary NRZ, owing to their smaller level spacing and higher linearity requirements.

Advanced Modulation-Coherent PON

Figure 3.8 shows the DP-QPSK and DP-16QAM constellation diagrams obtained at different input power levels into the SOA. At low input powers, the low-OSNR

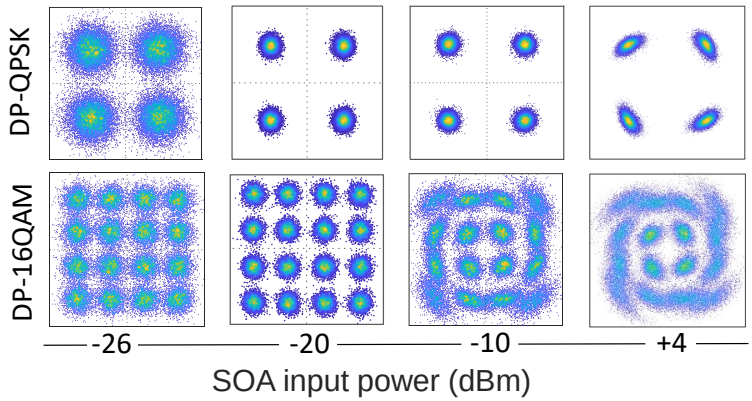


Figure 3.8: Experimental constellation diagrams showing the impact of *CIP-SOA-S* amplification on DP-QPSK and DP-16QAM signals at increasing input power levels.

condition leads to dominant ASE noise, introducing random amplitude and phase fluctuations that cause the constellation points to spread uniformly around their ideal positions. For DP-16QAM, this broadening increases the overlap between neighbouring symbols, reducing the distinction between inner and outer points. As the input power increases, the OSNR improves and the constellation diagrams become more distinct. However, once the SOA enters gain saturation, nonlinear amplitude and phase distortion appear. The arc-like deformation of the DP-QPSK and DP-16QAM constellations observed at high input powers is consistent with the saturation-induced amplitude and phase distortions discussed in Chapter 2. The experimentally generated DP-QPSK signal is not strictly constant-envelope in time, as pulse shaping and the I/Q modulator introduce residual amplitude modulation during symbol transitions, resulting in small instantaneous optical power variations. When the signal is amplified in the gain-saturated regime of an SOA, these variations can interact with nonlinear gain dynamics and amplitude–phase coupling, leading to observable phase distortion. In DP-16QAM, both amplitude and phase are modulated, and the signal inherently contains multiple power levels. As a result, symbol-to-symbol optical power variations are more pronounced, and the finite carrier recovery time of the SOA gives rise to patterning effects. These patterning effects lead to amplitude compression and power-dependent phase shifts, which predominantly affect the outer constellation points and enhance their deformation under gain saturation.

3.2 Method A: Variable Bias

In this section, we present the first of two techniques investigated in this thesis for SOA-based power equalisation in high-speed PONs. The variable bias technique relies on dynamically controlling the SOA gain through adjustment of its bias current. The main objective of this approach is to stabilise the output power of upstream packets, thereby mitigating the distortions caused by SOA saturation while maintaining a sufficiently large DR for PON operation. This section first introduces the underlying gain control mechanism and then discusses the achievable gain control levels and parameters that determine the target output power. Although the measurements are performed in the C-band, the same bias-tuning principle applies to O-band SOAs, supporting broader applicability across access network wavelength bands.

3.2.1 Gain Control Mechanism

The principle of this method is to vary the SOA bias current as a function of the input packet power. In conventional operation with fixed bias, high-power packets drive the SOA into gain saturation, which introduces nonlinear distortions such as patterning effects and degrades the BER performance. To avoid this, the bias current is reduced for high input power levels, thereby lowering the small-signal gain and preventing the SOA from entering the deep saturation regime.

Mathematically, the SOA gain G under saturation is governed by the transcendental relation [94]

$$G(P_{\text{in}}, I_{\text{bias}}) = G_0 \exp\left(-(G-1)\frac{P_{\text{in}}}{P_{\text{sat}}}\right), \tag{3.2}$$

where I_{bias} is the bias current, G_0 is the small-signal gain, P_{in} is the instantaneous packet input power, and P_{sat} denotes the saturation power, which itself depends on the carrier density controlled by I_{bias}. To obtain an analytically tractable expression for system-level analysis, the exponential term in the gain equation is expanded using a Taylor series. Retaining only the first-order term, which is valid in the weak-saturation regime ($P_{\text{in}}/P_{\text{sat}} \ll 1$), yields

$$G \approx G_0\left(1 + \frac{P_{\text{in}}}{P_{\text{sat}}} - G\frac{P_{\text{in}}}{P_{\text{sat}}}\right). \tag{3.3}$$

Rearranging this expression leads to the commonly used closed-form approxima-

tion

$$G \approx \frac{G_0 \left(1 + \frac{P_{\text{in}}}{P_{\text{sat}}}\right)}{1 + G_0 \frac{P_{\text{in}}}{P_{\text{sat}}}}. \tag{3.4}$$

Although this expression is not an exact solution of the gain equation, it provides an efficient and analytically tractable model that captures the gain behaviour in both the low and high input power regimes. By lowering I_{bias} for strong input packets, both G_0 and P_{sat} decrease, ensuring that the output remains below the nonlinear saturation threshold.

This bias control scheme effectively equalises the packet output power, reducing the gain fluctuations and mitigating saturation-induced penalties. However, operating at low bias currents can degrade the amplifier's noise figure, which introduces a trade-off between dynamic range extension and SNR performance.

3.2.2 Features: Gain Change and Target Output Power

The target of this technique is to maintain the SOA output power at a constant level, independent of the input power variations. Based on experimental evaluation, the optimum target is found to be around -2 dBm, which provides a balance between ensuring sufficient launch power to the receiver and avoiding nonlinear distortions at high input powers.

To achieve this, the bias current is dynamically adjusted such that:

$$P_{\text{out}} \approx P_{\text{target}} \quad \forall\, P_{\text{in}} \in [P_{\text{min}}, P_{\text{max}}], \tag{3.5}$$

where P_{target} is the desired constant output power and $[P_{\text{min}}, P_{\text{max}}]$ denotes the input power dynamic range.

Figure 3.9.(a) shows the SOA gain spectrum across the C-band under three conditions: maximum gain at high bias and low input power, and reduced gain at lower bias currents with higher input power. A tuning range of $>$20 dB is demonstrated across the band. This confirms that bias control enables wide-range SOA equalisation suitable for burst-mode PONs.

Figure 3.9.(b) further illustrates that lowering the bias shifts the SOA away from saturation, allowing controlled gain adjustments across the full input dynamic range. To maintain sensitivity and suppress patterning effects, the SOA output power is fixed at -2 dBm through bias level adjustment for each packet. Figure 3.9.(b) confirms that this prevents deep saturation, as the SOA operating

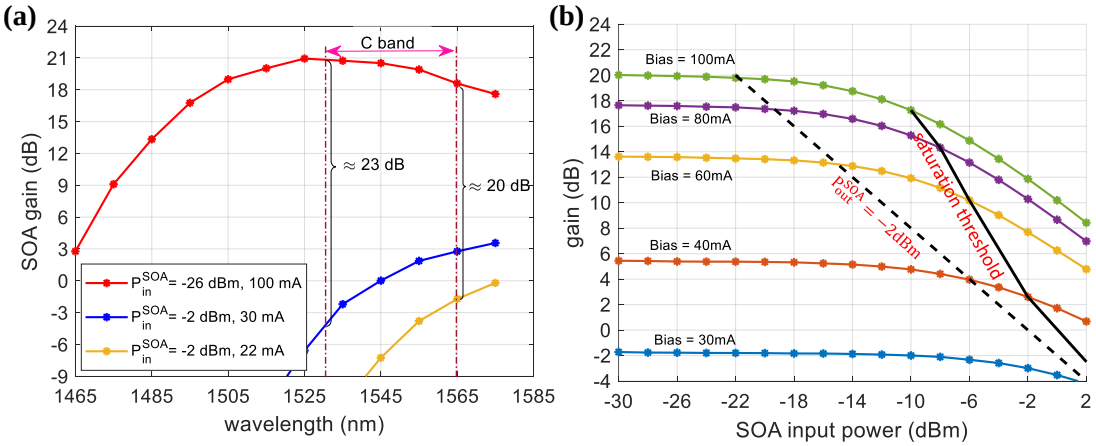


Figure 3.9: Experimentally measured (a) *CIP-SOA-S* gain spectrum highlighting the effect of bias current on gain change, and (b) gain measurement as a function of increasing input power at multiple bias currents, solid black line is gain versus saturation input power levels and dashed black line shows the required gain to fix the output power at -2 dBm by increasing the input power.

condition (dashed black line) remains always below the saturation threshold (solid black line) across the entire range of input signal powers. By tuning the bias between 30 mA and 100 mA, the system achieves power equalisation exceeding 21 dB.

3.3 Control light injection

The control light injection technique employs a local optical source, separate from the signal light, to regulate SOA gain by modifying its saturation dynamics. By inducing additional stimulated emission, the control light depletes carrier density and compresses gain, effectively reducing signal amplification for high signal input power packets. This controlled saturation suppresses nonlinear distortions in high-power signals (loud packets) and enables gain regulation without directly adjusting the SOA's bias current.

This section introduces the gain control principle of the technique and then discusses three important aspects: the wavelength optimisation of the control light, the choice of propagation direction, and the achievable gain control level and target output power. The findings of this section are also applicable to O-band SOAs.

3.3.1 Gain Control Principle

Carrier concentration N under the influence of two light sources at different wavelengths can be described by [95]:

$$\frac{dN}{dt} = \frac{I_{\text{bias}}}{qV} - (AN + BN^2 + CN^3) - \frac{g_1(N)}{h\nu_1}P_1 - \frac{g_2(N)}{h\nu_2}P_2, \tag{3.6}$$

where P_1 and ν_1 represent the signal power and frequency, respectively, P_2 and ν_2 correspond to the control light power and frequency. The terms $g_1(N)$ and $g_2(N)$ denote the material gain coefficients of the SOA at the signal and control light wavelengths, respectively.

By inducing additional stimulated emission, the control light depletes carrier density and compresses gain, effectively reducing signal amplification for high signal input power packets. This controlled saturation suppresses nonlinear distortions in high-power signals (loud packets) and enables gain regulation without directly adjusting the SOA's bias current.

3.3.2 Optimisation of Control Light Wavelength

The performance of control light technique is strongly influenced by the wavelength selection of both the signal and control light, as they dictate gain optimisation. In this study, wavelengths are strategically chosen to enhance dynamic range while reducing the power demand of the control light.

The optimal placement of the control light is analysed by varying its wavelength and measuring the resulting gain reduction. The results of this are shown in Figure 3.10. In (a), at high input powers, the SOA's gain peak wavelength shifts toward longer wavelengths (red shift) due to saturation effects, consistent with the simulation results. This suggests that placing the control light at a longer wavelength enhances carrier depletion in the active region, leading to greater gain reduction for the signal, as confirmed experimentally in Figure 3.10.(b).

To quantify this effect, control light is applied across the 1505–1575 nm range, with power levels up to +6 dBm for a signal at 1535 nm and lower -30 dBm input power. The SOA bias current was fixed at 100 mA, resulting in a small-signal gain of 20 dB, which is sufficient to provide the required sensitivity. The signal is placed at 1535 nm because this wavelength lies near the SOA gain peak under small-signal conditions, providing strong amplification and maximising receiver sensitivity. The results demonstrate that positioning the control light at

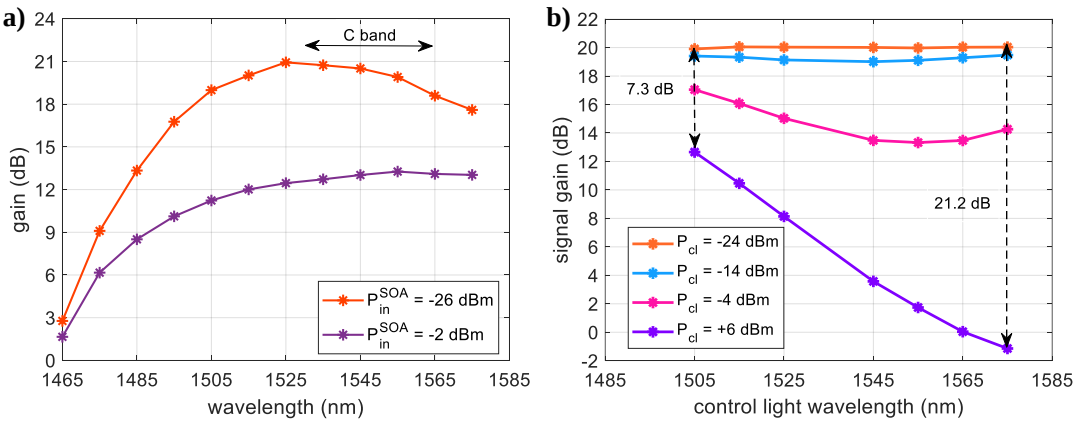


Figure 3.10: Experimental measurement of (a) *CIP-SOA-S* gain spectrum highlighting the peak gain wavelength shift at high input powers, (b) signal gain at -30 dBm input power to the SOA for a signal placed at 1535 nm, measured for various control light power levels at different control light wavelengths.

wavelengths longer than 1565 nm enables gain reduction exceeding 20 dB, and therefore achieves the desired dynamic range. Similar gain reduction can also be achieved in O-band SOAs, provided the signal and control light wavelengths are properly chosen, as the gain bandwidth and optimal wavelength separation may vary.

3.3.3 Injection Direction of Control Light

Another important parameter of Method B is the propagation direction of the control light relative to the signal. Two options exist: co-propagating injection, where the control light enters from the same facet as the data signal, and counter-propagating injection, where the control light is launched from the output facet.

Co-propagating injection requires an additional wavelength division multiplexer (WDM) or coupler to combine the control light with the signal at the SOA input, introducing additional loss compared to the bias control approach. However, if a custom-designed wavelength multiplexer is used, this loss can be minimised to approximately 1 dB. Although, counter-propagating injection eliminates this requirement, and avoids input-side losses, it increases NF as explained in the following.

Considering the SOA as a chain of amplifiers, corresponding to virtual subsections of the device. For each subsection, there is an associated NF and gain, G. Total

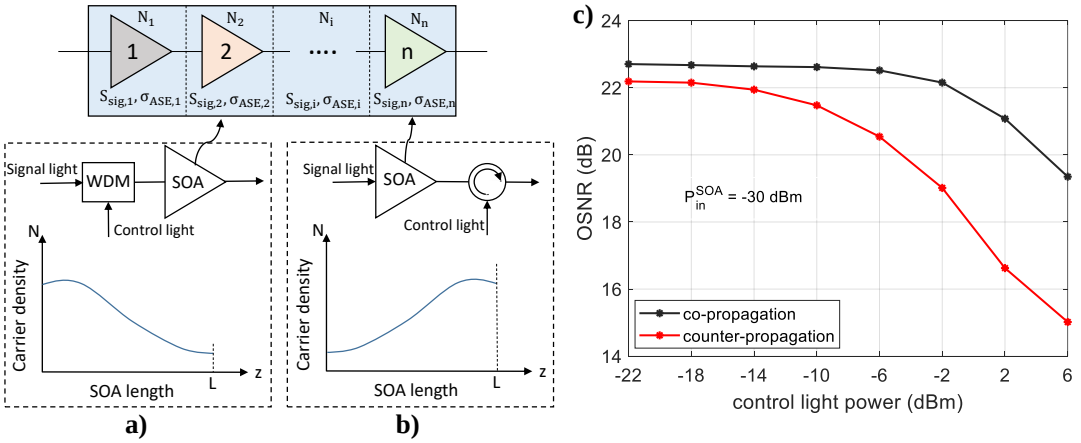


Figure 3.11: (a) Co-propagation injection scheme, (b) counter-propagation injection scheme. The SOA is longitudinally divided into n sections of equal length, and the carrier density graphs correspond to the case where the control light power is much higher than the input power. (c) Experimentally measured OSNR comparison of the two propagation schemes as a function of control light power at an SOA input power of -30 dBm. The loss of the WDM is not taken into account in this measurement.

noise figure is then given by the following equation [96]:

$$NF_{\text{tot}} = NF_1 + \frac{NF_2 - 1}{G_1} + \cdots + \frac{NF_n - 1}{G_1 \ldots G_{n-1}} \tag{3.7}$$

Therefore, the total NF is minimised if the low noise components are placed at the input of the SOA [97], [98]. To conform to this condition, a high number of carriers must be provided at the initial section of the amplifier to achieve a high level of population inversion, thus lowering the inversion factor leading to lower total NF and consequently increasing the overall OSNR.

The direction of control light injection strongly influences the carrier density distribution inside the SOA, and thus the resulting ASE noise performance [99]. When the control light is injected in the co-propagating direction, the carrier density is higher at the initial section of the amplifier and gradually decreases along the amplifier length in the same direction as the signal, as shown in Figure 3.11.(a). As a consequence, the accumulation of ASE is minimised, leading to lower output noise.

In contrast, counter-propagating injection introduces the control light from the output facet. As shown in Figure 3.11.(b), in this configuration the carrier density is higher near the output section of the SOA and lower at the input. As a result, the signal initially propagates through a region of lower carrier den-

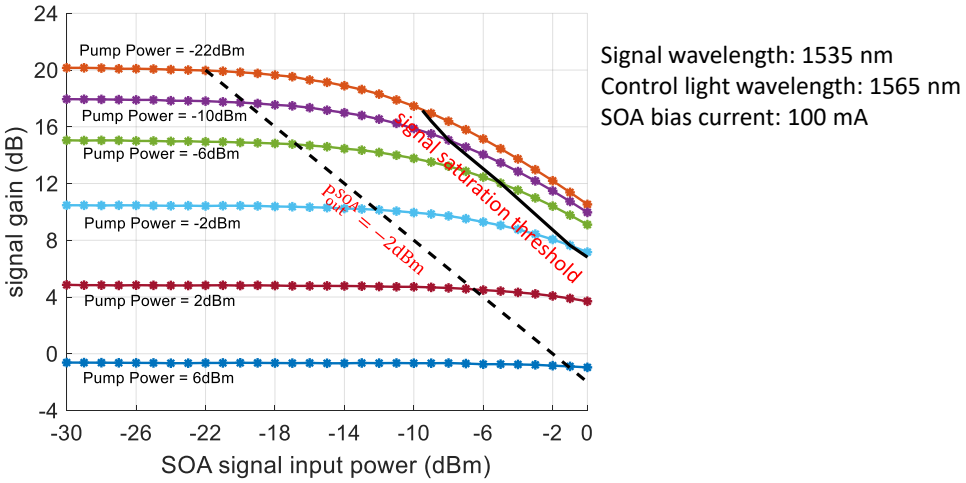


Figure 3.12: Experimentally measured SOA signal gain as a function of increasing input power for multiple control light power levels. Solid black line is gain versus signal saturation input power levels and the dashed black line shows the required signal gain to fix the output power at -2 dBm by increasing the input power.

sity and experiences stronger ASE generation before reaching the denser carrier population region near the output. This imbalance leads to less efficient gain regulation and a measurable degradation in OSNR, as observed experimentally in Figure 3.11.(c). In this experiment signal and control light are placed at 1535 nm and 1565 nm, respectively.

3.3.4 Dynamic Range and Target Output Power

Just like the other technique, the objective here is to fix the output power at a certain level and extend the dynamic range. To provide a higher sensitivity and give a fair comparison with the other technique, the output power of the SOA is fixed to -2 dBm using this technique.

Figure 3.12 illustrates the SOA gain as a function of increasing input power for multiple control light power levels. As shown, control light injection enables controlled gain adjustment across the full input dynamic range. The figure also demonstrates that adjusting the control light power to maintain the SOA output at -2 dBm (black dashed line) keeps the amplifier within the linear regime, ensuring a significant margin from the signal saturation threshold (solid black line). This enables more effective handling of high-power signals (loud packets) compared to the variable bias approach.

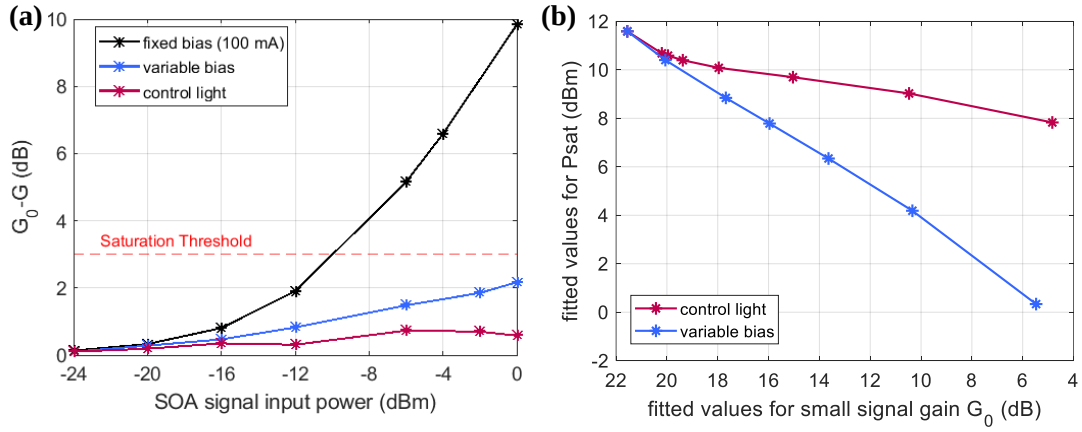


Figure 3.13: Experimental measurement of (a) SOA signal gain reduction compared to the small-signal gain, with a 3 dB drop defined as the saturation threshold across different operating modes, and (b) Fitted values of saturation power versus small signal gain.

3.4 Comparison of two methods

In this section, the effectiveness of the SOA-based power equalisation techniques is evaluated by comparing their impact on the following parameters: saturation input power, saturation output power, and OSNR.

Saturation input power ($P_{\text{in,sat}}$)

$P_{\text{in,sat}}$ is considered as a practical threshold for SOA nonlinearity induced by the patterning effect, which determines the dynamic range extension.

Figure 3.13.(a) compares the SOA's signal gain reduction relative to the small-signal gain G_0, with and without packet power level equalisation, where the 3 dB drop marks the saturation threshold. Without gain control, the amplifier enters deep saturation, which would lead to significant nonlinear distortions and patterning effects. In contrast, the proposed techniques provide more effective gain regulation, preventing saturation even at higher input power levels. Notably, control light injection outperforms the variable bias approach by keeping the SOA further from the saturation regime. When the control light is injected from the input side of the SOA, it dominates stimulated emission near the input section and limits the initial amplification of the data signal. As a result, the data signal removes fewer carriers at the SOA entrance, allowing the carrier population to remain high in this region. Consequently, a larger input signal power is required to induce strong carrier depletion and gain compression, leading to an increased saturation input power compared to variable bias.

Saturation power (P_{sat})

Saturation power of the SOA is defined by:

$$P_{\text{sat}} = \frac{h\nu A}{\Gamma a \tau_{\text{c}}}, \tag{3.8}$$

where $h\nu$ is the photon energy, A is the active region cross-sectional area, Γ is the optical confinement factor, a is the differential gain, and τ_c is the effective carrier lifetime and depends on the carrier density and therefore varies indirectly with the bias current through recombination processes in the SOA. As the bias current increases, the steady-state carrier density increases, leading to higher recombination rates and a reduction in the effective carrier lifetime. The saturation power P_{sat} exhibits wavelength dependence through both the photon energy and the wavelength dependence of the differential gain and the optical confinement factor.

By fitting the measured data to the gain expression 3.4, we estimate the small-signal gain G_0 and saturation power P_{sat}, as shown in Figure 3.13.(b) Scheme B demonstrates a notable advantage over the previous method (Scheme A) by maintaining the signal saturation power at a higher level. This is because control light's contribution to stimulated emission is strongest near the input and decreases toward the output as it propagates. Consequently, the effective population inversion increases toward the output, forming an asymmetric longitudinal gain profile that suppresses ASE buildup and increases the saturation output power compared to variable bias.

Optical Signal-to-Noise Ratio

Figure 3.14.(a) presents the OSNR degradation associated with different power equalisation techniques when the SOA output power is maintained at -2 dBm, comparing it to a fixed bias configuration. OSNR values are measured using an optical spectrum analyser with 0.1 nm resolution. At low input power levels, all configurations exhibit nearly identical OSNR, leading to similar BER performance. However, as input power increases, OSNR divergence emerges due to variations in the spatial carrier distribution within the SOA. These differences in carrier distribution result in varying levels of spontaneous emission amplification along the direction of forward signal propagation.

The OSNR degradation in the variable bias scheme at high input powers, compared to the fixed bias case, is primarily attributed to lower carrier density, which

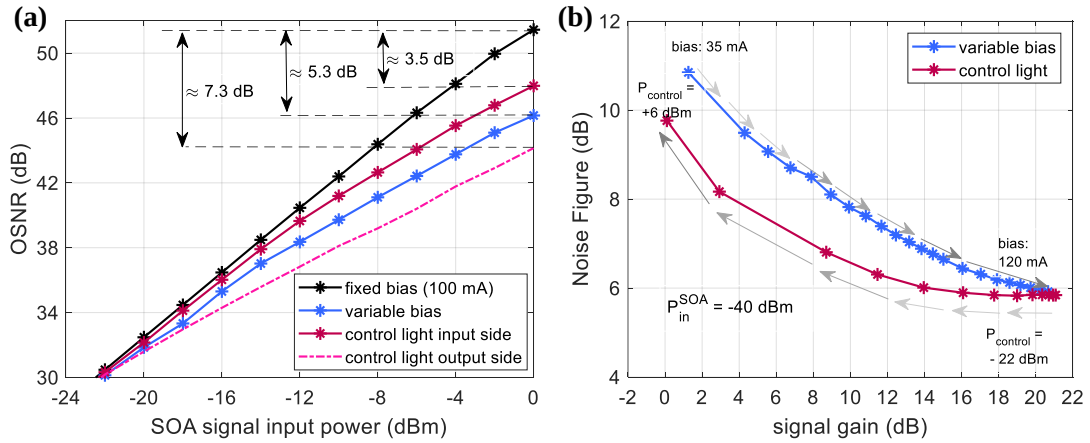


Figure 3.14: (a) Experimental OSNR measurement as a function of SOA signal input power before and after equalisation using the proposed schemes. The OSNR for control light injected from the SOA output is also included. (b) Experimental Noise figure measurement versus small signal gain after equalisation using the proposed techniques.

reduces signal gain while allowing greater ASE accumulation along the SOA. In contrast, reducing gain via control light injection instead of bias control modifies the carrier density profile differently, as explained in the previous section, depending on the injection point. The figure analyses control light injection from both the input and output sides to provide deeper insight into how carrier density redistribution affects ASE accumulation and OSNR performance.

It is important to note that for all three gain control schemes employed in Figure 3.14 (variable bias, control light input side and control light output side), the gain experienced by the signal remains the same at any given input power, as this is a fundamental principle of the power equalisation scheme.

When injected from the input side, control light reduces carrier density at the SOA output, resulting in higher initial gain that gradually decreases due to progressive carrier depletion. This limits ASE accumulation, as gain is highest at the input and decreases toward the output, explaining why this configuration outperforms the variable bias approach. Conversely, injecting control light from the output side increases carrier density at the SOA output while depleting carriers at the input end, reducing gain for both the signal and spontaneous emission at the signal input end. As the signal propagates, gradual amplification leads to greater ASE accumulation, resulting in the worst OSNR performance among all configurations.

Figure 3.14.(b) also compares the measured noise figure for two schemes. The

noise figure is measured at –40 dBm to ensure strictly small-signal operation of the SOA. Since the purpose of this measurement is to compare the impact of different gain-control techniques on the intrinsic noise performance, it is necessary to eliminate signal-induced gain compression effects. At –40 dBm, carrier depletion due to stimulated emission is negligible, and the amplifier operates in its linear regime. Therefore, any observed differences in noise figure can be attributed to the gain-control method itself rather than to power-dependent saturation effects. The noise figure and OSNR are related by the following equation:

$$NF = \frac{P_{\text{in}}}{\text{OSNR}\ h\nu\Delta\nu_{ref}} + \frac{1}{G} \approx \frac{P_{\text{in}}}{\text{OSNR}\ h\nu\Delta\nu_{ref}}, \quad \text{if} \quad G \gg 10, \tag{3.9}$$

where $\Delta\nu_{ref}$ is the reference noise bandwidth. For sufficiently large gain, the term $1/G$ becomes negligible, leading to the simplified expression.

Overall, both variable bias and control light techniques effectively regulate SOA gain while maintaining the desired dynamic range and enhancing linearity. However, control light injection (from input side) offers a more effective approach than variable bias adjustment, as it better regulates the spatial carrier density distribution and minimises ASE accumulation. By optimising the control light injection wavelength and power, higher OSNR and enhanced SOA linearity can be achieved, making this technique a promising solution for high-speed optical communication systems.

3.5 Real Implementation Complexity Analysis

Figure 3.15 illustrates the configuration of SOA gain controllers for a high-speed PON transmission using two proposed equalisation techniques. While the control circuit is not physically implemented in our experiment, the following describes how such a system can operate in practice.

An FPGA-based controller running at a 300 MHz clock (i.e., sampling every 3.33 ns) processes the optical envelope captured by a high sensitivity photodiode. This photodiode is designed for envelope detection and distinguishes the start of a burst (on-state) from guard-band zeros (off-state) by detecting amplitude transitions, even for weak signals, without requiring high-speed sampling. This signal is digitised by an ADC operating at gigasamples per second with nanosecond-scale latency. The FPGA monitors the envelope to detect a rising edge, which marks the start of a burst. By averaging the initial samples over a short window

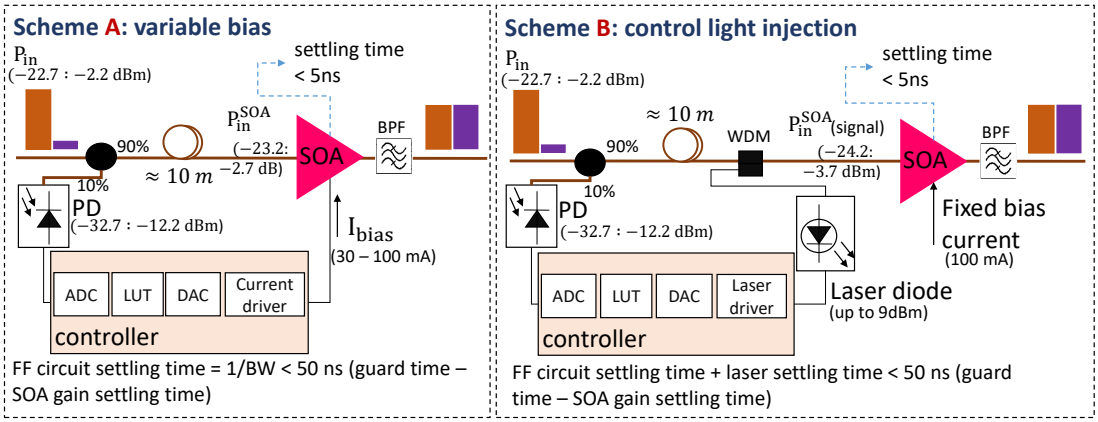


Figure 3.15: The SOA gain controller structure for the two proposed equalisation methods: (A) variable bias, and (B) control light injection.

(e.g., 10 to 20 ns), the controller classifies the burst amplitude and uses a lookup table (LUT) to select the appropriate SOA bias current or control laser power. The LUT can be indexed by measured burst power and wavelength and preloaded into the OLT controller. Since equalisation depends only on locally measured input power, upstream link changes do not impact the LUT. However, temperature drift and device ageing can gradually alter the SOA's gain response. To maintain performance, embedded monitoring photodiodes at the SOA output can track deviations from expected output power. If discrepancies persist, the system can initiate recalibration routines either periodically during idle periods or adaptively in the background to update the LUT and restore accuracy. This control value is then sent to a digital-to-analogue converter (DAC) and an appropriate driver to apply the required gain just before the burst reaches the SOA. With a fibre delay of approximately 10 meters (about 50 ns) in the main signal path, the system has sufficient time to complete burst detection and gain adjustment. A similar method detects the end of a burst by monitoring for a falling edge in the envelope. For the control light scheme, a wavelength multiplexer combines the control light with the signal, introducing additional insertion loss compared to the variable bias approach. However, if a custom-designed wavelength multiplexer is used, this loss can be minimised to approximately 1 dB.

The feasibility of the proposed control scheme is supported by prior implementations in related applications. A feed-forward SOA bias control loop with a total response time under 50 ns was demonstrated in [100], showing that real-time operation is achievable within typical burst-mode timing constraints. A photonic integrated circuit in [101] used FPGA-based control to adjust SOA bias

currents (30–100 mA) for burst equalisation in 40 Gb/s NRZ and 20 Gb/s PAM4 systems with a 60 ns guard time. In [102], an FPGA-controlled optical switch achieved a 43.4 ns switching time, further confirming the viability of nanosecond-scale SOA control. Lastly [103], demonstrated a low-latency FPGA system with integrated ADCs, DACs, and LUT-based nonlinear processing for quantum computing. While the application differs, its architecture, using pre-calibrated LUTs and nanosecond-scale data converters, aligns closely with the control structure proposed in this work. These examples collectively support the practicality of implementing the proposed feed-forward control within nanosecond timing budgets.

In our experimental setup, burst-by-burst gain switching is performed in real-time using an arbitrary function generator (AFG). The AFG is programmed with a waveform that is synchronised with the arrival of each burst. This waveform is generated using pre-calibrated data, which maps expected burst amplitudes to corresponding SOA bias currents (Scheme A) or control light levels (Scheme B). Due to the monotonic nature of the SOA response, only 10–20 calibration points are typically required. As a result, different gain levels are applied to different bursts, effectively emulating the behaviour of a real-time controller.

3.6 Summary

This chapter investigates the use of SOAs for burst power equalisation in high-speed PON receivers. The study begins by analysing SOA gain characteristics and their nonlinear effects on modulated signals operating at 50 Gbaud. It is shown that SOA gain saturation can significantly degrade different modulation formats. For M-PAM signals, the dominant impairment arises from patterning effects caused by carrier depletion and finite carrier recovery. For dual-polarisation QPSK and 16QAM, SOA saturation introduces nonlinear amplitude and phase distortions that deform the signal constellation. In 16QAM, stronger symbol-to-symbol power variations lead to pronounced patterning effects that further enhance this degradation.

To mitigate these nonlinearities, two optical equalisation techniques are proposed and analysed: variable bias and control light injection. Both methods regulate the SOA gain to maintain a constant output power across a wide input range, effectively extending the amplifier's linear operating region and improving receiver sensitivity. The results demonstrate that these equalisation techniques

can provide more than 20 dB of gain adjustment, satisfying the dynamic range requirements of the latest 50G-PON standard.

Among the two approaches, the control light injection method offers better OSNR and linearity at high input powers. The analysis also reveals that injecting the control light from the SOA input side increases the carrier density at the amplifier entrance and improves the OSNR by approximately 4 dB compared with output-side injection. In addition, positioning the control light at longer wavelengths, consistent with the red-shift of the SOA gain spectrum at high input powers, enhances carrier depletion and provides a larger gain variation.

Overall, the findings confirm that SOA-based optical equalisation is an effective, scalable, and low-complexity solution for next-generation high-speed PON systems, while also providing deeper insight into the nonlinear behaviour of SOAs and their impact on advanced modulation formats.

Chapter 4

SOA-Based Power equalisation on a 100G IM/DD PON

This chapter investigates SOA-based optical power equalisation in 100G IM/DD PON, demonstrating wide dynamic range performance in both continuous and burst-mode transmission. The proposed techniques are evaluated against the latest 50G-PON standard requirements, showing that they meet the optical power budget, dynamic range, and dispersion tolerance targets. In addition, high-speed system results using a transfer-printed SOA are presented to highlight the potential for scalable integration.

Future high-speed PONs must meet a stringent optical power budget of 29 dB while accommodating spectrally efficient modulation formats, such as PAM4. To satisfy this requirement, preamplification at the OLT is essential. In this thesis, the preamplifier not only enhances receiver sensitivity but also performs optical-domain burst power equalisation, mitigating the large dynamic range of upstream packets before detection. This approach alleviates the bandwidth, gain, and linearity constraints of conventional burst-mode TIAs, which become increasingly difficult to realise for multi-level modulation at high baud rates.

This chapter bridges the theoretical foundations of SOA-based equalisation with their experimental validation. Continuous-mode demonstrations at 100 Gb/s confirm the feasibility of adaptive SOA gain-control techniques using both a commercial *CIP-SOA-S* and a TP-SOA representing a scalable and integration-

friendly platform for future low-cost PON receivers. Since practical PONs operate exclusively in burst-mode, the work further investigates the transient behaviour and equalisation performance of SOAs under realistic operating conditions.

Recently, higher-order modulation formats such as PAM8 have been investigated as a means to further increase PON capacity beyond 100 Gb/s, offering improved spectral efficiency compared to PAM4 [104], [105], [106], [107], [108]. However, these formats impose tighter SNR and linearity requirements on the optical front end. To assess the feasibility of extending SOA-based equalisation to such advanced formats, this chapter also examines 150 Gb/s PAM8 transmission using the same equalisation schemes.

4.1 Rationals and Research Aims

Although the potential of SOAs as preamplifiers in PON receivers is well recognised, their behaviour under high-speed, burst-mode IM/DD operation remains insufficiently understood. Previous analyses have mostly focused on downstream transmission or continuous-wave conditions, which do not capture the transient effects, saturation dynamics, and recovery behaviour that occur when packet powers vary rapidly between bursts. A deeper experimental investigation is therefore required to establish whether SOA gain control can provide stable and distortion-free equalisation with realistic upstream traffic.

Another key motivation is to assess the practicality of implementing such equalisation schemes using commercially available and integration-compatible SOAs. Demonstrating that gain control can be achieved with commercial discrete devices, such as the *CIP-SOA-S*, or with transfer-printed SOAs on silicon photonic platforms would validate the approach as a viable path toward scalable, low-cost receiver designs suitable for future PON generations.

Finally, while PAM4 represents the leading candidate for 100 Gb/s IM/DD PONs, recent studies have explored higher-order formats such as PAM8 to further increase capacity. Investigating the performance of SOA-based equalisation under PAM8 transmission provides valuable insight into the limits of this technique and clarifies whether such modulation formats can be supported without excessive signal degradation or noise accumulation.

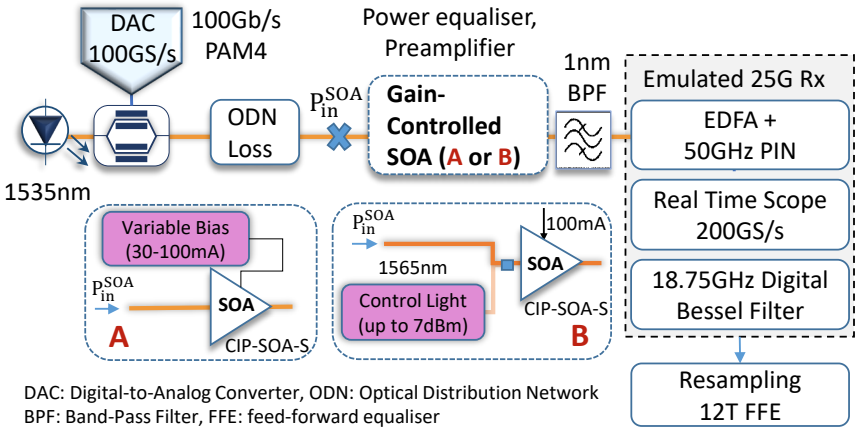


Figure 4.1: Experimental setup emulating PAM4 PON upstream back-to-back transmission using ideal transmitter and receiver to study the two SOA gain control schemes A and B.

4.2 Continuous Mode Analysis with an Ideal Receiver

The effectiveness of the proposed equalisation techniques is first evaluated under continuous-mode back-to-back (B2B) transmission, using an emulated low-cost 25G-class receiver. In this configuration, any performance degradation arises solely from SOA-related impairments and receiver bandwidth limitations, allowing a clear assessment of the intrinsic impact of the equalisation schemes. This analysis therefore provides a reference benchmark for the best achievable performance of the proposed SOA-based techniques before extending the study to burst-mode operation.

4.2.1 Experimental Setup

The performance of the proposed SOA-based power equalisation schemes is validated using a B2B transmission setup, as shown in Figure 4.1. A 50 Gbaud PAM4 electrical signal is generated by a DAC, with linear precompensation applied to mitigate transmitter bandwidth limitations. The signal is modulated onto the optical carrier using a Mach–Zehnder modulator (MZM) driven by the differential outputs of the DAC. The optical signal has an extinction ratio of 6 dB and is subsequently boosted using an EDFA to provide sufficient launch power. The overall transmitter architecture and operating parameters are chosen to emulate a typical 50G-PON transmitter compliant with current standard specifications.

The optical distribution network is emulated by varying the SOA input power,

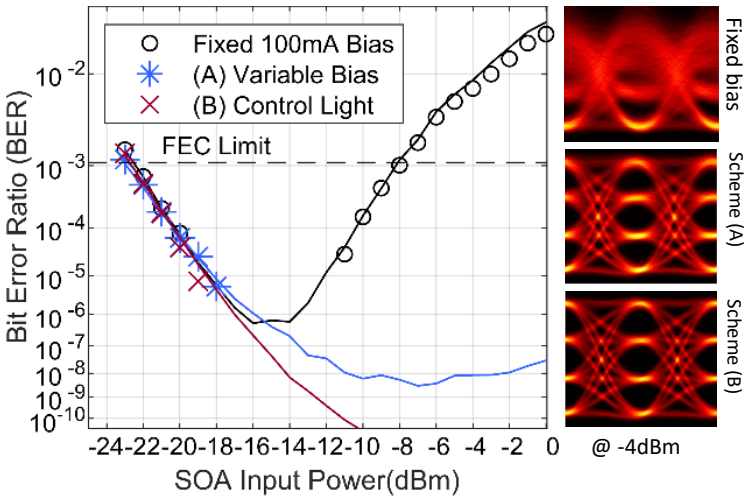


Figure 4.2: BER performance versus SOA input power for the three modes of SOA operation: fixed SOA bias with no power equalisation and the two SOA gain control schemes to maintain a constant output power of -2 dBm.

$P_{\text{in}}^{\text{SOA}}$, over a range from –24 dBm to 0 dBm, representing the expected dynamic range of upstream signals in a high-speed PON.

At the receiver side, an SOA acts as a preamplifier with integrated power equalisation functionality. Two gain-control approaches are investigated: Scheme A (variable bias current) and Scheme B (control light injection). In both cases, the SOA output power is kept constant at –2 dBm. The amplified signal is then passed to a low-cost 25G-class receiver, which is emulated with an 18.75 GHz digital Bessel filter, representative of devices specified in the ITU-T G.9804.3 standard for next-generation PON systems.

This configuration enables direct assessment of the equalisation schemes under realistic receiver constraints, while isolating SOA-induced impairments and bandwidth limitations.

4.2.2 Results and Discussions

Figure 4.2 shows that the SOA nonlinearity results in a V-shaped performance curve supporting only 15 dB DR. By applying equalisation techniques, the system achieves a BER at 1×10^{-3} across a 23 dB input power range, surpassing the PON DR performance target. The stochastic BER is estimated assuming Gaussian distribution to compare the two techniques at low error rates. As shown in the previous chapter, both schemes reduce gain at high input powers and prevent the SOA from operating in the saturation regime. Scheme B performs better,

exhibiting negligible patterning, as evident from the eye diagrams. While both techniques provide a large DR, control light injection outperforms variable bias at high input powers, making scheme B better suited for higher order modulation formats that require high SNR. Equalising the packet powers in the optical domain instead of electrical, as in the BM-TIA case, provides two advantages – (1) high dynamic range operation without any bandwidth limitation from the SOA and (2) the signal does not experience SOA gain saturation effects and is free from non-linear distortions avoiding the need for complex DSP.

4.3 Realistic Condition: Burst-Mode Analysis

While the previous section demonstrates the effectiveness of the SOA-based power-equalisation schemes in continuous-mode, those results are obtained in a B2B configuration using an ideal receiver (EDFA + 50GHz PD) without a TIA and therefore do not capture the constraints of practical operation. In real PONs, upstream traffic consists of short packets from multiple ONUs, each arriving at the OLT in assigned time slots and separated only by short guard times, rather than forming a continuous stream. These bursts also exhibit packet-to-packet power variations of up to 20.5 dB due to differential loss between ONUs. Under such conditions, the receiver must rapidly re-acquire each packet, and the SOA must transition quickly between operating points without introducing gain transients, saturation-induced distortions, or patterning effects. Burst-mode analysis is therefore critical to confirm that the proposed equalisation techniques maintain stable gain, preserve signal integrity during fast power transitions, and reliably support packet-level reception under realistic upstream conditions.

In this section, the packet structure employed in the experiments is first described, highlighting the fields required for synchronisation, equalisation, and payload transmission. The corresponding experimental setup is then presented, followed by results and discussion that assess the effectiveness of the SOA-based equalisation schemes under realistic burst-mode conditions.

4.3.1 Allocation of the Physical Layer Overhead Time

The burst-mode packet format employed in this work follows the principles of the ITU-T G.9804.3 50G-PON standard, with adaptations for 100 Gb/s PAM4 experimental validation. The structure of the packet is shown in Figure 4.3.

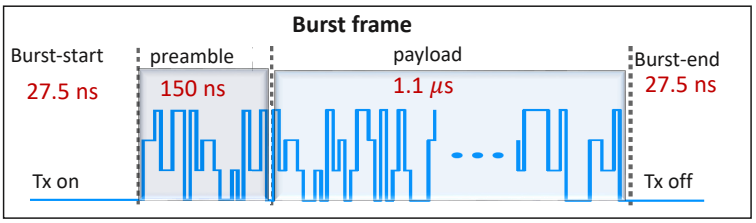


Figure 4.3: Logical structure of the burst frame.

Each packet contains four fields. The start-of-burst (SoB) sequence consists of a 1,375-symbol period (27.5 ns) with no user data transmission and is used to trigger the transmitter and indicate the beginning of a burst at the OLT. The preamble then follows, with 7,500 symbols (150 ns), allowing the receiver to achieve synchronisation, train the equaliser, and provide sufficient time for SOA gain control to stabilise. The payload field, lasting 1.10 μs, carries the modulated data, implemented as 50 Gbaud PAM4. Pseudo-random bit sequences (PRBS15 for loud bursts and PRBS13 for soft bursts) are used to emulate realistic dynamic range conditions. Finally, the end-of-burst (EoB) sequence consists of the same 1,375-symbol, no-data period as the SoB and is appended to disable the transmitter and clearly separate consecutive packets.

Between successive packets, a guard time of 55 ns is inserted to accommodate transmitter switching and ensure reliable separation. The resulting total overhead amounts to 10,250 symbols, which is consistent with the allocation recommended in the latest PON standards.

This packet structure provides sufficient overhead for synchronisation and gain adaptation while maximising payload efficiency. In particular, the impact of guard time duration on system performance is analysed experimentally in the following subsection.

Guard-Time Duration

In a real implementation, the inter-burst guard time directly impacts the system in two critical ways:

SOA gain switching dynamic: When SOAs are operated in burst mode, finite carrier recovery times following burst extinction can lead to residual gain and amplified spontaneous emission at low power levels. To avoid transient-induced noise leakage into subsequent packets, these effects must be considered to ensure proper settling of the burst envelopes generated by the ONU booster SOAs

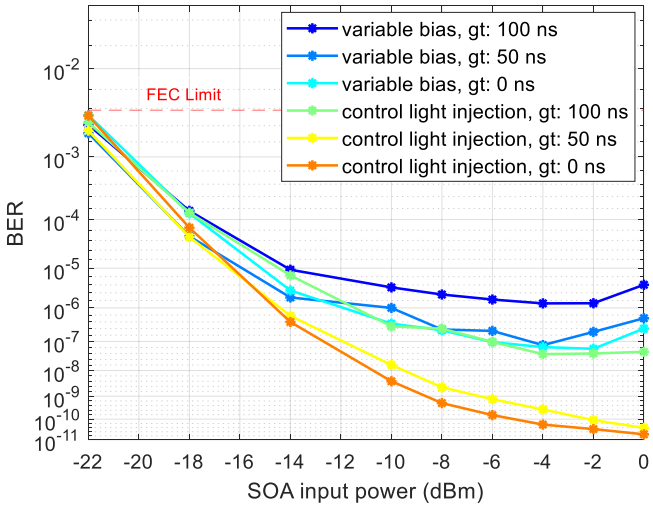


Figure 4.4: Effect of inserted inter-packet idle intervals (guard-time emulation) on the performance of a continuous-wave 100 Gb/s PAM4 transmission using the experimental setup shown in Figure 4.1. The receiver input power is fixed at -2 dBm using the equalisation techniques.

and the OLT preamplifier SOA used in this work. However, they do not represent the dominant constraint in determining the guard time.

System throughput and scalability: From a network and system perspective, the upstream guard time should be minimised to maximise bandwidth efficiency, reduce latency, and support scalable operation with a large number of ONUs and short upstream bursts. However, the guard time must remain sufficiently long to accommodate residual timing uncertainty from ranging errors and clock drift, allow for ONU transmitter turn-on and turn-off transients, and ensure reliable settling of the OLT burst-mode receiver front end, including SOAs, burst-mode TIAs, and clock-and-data recovery circuits, thereby preventing burst overlap and ensuring error-free reception. In our experiment, we adopt a 55 ns guard time, which reflects a practical trade-off. This value is in line with industry recommendations, including the 51.4 ns overhead allocated for guard time in 50G-PON systems.

While the SOA itself can switch quickly, the selected 55 ns guard time ensures reliable separation between bursts in our setup, limits inter-burst interference due to slow transients, and remains aligned with realistic system constraints. The experimental setup shown in Figure 4.1 is used to evaluate the impact of emulated inter-burst guard time on a 100 Gb/s PAM4 upstream transmission with continuous-wave optical operation. While the transmitter configuration remains unchanged, a photoreceiver with integrated adjustable conversion gain (Thorlabs

RXM42AF) is used in place of an ideal receiver to emulate more realistic operating conditions. Equalisation techniques are employed to maintain the optical input power to the receiver at a constant level of -2 dBm. Figure 4.4, which examines system performance under different off-state durations between packets (0 ns, 50 ns, and 100 ns) in continuous mode, further demonstrates that including a 55 ns guard time between packets does not cause significant degradation. Increasing the off-state duration to 100 ns does not yield further performance improvement and can instead lead to a slight degradation. This behaviour indicates that, beyond the minimum separation required for reliable burst isolation, the dominant penalty is governed by burst-to-burst settling effects in the end-to-end electrical and optical front ends. The transmitter and receiver used in this experiment are not explicitly designed or optimised for burst-mode operation, and therefore exhibit burst-to-burst nonideal behaviour when extended idle intervals are introduced.

4.3.2 Experimental Setup

The experimental testbed used to evaluate the proposed SOA-based equalisation schemes in burst-mode operation is shown in Figure 4.5. Two ONUs are emulated using independent tuneable lasers configured to adjacent C-band ITU-T grid channels, spaced by 150 GHz at 195.3 THz and 195.15 THz, corresponding to wavelengths of 1535.036 nm (ONU1) and 1536.216 nm (ONU2). The choice to use separate wavelengths is because of both experimental and architectural considerations. First, the objective is to demonstrate a soft–loud packet scenario, in which successive packets arrive with different optical power levels. Assigning distinct wavelengths to each ONU allows different levels of optical attenuation to be applied in a controlled manner. Second, ONUs may be configured to operate at different wavelengths within the designated upstream band. Such wavelength diversity can arise from laser tolerances or wavelength assignment strategies, while only a single ONU transmits at any given time in TDM-PON operation. Consequently, the adopted experimental approach reflects this characteristic of practical systems while enabling controlled power variation between packets. Each laser output is modulated by an MZM driven by a differential-output DAC. The DAC generates a 50 Gbaud PAM4 burst signal with an extinction ratio of 6 dB, while linear pre-compensation is applied to mitigate bandwidth limitations up to 40 GHz.

To carve burst packets with the format described in the previous subsection,

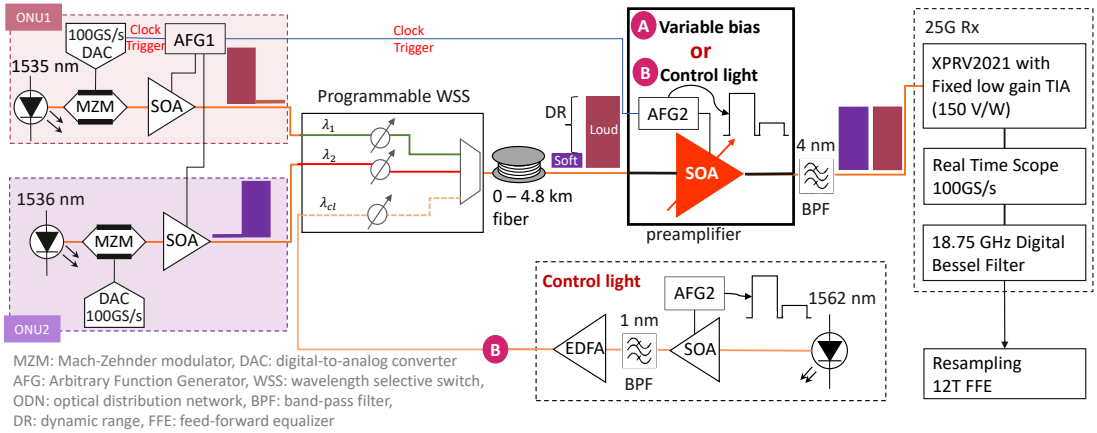


Figure 4.5: Experimental setup for high-speed burst-mode traffic analysis with SOA preamplified receiver performing optical equalisation using two schemes, (A) variable bias, and (B) control light injection.

booster SOAs (*CIP-SOA-L*) are placed after the modulators. These devices, driven by an AFG, suppress the optical output during the off-state between bursts. By synchronising the AFGs, time-division multiple access is emulated such that the ONUs transmit alternating bursts, separated by a 55 ns guard time in accordance with the 50G-PON standard.

A wavelength-selective switch (WSS) is employed to dynamically control attenuation, combine the control light with the signal, suppress out-of-band ASE, and emulate packet power variations. While not part of a practical PON deployment, the WSS provides flexibility in the laboratory environment. Due to its operational range, the control light wavelength is set to 1562 nm instead of the 1575 nm used during device characterisation.

The optical distribution network is further emulated by combining programmable WSS attenuation (up to 15 dB) with fixed attenuators, giving a total path loss of 24 dB. Chromatic dispersion is introduced using standard single-mode fibre with a coefficient of 16.16 ps/(nm·km) at 1535 nm, corresponding to 77.5 ps/nm in total — a value higher than expected for 20 km O-band transmission, but aligned with the 50G-PON standard and suitable for worst-case evaluation.

At the receiver, a *CIP-SOA-S* serves as the preamplifier with adaptive gain control. Two equalisation schemes are investigated: (A) variable bias current and (B) control light injection. In both cases, the SOA output is regulated to –2 dBm per packet. The AFG is programmed with pre-calibrated waveforms derived from offline SOA transfer measurements across a 20 dB input range, mapping burst amplitudes to either SOA bias current (Scheme A) or control light power (Scheme

B). Synchronisation between the DAC and AFG ensures that the equalisation waveform is applied to the correct burst in real time.

The SOA output is filtered with a 4 nm optical band-pass filter to suppress ASE noise before being detected by a 50 GHz photoreceiver with a fixed 46 dBΩ TIA. This configuration emulates an optically preamplified receiver with a low-gain TIA, consistent with the objective of simplifying the burst-mode front-end. The detected waveform is captured on a 100 GSa/s real-time oscilloscope with 70 GHz bandwidth, after which an 18.75 GHz digital Bessel filter is applied to emulate a cost-effective 25G-class receiver.

Finally, DSP processing is deliberately kept simple. A 12-tap FFE is trained using the preamble sequence, and BER analysis is carried out exclusively on the payload field. Each burst is analysed separately to assess the effectiveness of the equalisation schemes under dynamic input conditions.

4.3.3 Results and Discussions

In this study, the system sensitivity and achievable dynamic range are assessed using the SD-FEC limit of 1×10^{-2} BER. BER is calculated using the counting method, and to compare the two techniques at low error rates, the stochastic BER is also estimated assuming a Gaussian distribution.

The BER is first measured separately for the burst payloads of ONU1 and ONU2, beginning with the loud-loud scenario where no dynamic range is introduced. This initial measurement verifies transmitter quality and assesses whether SOA carving introduces any impairments. With the proposed gain control schemes A and B, the SOA output power is kept constant at -2 dBm. Figure 4.6 shows that bursts from ONU1 and ONU2 achieve comparable results. At low input powers, signal quality is primarily limited by OSNR degradation due to ASE, as discussed in the previous chapter. At high input powers, the dominant impairment arises from SOA gain saturation, which in our scheme is mitigated by applying gain equalisation techniques that maintain the SOA in its linear regime.

The sensitivity is measured at approximately –24 dBm for both schemes. Although, in control light scheme at least a 1 dB receiver sensitivity penalty should be considered due to the use of a combiner in its structure. Despite this penalty, both schemes still meet the sensitivity requirement outlined in the latest standard. Moreover, the burst-mode results align with the continuous-mode analysis performed on ONU1, confirming the absence of any SOA gain transition effects.

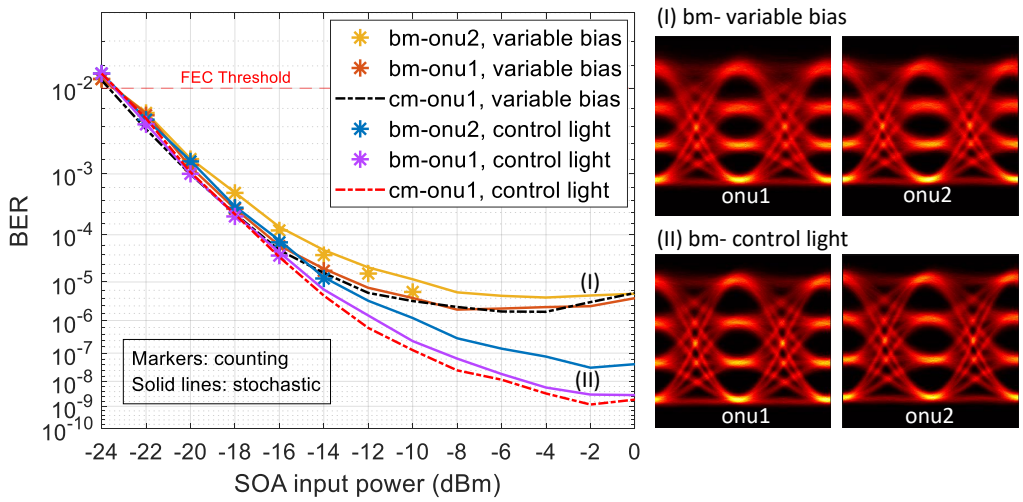


Figure 4.6: Burst-mode (loud (ONU1), and soft (ONU2)) and continuous mode (ONU1) BER measurements using SOA-based equalisation techniques in a 100 Gb/s back-to-back PAM4 transmission. Eye patterns are provided for both ONU1 and ONU2 at an input power of -2 dBm to the SOA.

The variation in performance between ONU1 and ONU2 in the control light scheme is attributed to a lower achievable SNR for ONU2 compared to ONU1. Although the gain reduction required at high input powers is achieved by reducing the carrier inversion in the SOA, which increases the noise figure, the impact on BER is minimal and the overall performance is improved, extending the dynamic range to 24 dB. Additionally, the eye patterns reported for both schemes and both ONUs confirm that even at the high input power into the SOA of -2 dBm, the degradation effect due to gain saturation is negligible, exhibiting minimal signs of patterning effect. To isolate the SOA's nonlinearity at high input powers, we avoided using a fixed 100 mA SOA bias in our measurements, as this configuration can lead to receiver overload and TIA nonlinearity, complicating interpretation. Instead, this scenario was analysed in the previous section, where we assumed an ideal receiver. That analysis revealed a V-shaped performance curve, with dynamic range limited to 15 dB due to the fixed bias operation.

The dynamic range of the soft-loud packet sequence is then gradually increased while maintaining the power of the soft (ONU2) burst at its sensitivity level. The power of the loud (ONU1) burst is adjusted by modifying the attenuation profile of the wavelength-selective switch.

Figure 4.7.(a) presents the burst signal traces captured immediately after the SOA preamplifier using a sampling oscilloscope. The top graph shows the signal traces before equalisation, while the middle and bottom graphs display the results after

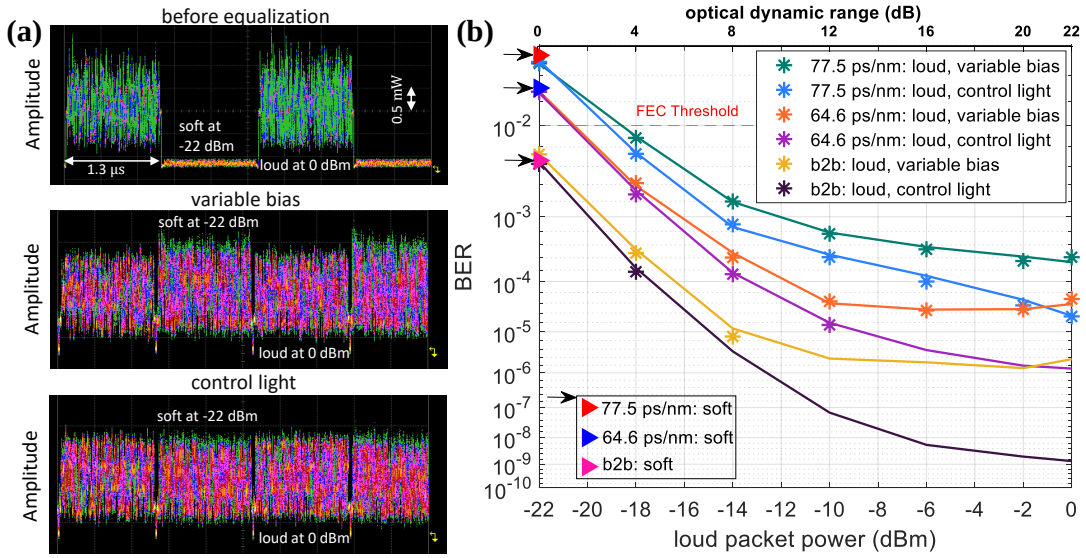


Figure 4.7: (a) Signal traces of burst signals before and after equalisation with two techniques, captured after the SOA preamplifier. (b) BER measurements for 100 Gb/s burst-mode PAM4 transmission using SOA-based equalisation at various dispersion levels. Markers indicate counting errors, and solid lines represent stochastic errors.

applying variable bias and control light equalisation, respectively. As shown in the figure, the proposed methods effectively compensate for large power variations, with no observable signal distortion caused by the SOA's transient response.

As shown in Figure 4.7.(b), in a B2B configuration, the BER of the loud burst measured for DRs ranging from 0 dB to 22 dB floors at approximately 10^{-6} using the variable bias equalisation method, and at around 10^{-9} when injecting a control light. This difference arises from the improved performance of the SOA in the signal saturation regime and higher OSNR of the SOA in the control light scheme. However, as dispersion-induced distortions increase, the difference between the two equalisation methods becomes less significant. This is likely because the BER is primarily constrained by residual ISI caused by chromatic dispersion, diminishing the relative impact of the improved OSNR and higher saturation power provided by the control light approach. The sensitivity penalty observed for fibre lengths of 4 km and 4.8 km, compared to the B2B case, is attributed to residual chromatic dispersion, which the 12-tap FFE equaliser could not fully compensate for, leading to a degradation of system performance.

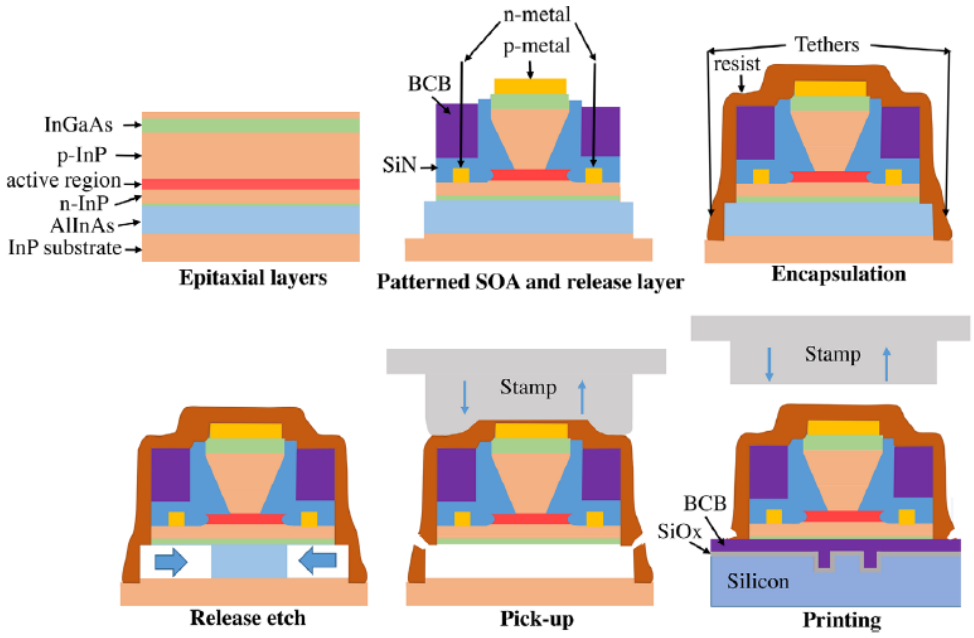


Figure 4.8: Overview of the micro transfer printing process for integrating prefabricated III–V devices onto silicon photonic circuits [30].

4.4 Integration: Transfer Printing SOA

This section demonstrates that advanced SOA-based power equalisation is not limited to commercial discrete devices but can also be realised on an integration-friendly platform. The experimental validation of TP-SOAs in this section highlights their potential as a scalable solution for future PON systems, where compactness, cost-effectiveness, and manufacturability are as critical as performance.

4.4.1 Micro-Transfer Printing Technology

Micro transfer printing has emerged as a powerful technique for the heterogeneous integration of III–V optoelectronic devices onto silicon photonic integrated circuits. The method was further developed and formalised through advances in elastomer stamp-based deterministic assembly, which demonstrated that microscopic semiconductor devices can be released from their native substrates and accurately placed onto foreign platforms with high placement fidelity [109]. Compared with monolithic III–V growth on silicon, which remains challenged by crystal defects and thermal mismatch [110], micro transfer printing enables the use of high-quality III–V epitaxial material while maintaining compatibility with established CMOS-derived silicon photonics processes [111].

In a typical micro transfer printing process, the III–V devices are first fabricated

on their native InP wafer. The active epitaxial layers are grown above a selectively etchable release layer, and the full device structure, including the mesa and the electrical contacts, is defined using standard III–V processing. A schematic overview of the key steps in this process is provided in Figure 4.8, which illustrates the sequence of device release, elastomer stamp pick up and subsequent placement onto the silicon photonic circuit. The release layer is then removed in a controlled etching step, leaving each device mechanically supported by thin tethers. At this stage, the devices have been completely processed and can be electrically tested on the III–V wafer before integration, which improves overall yield and allows selection of only fully functional components [112]. A soft polydimethylsiloxane (PDMS) stamp is used to retrieve the released devices by means of a laminating and peeling motion that breaks the supporting tethers. The same stamp is then aligned to the silicon photonic wafer, and the devices are placed onto the prepared bonding regions using a controlled contact and release sequence. Placement accuracy from sub-micron to a few microns (process-dependent) can be achieved, and the method supports both single device placement and parallel transfer of large arrays. Such placement precision is sufficient for III–V devices that use adiabatic taper transitions designed for relaxed alignment tolerance to interface with the underlying silicon waveguides [113].

One of the key strengths of micro transfer printing is its ability to integrate devices that originate from different III–V epitaxial structures onto the same silicon photonic platform. This stands in contrast to die to wafer bonding, where all bonded dies typically share a common epitaxial design and where modifications to the silicon photonics back end are often required [114], [115]. Micro transfer printing largely avoids these constraints and minimises disruption to the standard silicon photonics process flow. Only minimal post processing is needed after printing, usually limited to removing temporary encapsulation material, planarizing the bonding layer, opening contact vias to the printed devices and depositing the final metallisation.

Transfer printed III–V on silicon semiconductor optical amplifiers, for example, have demonstrated small signal gain values exceeding 20 dB, which satisfies the gain requirement for a preamplifier and provides sufficient power budget. They also exhibit high saturation powers on the order of $\approx$10 mW (and in some reports tens of mW), depending on the design, confinement factor, and measurement point (on-chip vs off-chip) [30], [116], [117], which extends the linear region of the SOA and offers an increase in the achievable dynamic range when used as a preamplifier.

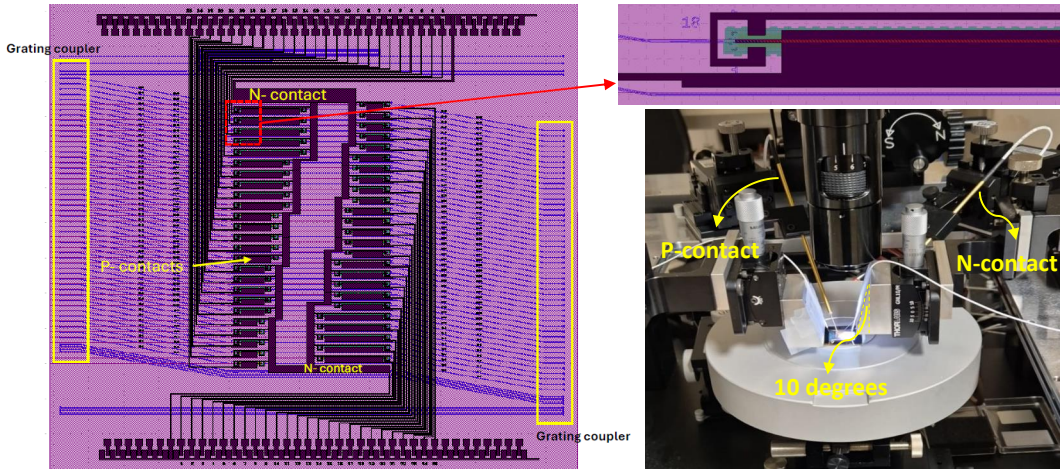


Figure 4.9: TP-SOA chip layout and probe station connection.

4.4.2 Under Test TP-SOA

Figure 4.9 shows the TP-SOA chip layout fabricated by the III-V Materials and Devices Group at Tyndall National Institute. The chip hosts multiple SOAs with lengths between 1.0 mm and 1.5 mm, designed to provide a range of gain characteristics.

Figure 4.9 also presents the probe station used for characterisation, highlighting the electrical probing contacts and fibre coupling arrangement. The fibres are aligned at an angle of approximately 10° to the grating couplers in order to minimise back-reflections. This coupling geometry is typical for grating-coupled devices but introduces an additional coupling loss of about 5 dB, which impacts the effective system-level gain. Nevertheless, for consistency, all reported sensitivity and BER measurements are referenced directly at the chip facet, excluding this coupling penalty.

Based on the characterisation of several devices, an SOA with a 1 mm length and a maximum small signal gain of 17 dB is selected to replace the *CIP-SOA-S* in the experimental setup shown in Figure 4.1. The spectral measurements confirm that the chosen device does not exhibit parasitic lasing, as shown in Figure 4.10. Parasitic lasing occurs when internal reflections together with high gain cause the SOA to behave like an unintended laser cavity, which results in narrow peaks at wavelengths that are not present in the input signal. To verify this, spectra are recorded at both high and low input powers and for several bias currents. The spectra corresponding to the conditions where parasitic lasing is most likely to occur are included in the figure. These are the cases with high bias and low

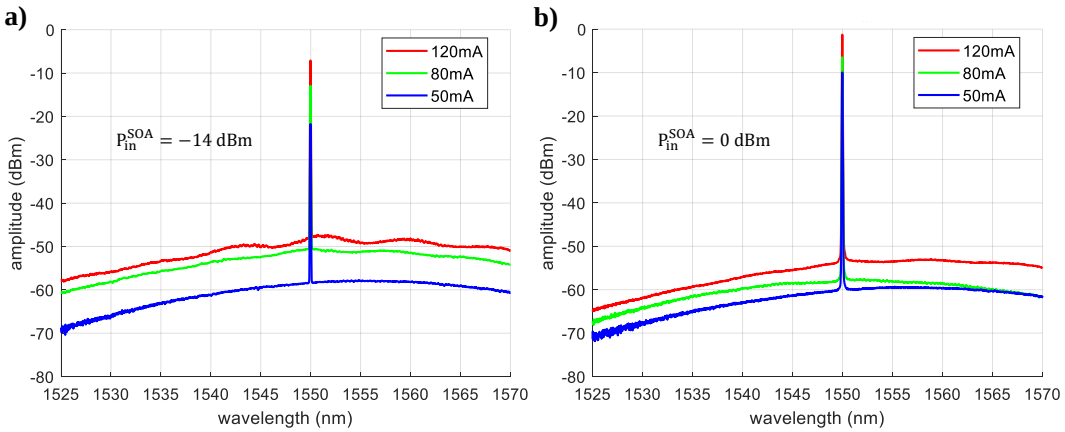


Figure 4.10: Measured spectra of the TP SOA at (a) low and (b) high input powers for multiple bias currents, used to assess potential parasitic lasing.

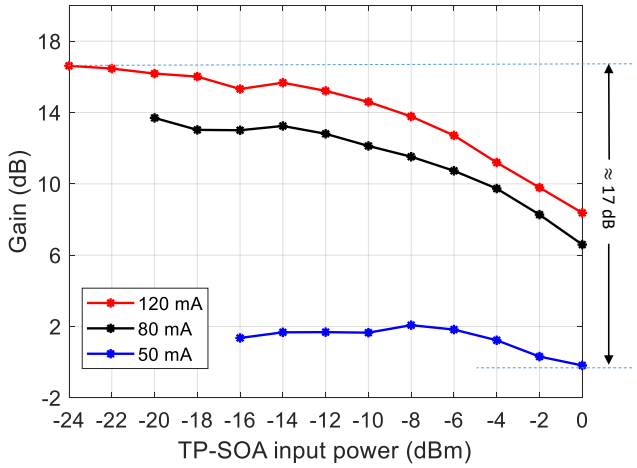


Figure 4.11: Measured TP-SOA gain as a function of input power for several bias currents, illustrating a gain variation of approximately 17 dB.

input power, and with high bias under strong saturation.

The gain characteristics of the selected device, measured at bias currents of 120 mA, 80 mA, and 50 mA, are presented in Figure 4.11. As expected, reducing the bias current decreases the small signal gain by about 17 dB and increases the linear operating range of the amplifier.

Table 4.1: TP-SOA (excluding coupling loss) and *CIP-SOA-S* characteristics.

Amplifier	$\mathbf{G_0}$ (dB) @ 100 mA	**NF** (dB) @ -30 dBm	$\mathbf{P}_{\text{in,sat}}$ (dBm)
CIP-SOA-S	20	6	-8.8
TP-SOA	≈16	5.8	-8

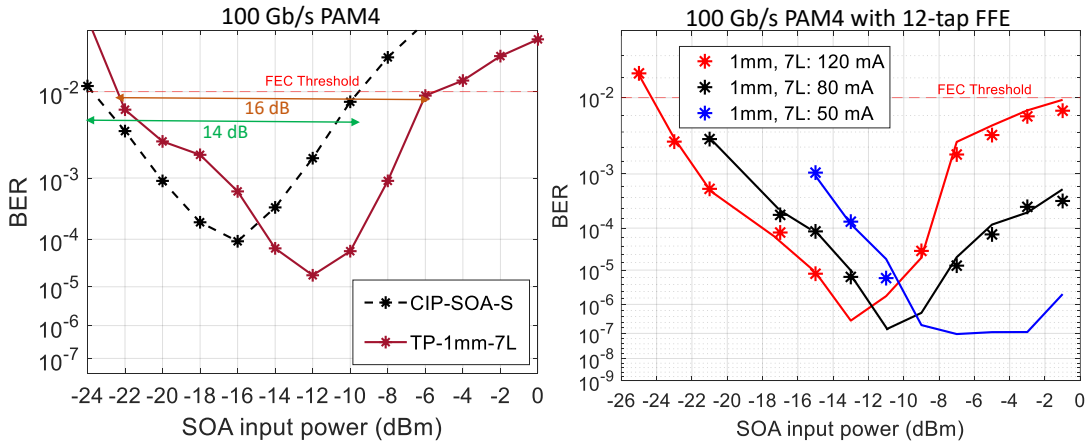


Figure 4.12: (a) BER comparison of TP-SOA and *CIP-SOA-S* at a fixed bias current of 100 mA for 100 Gb/s PAM4 transmission over a wide dynamic range, and (b) bias reduction impact on the BER performance improvement at high input powers.

Table 4.1 summarises the measured device parameters, including maximum gain, saturation input power, and noise figure, and provides a direct comparison between the TP-SOA and the commercial *CIP-SOA-S*. These values represent the intrinsic device measurements and therefore do not include the 5 dB coupling loss as mentioned earlier. Although the small signal gain of the TP-SOA is lower, its slightly lower noise figure and higher saturation input power provide improved system-level characteristics, resulting in comparable sensitivity and an extended dynamic range.

4.4.3 System-Level Test

Figure 4.12.(a) shows the BER performance of 100 Gb/s PAM4 transmission using the TP-SOA as a preamplifier, compared against the commercial *CIP-SOA-S* device. The experimental setup corresponds to the continuous-mode configuration described in Section 4.2, with the signal wavelength fixed at 1550 nm. A sensitivity shift of approximately 1 dB is observed relative to the *CIP-SOA-S*, primarily due to the lower gain of the TP-SOA. At higher input powers, the TP-SOA demonstrates a higher saturation input power than the commercial device, thereby entering saturation later and extending the dynamic range by about 2 dB.

Figure 4.12.(b) presents the BER results obtained at multiple SOA bias currents. A 12-tap FFE is applied at the receiver to mitigate bandwidth limitations. As expected, reducing the bias current shifts the BER curves and increases the dynamic range. These results confirm that the variable bias technique is equally

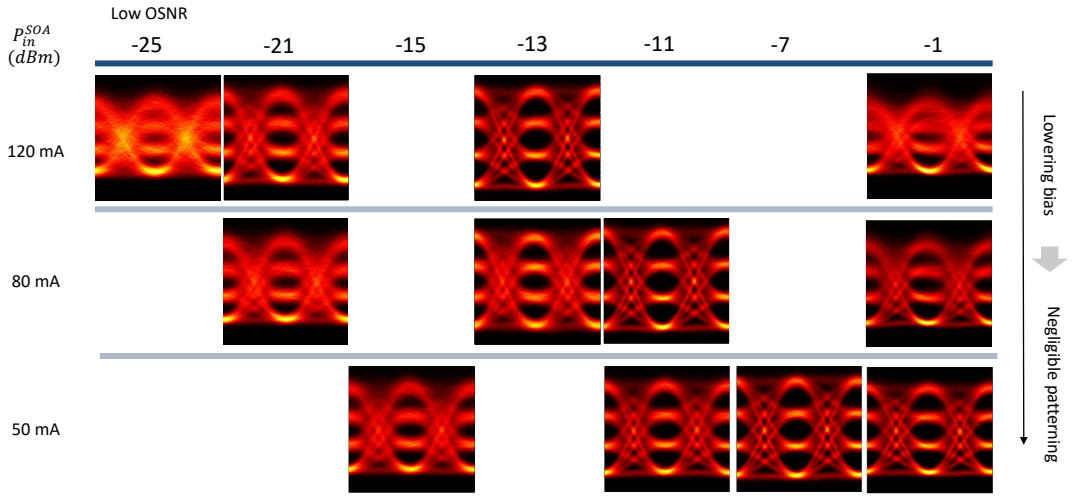


Figure 4.13: Eye diagrams at increasing input powers for multiple bias currents.

applicable to TP-SOAs, enabling burst-packet equalisation.

Figure 4.13 illustrates the eye diagrams of the received 100 Gb/s PAM4 signal at increasing SOA input powers for three different TP-SOA bias currents: 120 mA, 80 mA, and 50 mA. At a high bias current of 120 mA, the eye quality degrades at low input powers due to reduced OSNR, while at higher input powers pronounced patterning effects emerge as the SOA enters saturation. By contrast, lowering the bias current progressively suppresses pattern-dependent distortion. At 50 mA bias, the eye diagrams exhibit negligible signs of patterning even at high input powers, confirming that bias reduction effectively extends the SOA's linear operating regime.

Together, these findings highlight the potential of TP-SOAs not only as integration-friendly alternatives to discrete commercial SOAs but also as viable candidates for implementing adaptive optical equalisation in future PON architectures.

4.5 Increasing Capacity: PAM8 Signal Quality

Higher-order modulation formats such as PAM8 demand significantly higher SNR and exhibit increased sensitivity to nonlinear distortion. This section evaluates how far the IM/DD data rate can be extended when operating in such a linearity-critical regime and examines the effectiveness of SOA-based power-equalisation techniques under these conditions. Extending the PAM4 analysis, system performance under PAM8 modulation is evaluated, where SOA patterning effects and noise figure impose more stringent limitations. Since the control light injection

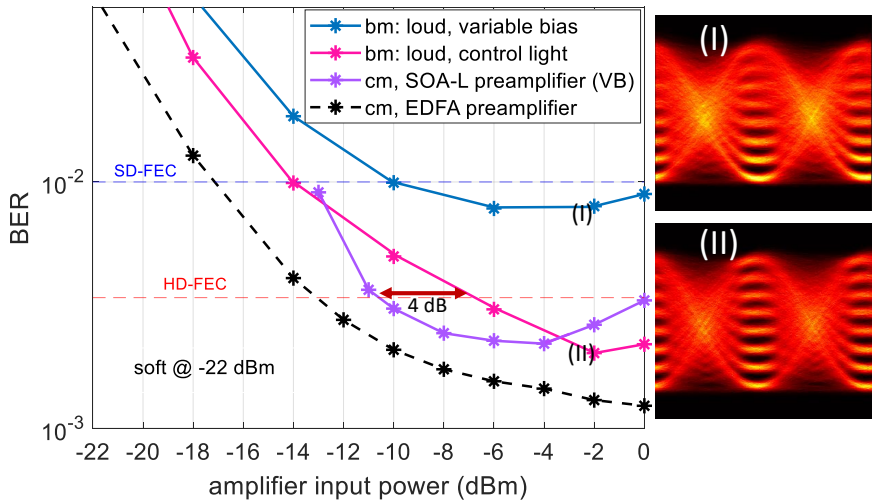


Figure 4.14: 150 Gb/s PAM8 burst-mode back-to-back transmission employing SOA-based power equalisation is analysed. Continuous-mode operation using a linear SOA is included for comparison, and EDFA preamplification serves as an ideal reference case.

method maintains higher OSNR and provides stronger suppression of patterning effects compared with the variable bias technique, improved performance is anticipated when applying this approach to PAM8 transmission.

The experimental setup used for the 50 Gbaud burst-mode PAM4 measurements (Figure 4.5) is reused for this analysis, with the DAC configured to generate a 50 Gbaud PAM8 burst signal.

4.5.1 Experimental Results

Figure 4.14 presents the BER performance of the loud packet as a function of its dynamic range relative to the soft packet, which is fixed at an input power of -22 dBm. Measurements are conducted in a 150 Gb/s PAM8 burst-mode B2B configuration using the proposed equalisation techniques. Continuous-mode operation with an EDFA preamplifier is included as an ideal reference. Without optical preamplification, the receiver sensitivity is -6 dBm at the HD-FEC threshold for 50 Gbaud PAM8.

As shown in the figure, the variable bias method fails to mitigate the SOA nonlinearities at this symbol rate and therefore degrades the receiver sensitivity, while the control-light equalisation provides only a marginal improvement of approximately 1 dB. The better performance observed with control light injection is primarily attributed to improved SOA operation in the signal saturation regime

and a higher OSNR. This behaviour is further evidenced by the corresponding eye diagrams. However, the limited receiver sensitivity indicates that the improvement remains insufficient for practical 50 Gbaud PAM8 PON operation.

To further investigate sensitivity enhancement at 50 Gbaud PAM8, the SOA is replaced with a linear model. As illustrated, the linear SOA (*CIP-SOA-L*), featuring a higher saturation power and enabling packet power equalisation via variable bias control, achieves a 4 dB sensitivity improvement compared to the *CIP-SOA-S*, which has a lower saturation power and employs control-light injection. At the SD-FEC threshold, however, the latter provides better sensitivity due to SOA's higher gain but still fails to meet the required power budget. Method B equalisation is not evaluated for the linear SOA, as it requires control light injection at wavelengths beyond the capabilities of the experimental setup. Further sensitivity improvement is limited by the relatively low gain (14 dB) of the *CIP-SOA-L*.

The EDFA-based reference results further indicate that simply increasing the modulation order, for example from PAM4 to PAM8, does not provide a viable path to scaling the data rate in IM/DD PON systems. At 50 Gbaud PAM8, neither the required power budget nor the dynamic range can be achieved using the proposed SOA-based equalisation techniques. These results highlight the fundamental limitations of IM/DD approaches at higher baud rates and modulation orders, suggesting that a transition toward coherent PON architectures represents the most practical and future-proof solution for ultra-high-speed next-generation access networks.

4.6 Summary

This chapter experimentally validates SOA-based optical power equalisation for 50 Gbaud IM/DD PONs. Continuous-mode tests confirm that both variable bias and control light injection effectively adapt SOA gain, suppress nonlinear patterning, and extend dynamic range to 23 dB while remaining compatible with low-cost 25G-class receivers. These results are published in the *CLEO/Europe conference* [A1].

Burst-mode transmission is then investigated using two emulated ONUs transmitting to an SOA-preamplified receiver equipped with a fixed 46 dBΩ TIA. The experiments include up to 77.5 ps/nm chromatic dispersion, representing a worst-case condition. Results demonstrate that the proposed equalisation techniques

successfully regulate a 24 dB input dynamic range and overcome SOA nonlinearities. With the packets already equalised in the optical domain, only a simple 12-tap FFE is required to compensate for dispersion and receiver bandwidth limitations, eliminating the need for a BM-TIA to handle large dynamic range. The results of this study have been published in *Optics Express* [A2].

Optical equalisation using TP-SOA is also evaluated in a high-speed 100 Gb/s upstream transmission to demonstrate its potential for integration into cost-effective receivers. Despite lower maximum gain compared to the commercial *CIP-SOA-S*, without considering the coupling loss, TP-SOA offers slightly lower noise figure and higher saturation power, achieving comparable sensitivity and improved dynamic range. These results form part of an upcoming collaborative journal publication.

Finally, 50 Gbaud PAM8 transmission is examined. Neither the required power budget nor the dynamic range is met, even with an EDFA reference, highlighting the limitations of IM/DD at higher modulation orders. These limitations motivate the transition toward coherent PON architectures, the results of which are presented in the next chapter.

Chapter 5

SOA-based Power equalisation over a 400 Gb/s Coherent PON

This chapter investigates SOA-based optical power equalisation in coherent PON at line rates up to 400 Gb/s. While such equalisation has been explored at lower speeds, we introduce a new architecture that motivates SOA use by maintaining wavelength alignment between ONU and LO. Using a variable-bias scheme, packet powers are equalised in the optical domain, mitigating SOA saturation and easing burst-mode receiver requirements, thereby reducing the need for high-gain, high-dynamic-range BM-TIAs.

Although IM/DD remains in use for its simplicity and cost effectiveness, it is increasingly unable to support the evolution of future PONs. The ITU-T G.9804 standard for 50G-PON specifies a stringent 29 dB loss budget which becomes difficult to meet as data rates scale to 100 Gb/s per wavelength and beyond. IM/DD transmission at such rates faces significant challenges from CD, SNR degradation, and low cost component bandwidth constraints. Although O-band operation reduces CD, a key additional limitation stems from BM-TIAs, which may struggle to meet the necessary linearity, bandwidth, and dynamic range.

Coherent optical technology provides a stronger alternative to IM/DD by overcoming key limitations in power budget and spectral efficiency. It offers higher receiver sensitivity, built-in chromatic dispersion compensation, and supports advanced modulation formats, making it well-suited for scaling PONs to 100 Gb/s

per wavelength and beyond. However, practical deployment requires addressing key challenges such as cost and burst-mode compatibility.

This chapter proposes a new architecture for coherent PON which uses a frequency comb source at the OLT allowing the use of low-cost Distributed Feedback (DFB) lasers in ONUs while addressing the challenge of maintaining wavelength alignment between the ONU and LO. Simultaneously, performs packet equalisation in the optical domain using an SOA reducing the need for high-dynamic-range BM-TIAs. The system model is analysed in detail, including an evaluation of the LO power range when comb-source losses are considered, based on values reported in prior works. Although the experimental setup does not employ a real comb source as the LO, it serves as a proof-of-concept demonstration of the effectiveness of SOA-based optical power equalisation in a high-speed coherent PON receiver equipped with a low fixed-gain BM-TIA.

5.1 Functional Overview

Meeting the strict cost targets of an ONU while ensuring emission at a well-defined wavelength remains a significant challenge. DFB lasers represent a cost-effective solution, offering single-mode operation, linewidths on the order of 1 MHz, and maximum output powers around 10 dBm [118], [119], [120]. Nevertheless, their emission wavelength is sensitive to fabrication tolerances and temperature fluctuations, drifting by approximately 0.1 nm/°C [121], [122], [123], [124]. As a result, DFB lasers can exhibit wavelength variations of up to ± 4 nm [60], corresponding to a frequency offset of about 1 THz in the C-band. This poses a critical issue for coherent PONs, where accurate wavelength matching between the signal and LO is required. Different methods have been proposed to address this issue, including injection locking [125] and the use of reflective semiconductor optical amplifiers [126]. Although fast-tuning local oscillators for burst-mode coherent receivers have been demonstrated in [127], producing such lasers at low cost continues to be a major technical obstacle.

A promising alternative is the use of a frequency comb source at the OLT [60], [61], [128], which generates multiple narrow spectral lines. Such a source inherently tolerates the wavelength drift of ONU lasers, provided it remains within the comb's spectral coverage, thereby eliminating the need for active LO tuning.

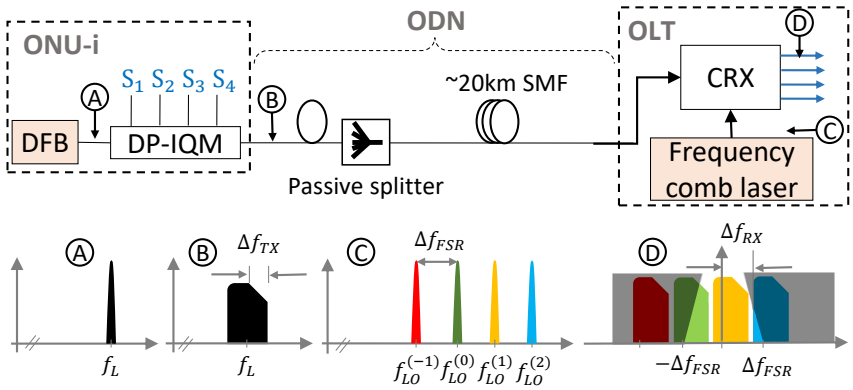


Figure 5.1: Simplified system model of the upstream transmission using a low-cost DFB laser at the ONU and a frequency-comb source at the OLT as the LO [60]. Power spectra at different stages are included.

5.1.1 Frequency Comb Source as Local Oscillator

A frequency comb source is a multi-line optical laser source that generates N_{comb} optical carriers (comb lines) uniformly spaced in frequency by a constant interval Δf_{FSR}, referred to as the free-spectral range (FSR), resulting in an overall optical bandwidth $\Delta f_{\text{comb}} = N_{\text{comb}} \Delta f_{\text{FSR}}$ around the optical centre frequency f_c. The optical frequency of the n-th comb line can therefore be expressed as

$$f_L^{(n)} = f_c + n\Delta f_{\text{FSR}}. \tag{5.1}$$

When such a source is used in coherent systems, the phase evolution of the detected signals depends on the relative phase evolution between the signal and the corresponding comb lines used as local oscillators. If all comb lines share a common phase noise process and differ only by constant, line-dependent phase offsets, the source is referred to as a coherent frequency comb [60].

Figure 5.1 shows a simplified model for an upstream operation. At the ONU, a low-cost DFB laser is used as the upstream transmit laser. Subfigures A and B depict the optical spectrum of the unmodulated DFB laser and the corresponding spectrum at the output of the dual-polarisation I/Q modulator (DP-IQM), respectively. With electrical filters of bandwidth Δf_{TX} applied to the I and Q components, the optical signal bandwidth becomes $\Delta f_{\text{sig}} = 2\Delta f_{\text{TX}}$.

At the OLT, the upstream signal is detected by a coherent receiver (CRX) using a coherent frequency-comb source as the LO, with a comb-line spacing given by the free-spectral range Δf_{FSR} as shown in subfigure C. The spacing between adjacent comb lines must be chosen in accordance with the bandwidth of the transmitted

signal to avoid spectral overlap after detection. To ensure that each comb line maps to a distinct electrical spectrum, the condition $\Delta f_{\text{FSR}} \geq 2\Delta f_{\text{TX}}$ must be satisfied. If the comb spacing is smaller than this limit, spectral components originating from neighbouring comb lines overlap in the electrical domain, resulting in ISI and inter-channel interference that cannot be fully removed by linear signal processing. Accordingly, the comb spacing must be chosen to support the desired symbol rate without spectral overlap.

Subfigure D illustrates the power spectrum of the complex received electrical signal. The shaded regions represent the effect of the low-pass characteristic of the OLT receiver. If the detected signal does not fully fit within the electrical receiver bandwidth Δf_{RX}, spectral clipping occurs, leading to signal distortion and performance penalties. This situation can arise when the receiver bandwidth is limited by hardware constraints or when reduced-bandwidth receiver architectures are employed. Such impairments can be mitigated to some extent by appropriate digital signal processing, for example by using MIMO equalisation, however, a detailed treatment of receiver bandwidth limitations is beyond the scope of this thesis.

Since the effective LO power is determined by the power of the selected comb line, the following analysis estimates the per-line power of the frequency-comb source used as the LO in a 50 Gbaud system, assuming an ONU laser wavelength drift of ± 4 nm. A frequency comb comprising 20 lines with a spacing of 50 GHz spans a total bandwidth of about 1 THz, which is sufficient to cover this drift range and relax the wavelength-stability requirements of low-cost ONU transmitters.

A key practical limitation arises from the fact that the total output power of the comb is distributed among all lines. If the comb delivers a total optical power P_{tot} across N_{comb} lines, then the average per-line power can be approximated as

$$P_{\text{line,avg}} = P_{\text{tot}} - 10\log_{10}(N_{comb}). \tag{5.2}$$

For a 20-line comb, this results in a ~ 13 dB reduction relative to the total power. For example, a comb source with $P_{\text{tot}} = +16$ dBm yields an average line power of roughly $+3$ dBm before additional filtering or splitting losses.

Equally important is the spectral flatness of the comb. Ideally, all lines would exhibit identical power. However, in practice, frequency combs generated by mode-locked laser diodes (MLLDs), valued for their compactness, reliability, and

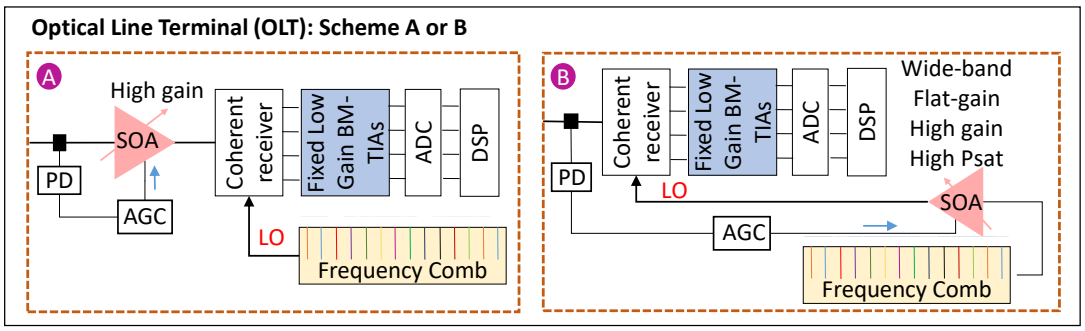


Figure 5.2: OLT receiver architecture showing two possible configurations when a frequency-comb source is used as the LO: (A) SOA-based signal pre-amplification and (B) SOA-based LO power boosting.

efficiency, and by other comb sources exhibit power variations of several decibels across the spectral span. Thus, while the central lines may be close to the average level, edge lines are often weaker. For example, a $+16$ dBm total output power comb source with a 3 dB variation over a 1.42 THz span has been reported in [60]. With an additional conservative demultiplexer insertion loss of up to 6 dB, the actual usable line powers typically range from -3 dBm down to -6 dBm.

This spectral imbalance directly impacts upstream reception, since the photocurrent in coherent detection scales with the product of the upstream signal field and the LO field, any reduction in LO power translates to reduced sensitivity. If an ONU wavelength aligns with a weak comb line, the degradation is particularly severe.

Therefore, while frequency combs provide wavelength resilience and enable colorless operation, the combined effects of power spreading and non-flat spectra make optical amplification essential. This naturally motivates the inclusion of receiver optical amplification, as discussed in the following subsection.

5.1.2 Optical Amplification for Low Power LO Compensation

Using a frequency comb source as LO, although cost-effective, distributes the total power of the comb across many spectral lines, resulting in low power LO tones. To maintain receiver sensitivity when using N_{comb} comb lines, compared to the case with a single line, optical amplification becomes essential to ensure the received signal is strong enough given the relatively low-power LO. SOAs are well-suited for this role, offering low cost, compact size, and scalability, making them ideal for integration with coherent receivers. Figure 5.2 illustrates two amplification schemes, where the amplifier can be placed either in the LO path or in the signal

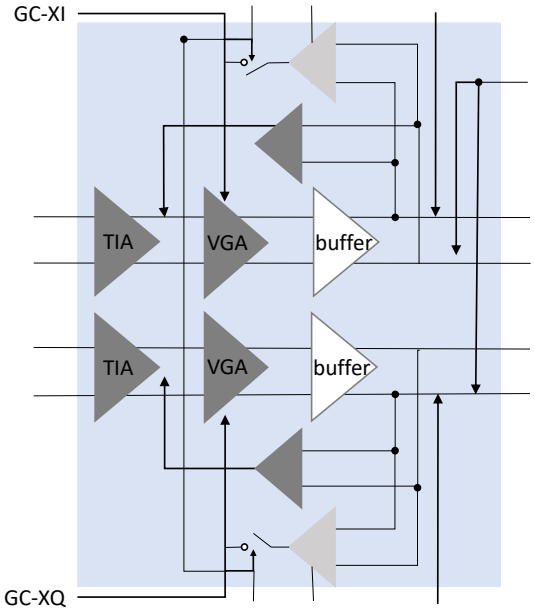


Figure 5.3: Dual-channel TIA–AGC architecture in automatic adjustable mode. This diagram represents X channel only. Y channel has the same diagram.

path. The following discuses the requirements and performance considerations of each approach. Before that, we examine the receiver architecture to provide a better understanding of how the receiver operates and regulates its gain based on the incoming packet power.

Coherent Receiver Front-End Design

In this study, an integrated coherent receiver (ICR, model FIM24902) is employed. The receiver incorporates an adaptive-gain mechanism that maintains a constant output swing for each received packet, thereby enabling packet-level power equalisation in the electrical domain. This operating mode provides a useful reference for assessing the behaviour of the SOA under idealised receiver conditions. It should be emphasised that this adaptive-gain operation is applicable only to continuous-mode measurements and is not suitable for burst-mode operation, as it cannot support fast gain switching on a packet-by-packet basis. Accordingly, results obtained using the adaptive-gain receiver are presented in this chapter to isolate the impact of SOA nonlinearity on system performance and to benchmark the proposed schemes against coherent transmission employing high local-oscillator power and a high-gain, high-bandwidth, high-dynamic-range receiver. Throughout this chapter, *CIP-SOA-S* is used for all measurements.

Figure 5.3 illustrates the dual-channel TIA–AGC architecture that forms the front-

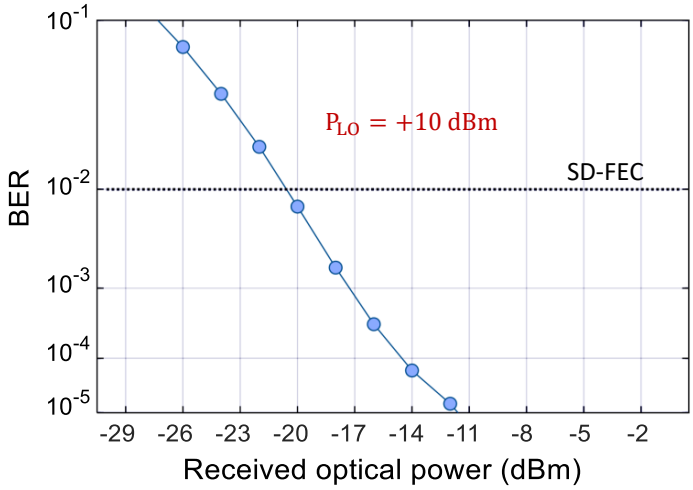


Figure 5.4: Experimentally measured BER versus input optical power for a continuous-mode 50 Gbaud DP-16QAM back-to-back transmission using the integrated coherent receiver, without optical amplification and with an LO power of +10 dBm.

end of the device. As shown, each channel consists of a TIA with a fixed gain of 150 V/A, followed by a variable-gain amplifier (VGA) that regulate the overall output swing. During this analysis, the VGAs dynamically adjust their gain to maintain a constant electrical amplitude, resulting in a differential transimpedance that varies from 43.5 dBΩ to 70.1 dBΩ, as specified in the datasheet. This methodology isolates the effects of the SOA operation, thereby reducing the influence of the receiver front end on the measured performance.

Figure 5.4 shows the BER performance of a 50 Gbaud DP-16QAM back-to-back transmission using the integrated coherent receiver as a function of input optical power, measured without optical amplification and with an LO power of +10 dBm. Measurements are performed in continuous mode with the receiver analogue gain adjusted according to the input power. The receiver sensitivity at the SD-FEC threshold is approximately -21 dBm. This value provides a reference sensitivity at high LO power and serves as a baseline for evaluating the impact of reduced LO power and optical amplification on receiver sensitivity. Notably, this sensitivity is achieved without the use of optical preamplification, demonstrating the superior sensitivity of coherent reception compared with IM/DD systems. As shown in the previous chapter, IM/DD transmission falls short of meeting the required power budget at data rate of 150 Gb/s, even when optical preamplification is employed.

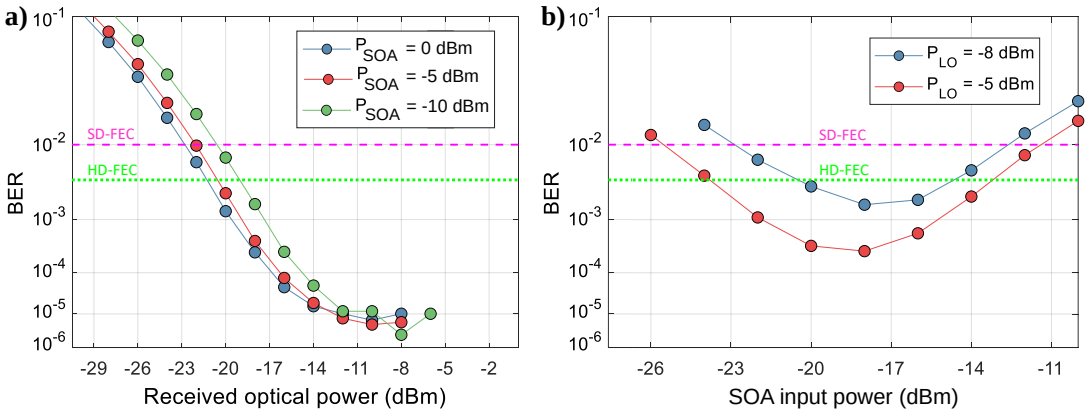


Figure 5.5: BER measurements for a 400 Gb/s DP-16QAM continuous-mode signal, where the receiver analogue gain is adjusted for each input power, comparing two configurations: (a) an SOA in the LO path with a fixed bias and input powers of 0 dBm, –5 dBm, and –10 dBm, resulting in different LO power levels, and (b) an SOA used as a preamplifier with a fixed bias and two different LO powers.

LO Power Booster: Amplifier at the LO Path

Figure 5.5.(a) shows the BER measurement for a 50 Gbaud DP-16QAM continuous-mode signal using an SOA (Model: *CIP-SOA-S*) biased at 120 mA in the LO path. In this experiment, the TIA gain is adjusted for each receiver input power level to equalise the received power. By regulating the SOA input power, the resulting LO output power varies between +9.2 dBm and +12.7 dBm, which keeps the LO power below the maximum limit specified in the datasheet. This configuration minimises SOA-induced nonlinearities, as the LO does not carry modulated data, and thus provides a clean gain boost for the weak comb lines. As shown, the ideal sensitivity level achieved at higher LO power can also be obtained at lower LO powers by using the booster amplifier. However, to meet the receiver sensitivity target, each LO tone would need to be amplified to +10 to +13 dBm, which exceeds the practical output power of integrated SOAs. Moreover, the SOA would require a flat and wide gain spectrum to accommodate the ONU laser wavelength drift, which is challenging to realise in practice. As a result, despite its theoretical benefits, LO-path amplification is not a practical solution for coherent PON systems.

Signal Preamplification: Amplifier at the Signal Path

Instead of amplifying the LO, this work adopts an SOA-based optical signal preamplifier at the receiver to sustain the link budget without boosting individual comb

lines. To satisfy the 29 dB power budget, the SOA gain must be sufficiently high to compensate both for the limited launch power (restricted to mitigate fibre nonlinearities) and for the relatively low LO power. Additional considerations such as SOA polarisation sensitivity and LO–ASE beat noise further influence the required gain margin. Figure 5.5.(b) demonstrates the effectiveness of SOA (*CIP-SOA-S*) preamplification in maintaining sufficient receiver sensitivity for a 50 Gbaud DP-16QAM transmission even at very low LO powers of –8 dBm. In this configuration, the increased optical power at the coherent receiver input reduces the relative impact of receiver noise equivalent power, such that the overall system performance becomes increasingly dependent on the OSNR. Reducing the LO power decreases the coherent mixing efficiency, since the detected electrical signal amplitude scales approximately as $i_{\text{sig}} \propto \sqrt{P_{\text{sig}} P_{\text{LO}}}$. Consequently, in a regime where the dominant noise contributions are largely independent of LO power, a reduction of the LO power by Δ dB must be compensated by approximately Δ dB increase in received signal power in order to maintain a constant electrical SNR. This is consistent with the measured behaviour between $P_{\text{LO}} = -8$ dBm and $P_{\text{LO}} = -5$, where a 3 dB change in LO power leads to an approximately 3 dB change in sensitivity.

Beyond providing amplification, the SOA can also function as an optical power equaliser by dynamically adjusting its gain to stabilise packet power before detection. This reduces both the dynamic range and gain requirements of the burst mode TIA. Although SOA gain saturation at high input powers can introduce nonlinear distortions, leading to patterning effects degrading both phase and amplitude, and increased BER, as illustrated in the figure, these impairments can be mitigated through appropriate SOA gain control, as demonstrated in the previous chapter.

5.2 Experimental Setup

Figure 5.6 illustrates the emulated coherent optical upstream transmission setup operating at 50 Gbaud with dual-polarisation QPSK and 16QAM modulation formats, which is used to evaluate the SOA-based power equalisation in CPON. Although the feasibility of the scheme is evaluated in continuous transmission mode, the results can be extended to burst-mode transmission, as demonstrated in the previous chapter on 100 Gb/s PAM4 systems, where comparable performance was achieved under both continuous and burst-mode operation. The SOA-based power equalisation relies on envelope-level gain dynamics that are

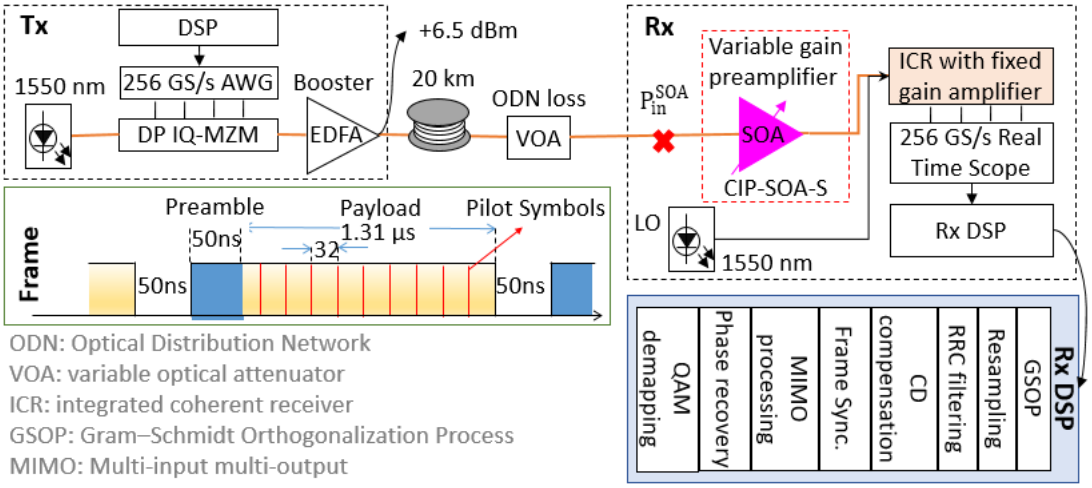


Figure 5.6: Experimental setup of a 20 km optical upstream link in a flexible coherent PON supporting a net data rate of up to 312 Gb/s. The packet frame structure is also shown.

slow relative to the symbol rate, and therefore remains valid for burst transmissions, provided that the SOA gain is settled prior to payload reception. In coherent PON systems, the additional penalties introduced by burst-mode operation are predominantly associated with receiver DSP tasks such as fast frequency offset estimation, carrier recovery, and burst synchronisation, which have been widely studied in prior works [129], [130], [131]. The primary objective of this study is to investigate SOA-based optical power equalisation, rather than to perform an in-depth optimisation of burst-mode DSP algorithms. Consequently, continuous-mode transmission is adopted to decouple DSP convergence effects from the optical front-end behaviour and to provide a clear evaluation of the proposed equalisation scheme.

While the proposed coherent PON architecture assumes the use of a cost-effective, wider-linewidth laser at the ONU and a comb-based source at the OLT receiver, the experimental validation does not strictly follow this configuration. Instead, narrow-linewidth discrete lasers are employed in order to minimise phase-noise impairments and approximate an ideal transmitter. By suppressing transmitter-induced phase noise, the measurements ensure that the observed performance trends are dominated by the receiver processing rather than carrier instability. However, such narrow-linewidth lasers are not representative of cost-sensitive practical ONU implementations, where linewidths in the range of several hundred kHz to MHz are more typical.

At the transmitter side, 50 Gbaud electrical signals are generated by a 256 GSa/s

arbitrary waveform generator (AWG). As shown in the frame structure, each sequence contains a 50 ns corresponding to the experimentally observed DSP convergence time under continuous-mode operation. In a practical burst-mode implementation, additional preamble may be required to accommodate analogue front-end settling. The frame further includes a 1.31 μs payload, and a 50 ns guard time. An external cavity laser (ECL) operates at 1550 nm with a specified linewidth (LW) of 30 kHz is coupled into the dual I/Q modulators to generate the optical signal. An EDFA boosts the optical launch power to 6.5 dBm before the signal is transmitted over 20 km of SMF. A variable optical attenuator (VOA) is used to simulate the ODN loss. Then, the optical signal is directed into the receiver, which includes an SOA serving as a preamplifier and optical equaliser, followed by the integrated coherent receiver as characterised earlier in this chapter. Another ECL (LW$<$100 kHz) acts as an LO to mix with the received signal before the signal is converted to the electrical domain by the ICR. A real-time oscilloscope operating at 256 GSa/s is used to capture the electrical signals.

In the receiver DSP, the amplitude and phase imbalance are compensated using the GSOP. The signals are then downsampled and filtered. A fixed 15-tap time-domain equaliser is applied to compensate for CD impairments, followed by coarse frequency offset compensation and frame synchronisation. Polarisation demultiplexing and signal equalisation are performed using a 2x2 MIMO equaliser based on a 21-tap least mean squares algorithm with training. Phase recovery is performed using a pilot-aided approach, in which pilot symbols are periodically inserted into the transmitted symbol stream to enable accurate phase-noise tracking. One pilot symbol is inserted every k payload symbols, resulting in a total number of pilot symbols

$$N_{\text{pilot}} = \left\lceil \frac{N_{\text{payload}}}{k} \right\rceil, \tag{5.3}$$

where N_{payload} denotes the number of payload symbols in a frame and $\lceil . \rceil$ represents the round-up operation. In the considered system, a pilot insertion rate of one pilot symbol per 32 payload symbols is employed, yielding $N_{\text{pilot}} = 2047$. This pilot density provides a suitable trade-off between phase-noise tracking capability and symbol overhead. However, since the effective phase noise scales with the sum of the transmitter and LO linewidths, a practical ONU employing a wider-linewidth laser would exhibit increased phase noise and faster carrier phase drift. Consequently, more frequent pilot insertion would be required to ensure reliable phase tracking. The pilot overhead reported in this work should

therefore be regarded as a lower-bound estimate for practical implementations.

Only payload symbols are subject to channel coding, while preamble and pilot symbols remain uncoded, since they are known symbols used for synchronisation and phase estimation rather than information transmission. This design avoids unnecessary redundancy and decoding complexity, thereby maximising the effective net data rate. For a dual-polarisation coherent system with symbol rate R_s and modulation order of M, the gross line rate is given by

$$R_{\text{line}} = 2 \times R_s \times \log_2(M), \tag{5.4}$$

where the factor of two accounts for dual polarisation. If N_{total} denotes the total number of transmitted symbols per frame, including payload, preamble, and pilot symbols, the fraction of symbols carrying payload data is then given by

$$\eta_{\text{frame}} = \frac{N_{\text{total}} - N_{\text{preamble}} - N_{\text{pilot}}}{N_{\text{total}}}. \tag{5.5}$$

Assuming an FEC overhead of OH_{FEC}, the net information rate of the system can be expressed as

$$R_{\text{net}} = R_{\text{line}} \times \eta_{\text{frame}} \times \frac{1}{1 + \text{OH}_{\text{FEC}}} \tag{5.6}$$

Applying this formulation to a 50 Gbaud coherent PON using DP-16QAM , the gross line rate is 400 Gb/s. Therefore, with a 20% SD-FEC overhead and the previously defined frame structure including preamble and pilot symbols, the resulting net data rate is approximately 312 Gb/s.

Similarly, for 50 Gbaud DP-QPSK, the gross line rate becomes 200 Gb/s, and, assuming the same framing structure and FEC overhead, the corresponding net data rate is approximately 156 Gb/s.

Finally, the BER is obtained by comparing the transmitted and received bit sequences after equalisation, phase recovery, and symbol demapping.

5.3 Experimental Results

Figure 5.7 demonstrates the BER measurement versus the SOA input power, P_{in}^{SOA}, in a 20 km transmission at LO power, P_{LO}, of -6 dBm (corresponding to 40 comb lines) and -3 dBm (corresponding to 20 comb lines). The SOA bias is fixed at 120 mA to achieve its maximum gain and increase the receiver sensitivity, while the TIA/VGA analogue gain of the receiver is adjusted to maintain

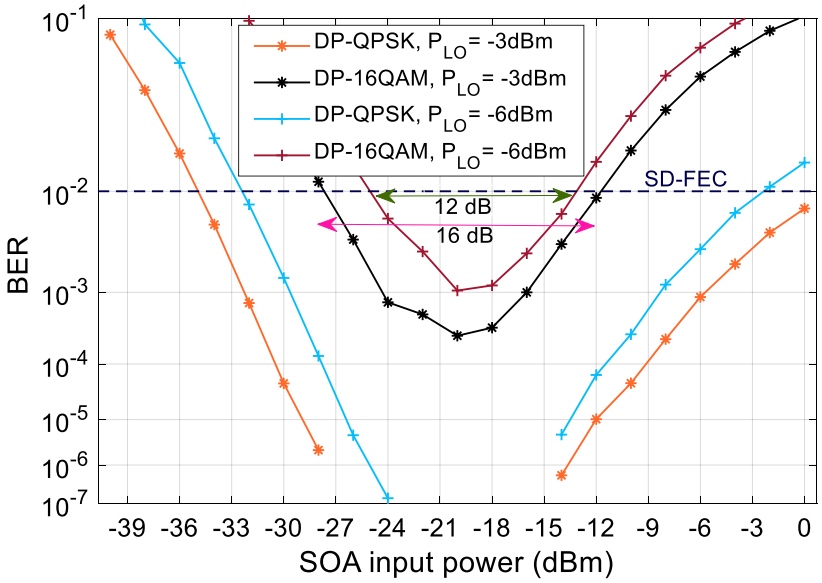


Figure 5.7: Experimental results of 50 Gbaud DP-QPSK and DP-16QAM signals in continuous mode operation after 20 km transmission, measured at different LO power levels using an SOA preamplifier biased at 120 mA and a variable analogue-gain receiver.

a constant output swing, emulating a fast, high-dynamic-range, high-gain, and high-bandwidth BM-TIA, which is challenging to implement in practice, as discussed in Chapter 2.

In order to better understand the BER degradation observed after 20 km fibre transmission, Figure 5.8 compares the received constellations after fibre propagation with those obtained in the B2B configuration for an SOA input power of 0 dBm. In the B2B case, the dominant impairment is caused by SOA nonlinearities, primarily gain saturation and the associated amplitude-to-phase coupling arising from the SOA effective alpha factor (α_{eff}). At such a high input power to the SOA, the amplifier operates deep in the saturation regime, resulting in strong nonlinear phase noise and constellation broadening for DP-QPSK, as well as pronounced warping and cluster overlap for DP-16QAM. This behaviour is consistent with previously reported experimental results on advanced modulation formats amplified by SOAs, where nonlinear phase noise and constellation deformation increase rapidly with input power (see Chapter 2).

After 20 km, the accumulated dispersion is substantially larger, so the fixed time-domain equaliser can leave residual ISI. When the received signal is then amplified by an SOA operating deep in saturation, the saturation-induced patterning becomes more pronounced as the SOA is driven by a dispersion-impaired wave-

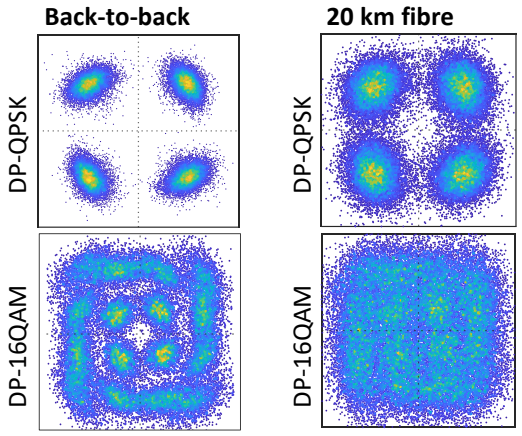


Figure 5.8: Constellation diagrams for both modulation formats measured at an SOA input power of 0 dBm and an LO power of -3 dBm, comparing the back-to-back configuration with 20 km fibre transmission.

form in which chromatic dispersion enhances the temporal overlap of symbols and the resulting instantaneous power variations already present due to modulation and pulse shaping. The resulting nonlinear, memory-dependent distortion (together with ASE noise, which is present in both cases) is not fully removable by linear CD/MIMO equalisation, leading to increased constellation spreading and asymmetry for DP-QPSK, and much more severe symbol overlap and apparent level compression for DP-16QAM.

Although the DP-QPSK signal is less affected, the dynamic range of the DP-16QAM signal is limited to only 12 dB due to SOA patterning, illustrating the challenges for increasing PON data rates via higher order modulation schemes. This motivates the need for dynamic SOA gain control to simultaneously minimise impairments from gain saturation and perform burst to burst amplitude equalisation in the optical domain, to simplify BM-TIA design.

Figure 5.9 illustrates the SOA-based equalisation capability in handling signals with a large dynamic range. The receiver analogue gain is fixed at a low setting, with a slightly higher value for an LO power of -6 dBm compared to -3 dBm. In this experiment, variable bias technique is used to maintain the SOA output power at 0 dBm. By adjusting the SOA bias current, the impact of nonlinear effects can be reduced, as evidenced by the improved constellation diagrams for both DP-QPSK and DP-16QAM. Reducing the SOA bias current lowers the available carrier density and the small-signal gain. At high input powers, this causes the SOA to operate less deeply in saturation, reducing carrier depletion dynamics. As a result, both gain compression (amplitude distortion) and carrier-induced

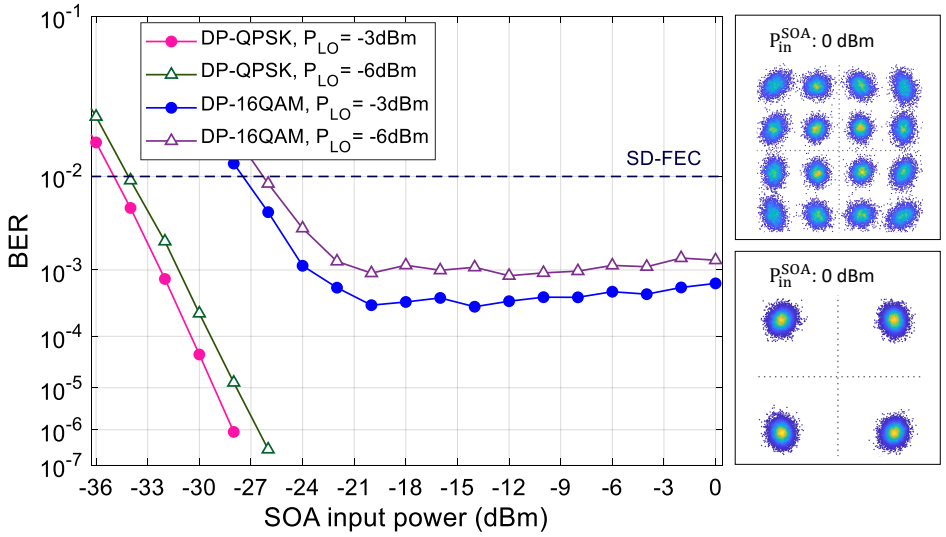


Figure 5.9: Experimental results of 50 Gbaud DP-QPSK and DP-16QAM continuous mode signals at different values of LO power in a 20 km transmission using variable gain SOA and fixed, low receiver analogue gain. Constellation diagrams are for -3 dBm LO power at SOA input power of 0 dBm.

phase distortion, linked through the effective alpha factor. While lowering the bias current reduces nonlinear distortion for both modulation formats, the remaining amplitude-dominated distortion and reduced constellation spacing ultimately limit the performance of DP-16QAM, leading to a BER floor. Nevertheless, this approach enables a net data rate of up to 312 Gb/s using the DP-16QAM modulation format over a wide dynamic range of 26 dB.

Since the received signal power and LO power are comparable in both fixed-bias and variable bias experiments at the lowest input powers, the sensitivities at an LO power of -3 dBm are essentially identical for both measurements. When the LO power is reduced to -6 dBm, the coherent signal–LO beat amplitude decreases, and the measurement becomes more sensitive to the receiver analogue gain. Consequently, small differences in receiver gain settings between the two measurement procedures can produce a modest difference in the measured sensitivity.

5.4 Summary

This chapter presents SOA-based optical power equalisation for an emulated 50 Gbaud upstream coherent PON employing dual-polarisation QPSK and 16QAM. The analysis is performed in continuous transmission mode to isolate

and clearly evaluate the SOA-based optical power equalisation without conflating its performance with burst-mode DSP convergence effects. The proposed design concept employs a frequency comb source at the OLT to maintain wavelength alignment between the ONU and LO, providing the motivation for using an SOA in coherent systems that typically do not require preamplification. Although the experimental demonstration does not employ a comb source, it validates the effectiveness of SOA-based equalisation in a high-speed coherent PON. A variable-bias control scheme dynamically adjusts the SOA gain according to the received packet power, equalising signal levels in the optical domain and mitigating non-linear distortions due to gain saturation. The receiver operates with a low-power LO and fixed, low TIA/VGA gain, reducing complexity and power consumption compared to conventional burst-mode receivers. The system supports net rates up to 312 Gb/s with a 32 dB loss budget and a 26 dB dynamic range, confirming that SOA-based optical equalisation is a viable approach for simplifying receiver design in future high-capacity coherent PONs.

The results of this chapter have been drafted as a manuscript for submission to *Photonics Technology Letters*.

Chapter 6

Conclusion

The final chapter presents an overview of the main contributions and novel aspects of this work, and concludes with suggestions for future research directions.

This thesis has investigated SOA-based optical burst power equalisation as an effective approach to overcoming the dynamic range limitations in next-generation PONs. As data rates move towards 100 Gb/s per wavelength for IM/DD and 400 Gb/s for coherent systems, conventional burst-mode receivers face increasing challenges due to limited linearity and bandwidth. By introducing gain control in the optical domain, the proposed SOA-based techniques alleviate these constraints while reducing the need for complex digital compensation.

Two proposed equalisation methods: (A) variable bias and (B) control light injection are experimentally validated, demonstrating wide dynamic range operation and high receiver sensitivity in 100 Gb/s PAM4 burst-mode transmission. The concept is further extended to coherent PONs using DP-16QAM, where SOA-based equalisation enables reliable detection across a wide range of input powers while relaxing wavelength alignment requirements.

The following sections summarise the key findings, discuss the broader implications of SOA-based equalisation for high-speed optical access networks, and outline future research directions aimed at achieving scalable, energy-efficient, and cost-effective PON receiver integration.

6.1 Summary of Contributions

Chapter 3 investigates the use of SOAs for optical burst power equalisation in high-speed PON receivers. It analyses the SOA gain dynamics and their nonlinear impact on advanced modulation formats, showing that gain saturation induces patterning effects in M-PAM and both amplitude and phase distortion in coherent signals such as dual-polarisation QPSK and 16QAM. To address these impairments, two equalisation techniques are developed: (A) variable bias and (B) control light injection. Both methods regulate the SOA gain to maintain constant output power across a wide input range, extending the amplifier's linear operating region and improving receiver sensitivity. The variable bias method adjusts the SOA gain by controlling the carrier injection into the active region, whereas the control light injection method regulates the gain by inducing carrier depletion through stimulated emission. Experimental and analytical results confirm that these approaches provide more than 20 dB of gain adjustment, satisfying the dynamic range required by next-generation 50G-PON standards. Among them, control light injection delivers superior performance at high input powers, offering higher OSNR and linearity by keeping the SOA in its linear regime. The analysis also shows that input-side injection and wavelength alignment to the SOA's red-shifted gain spectrum further enhance gain control and optical performance.

In Chapter 4, SOA-based optical power equalisation is experimentally demonstrated as a practical solution for managing large upstream power variations in 100 Gb/s PAM4 IM/DD PONs. The results, published in [A1], and [A2], confirm that dynamic SOA gain control, implemented through variable bias or control light injection, effectively suppresses nonlinear gain saturation and extends the receiver dynamic range beyond 23 dB while remaining compatible with low-cost 25G-class receivers. By transferring power regulation to the optical domain, the approach removes the need for complex burst-mode TIAs and simplifies receiver design without compromising performance. The technique is also verified under burst-mode operation and significant chromatic dispersion, demonstrating its robustness for 50 Gbaud PAM4 transmission.

In addition, a transfer-printed SOA, which is fabricated by the III-V Materials and Devices Group at Tyndall National Institute, is evaluated in a 100 Gb/s transmission to assess integration potential. These results form part of an upcoming collaborative journal publication. The study also shows that 50 Gbaud PAM8 transmission does not meet the required power budget or dynamic range, even

with EDFA preamplification. This finding highlights the limitations of IM/DD at higher modulation orders and motivates the transition toward coherent PON architectures, which are investigated in Chapter 5.

Chapter 5 further investigates SOA-based optical power equalisation at even higher speeds using coherent technology. The proposed architecture employs a frequency comb source at the OLT to maintain wavelength alignment between the ONU and LO, motivating the inclusion of an SOA in the receiver. Although the experimental setup does not use a real comb source, it validates the concept through variable-bias SOA control that equalises packet powers in the optical domain. The receiver operates with a low-power LO and fixed, low receiver analogue gain, achieving 312 Gb/s net rate with a 32 dB loss budget and a 26 dB dynamic range. These results demonstrate that SOA-based equalisation can effectively simplify coherent receiver design and extend the performance of future high-capacity PONs. These results have been prepared for submission to *PTL*.

6.2 Future Research Directions

The results presented in this thesis open promising avenues for further investigation, particularly in the development of practical SOA-based power equaliser hardware for OLT receivers and in the integration of optical-domain equalisation with comb-driven coherent PON architectures. These directions naturally extend the concepts introduced in this work and offer a roadmap toward fully integrated, high-speed, and high dynamic-range receivers for next-generation access networks.

Practical Realisation of SOA-Based Gain Controllers

The work presented in this thesis establishes the potential of SOA-based optical equalisation to simplify high-speed IM/DD receivers and relax the increasingly demanding linearity and bandwidth requirements of next-generation BM-TIAs, but the gain-control mechanisms themselves are not physically implemented. Instead, the thesis evaluates their feasibility and outlines how such a controller could operate in practice. The proposed architecture includes the required functional blocks for burst detection, input-power estimation, gain-level selection and SOA drive adjustment, together with the timing budget and latency considerations that determine their performance. This structure shows that real-time gain switching within typical PON guard times is achievable with existing ADCs,

DACs, FPGA logic and monitoring photodiodes.

By providing this architectural framework and outlining the operating ranges, timing constraints, and functional requirements of each block, the thesis offers a practical foundation for designers aiming to realise a hardware automatic gain controller for driving the SOA. Future research can build on this by implementing and validating a complete controller, evaluating its performance in conjunction with a practical burst-mode receiver front-end, and exploring integrated or co-packaged solutions in which monitoring, control logic, and SOA gain adjustment are combined within a compact, low-power module. Such developments would bridge the remaining gap between the physical-layer feasibility demonstrated here and the deployment of optical-domain power equalisation in next-generation IM/DD PON receivers.

Integration of SOA-Based Equalisation with Frequency Comb Source Driven Coherent PON Receivers

This thesis also presents a proof-of-concept for SOA-based power equalisation in coherent PONs by emulating the reduced LO power levels expected when the OLT employs a frequency comb. This result highlights a promising future direction in which optical-domain equalisation is combined with comb-based coherent receiver architectures to achieve stable wavelength alignment between ONU transmitters and the LO while supporting wide dynamic-range operation. Existing demonstrations of coherent and colourless PON architectures already use frequency combs at the OLT to provide multiple phase-coherent wavelengths and to stabilise the wavelength relationship between the ONU transmitters and the OLT reference. These works show that comb sources can act as a shared optical reference and can, in principle, also serve as a multi-wavelength LO for coherent reception. What remains largely unexplored, however, is how a comb-derived LO behaves under realistic upstream burst-mode operation. In addition, the per-line power, noise characteristics and spectral uniformity of the comb may influence coherent-receiver performance when combined with SOA-based optical equalisation.

The high-speed characterisation of TP-SOAs presented in this thesis provides an additional opportunity. TP technology enables compact, low-loss integration of III–V amplifiers onto silicon photonic receivers, allowing SOA-based automatic gain control to be placed directly in front of the coherent hybrid. When combined with on-chip comb distribution networks, this creates a compelling receiver ar-

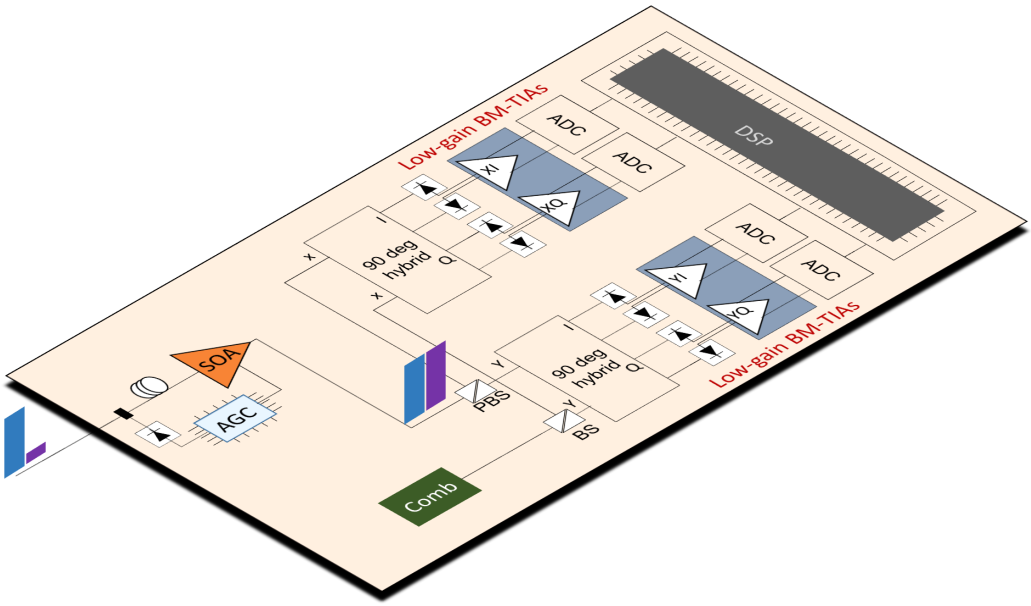


Figure 6.1: Schematic of an integrated optical equaliser in a coherent receiver employing an integrated comb source as the LO for future ultra-high-speed PONs.

chitecture in which each comb line is delivered to a dedicated coherent branch equipped with a TP-SOA. Such a configuration naturally supports wavelength alignment, automatic compensation of LO power imbalance, and stable reception over a wide upstream dynamic range. It also opens a path toward a compact, integrated coherent OLT receiver in which the LO, SOA equaliser and coherent front-end are realised on the same photonic platform.

Overall, these considerations point toward future work exploring how a transfer-printed comb source could act as a tuneable LO, enabling compact integration of the LO, a TP-SOA equalisation stage and a burst-mode coherent front-end with low-gain, lower-dynamic-range BM-TIAs within a practical receiver design, as illustrated in Figure 6.1. Addressing these open questions has the potential to define the architecture of future coherent PON receivers and to enable high-speed, high-dynamic-range operation in a format suitable for commercial deployment.

Acronyms

M-PAM M-level pulse amplitude modulation

M-QAM M-aray quadrature amplitude modulation

100GE-PON 100-Gigabit Ethernet PON

ADC Analogue-to-digital converter

AFE Analogue Front End

AFG Arbitrary Function Generator

APD avalanche photodiode

APON ATM PON

ASE Amplified Spontaneous Emission

ATM Asynchronous Transfer Mode

AWG Arrayed Waveguide Grating

AWG-Gen Arbitrary Waveform Generator

AWGN Additive white Gaussian noise

B2B back-to-back

BER Bit Error Rate

BM-TIA burst-mode trans-impedance amplifiers

BMRx burst-mode receiver

BPF band-pass filter

BPON Broadband PON

BPS Blind Phase Search

BPSK Binary phase-shift keying

CB conduction band

CD Chromatic dispersion

CFO Carrier Frequency Offset

CPON coherent PON

CPR Carrier Phase Recovery

CRX Coherent Receiver

DAC Digital-to-Analogue Converter

DFB Distributed Feedback

DP-M-QAM dual-polarisation M-level quadrature amplitude modulation

DP-IQM Dual-Polarisation I/Q Modulator

DP-QAM dual polarisation QAM

DP-QPSK dual polarisation QPSK

DR Dynamic Range

DSL digital subscriber line

DSP digital signal processing

ECL external cavity laser

EDFA erbium-doped fibre amplifier

EoB end-of-burst

EPON Ethernet PON

ER Extinction Ratio

EVM Error Vector Magnitude

FC-NNE Fully Connected Neural Networks

FEC Forward Error Correction

FF-NNE Feed-Forward Neural Network

FFE Feed-Forward Equalisers

FIR Finite Impulse Response

FPGA Field Programmable Gate Array

FSAN Full Service Access Network

FSR free-spectral range

FTTC fibre to the Curb

FTTH fibre to the Home

FTTN fibre to the Node

GPON Gigabit PON

GRU Gated Recurrent Units

GSOP Gram–Schmidt orthogonalisation procedure

HH heavy-hole

IEEE Electrical and Electronics Engineers

IM/DD intensity modulation and direct detection

IoT Internet of Things

ISI Inter-Symbol Interference

ITU International Telecommunication Union

LDPC low-density parity-check

LH light-hole

LMS Least Mean Square

LO local oscillator

LUT Lookup table

LW linewidth

MIMO Multi-Input Multi-Output

ML Machine Learning

MLLD mode-locked laser diode

MQW multiple quantum-well

MSA Multisource Agreement

MSE Mean Squared Error

MZM Mach–Zehnder modulator

NF Noise Figure

NG-PON2 Next-Generation PON 2

NRZ Non-return-to-zero

ODN Optical Distribution Network

OLT Optical Line Terminal

ONU Optical Network Unit

OSNR Optical signal-to-noise ratio

P2MP point-to-multipoint

PAM4 4-level pulse amplitude modulation

PDF Probability Density Function

PDMS polydimethylsiloxane

PMD Polarisation Mode Dispersion

PON Passive optical network

PRBS Pseudo-random bit sequences

PSD Power Spectral Density

QPSK quadrature phase shift keying

RMS root-mean-square

RNN Recurrent Neural Network

SBS Stimulated Brillouin Scattering

SD-FEC soft decision FEC

SER Symbol Error Probability

SiGe BiCMOS Silicon–Germanium Bipolar Complementary Metal–Oxide–Semiconductor

SiGe HBTs SiGe heterojunction bipolar transistors

SMF Single-Mode Fibre

SNR signal-to-noise ratio

SOA Semiconductor Optical Amplifiers

SoB start-of-burst

SQW Single quantum-well

TDM-PON Time Division Multiplexing PON

TE transverse electric

TM transverse magnetic

TP-SOA transfer printed SOA

TWDM Time and Wavelength Division Multiplexing

VB valence band

VDSL Very High-Speed DSL

VGA variable-gain amplifier

VOA variable optical attenuator

WDM wavelength division multiplexer

WDM-PON Wavelength Division Multiplexing PON

WSS Wavelength-Selective Switch

References

[1] T. Pfeiffer, P. Dom, S. Bidkar, F. Fredricx, K. Christodoulopoulos, and R. Bonk, "PON going beyond FTTH [Invited Tutorial]," *Journal of Optical Communications and Networking*, vol. 14, no. 1, A31–A40, 2022. DOI: 10.1364/JOCN.439241.

[2] Broadband optical access systems based on Passive Optical Networks (PON), ITU-T Recommendation G.983.1, International Telecommunications Union, Geneva, Switzerland, Oct. 1998.

[3] F. Effenberger, G. Kramer, and B. Hesse, "Passive optical networking update [PON Update]," *IEEE Communications Magazine*, vol. 45, no. 3, S6–S8, 2007. DOI: 10.1109/MCOM.2007.344577.

[4] P. Torres-Ferrera, F. Effenberger, M. S. Faruk, S. J. Savory, and R. Gaudino, "Overview of high-speed TDM-PON beyond 50 Gbps per wavelength using digital signal processing [Invited Tutorial]," *Journal of Optical Communications and Networking*, vol. 14, no. 12, pp. 982–996, 2022. DOI: 10.1364/JOCN.468920.

[5] S. Jain et al., "World's First XG-PON Field Trial," *Journal of Lightwave Technology*, vol. 29, no. 4, pp. 524–528, 2011. DOI: 10.1109/JLT.2010.2104313.

[6] 10-gigabit-capable symmetric passive optical network (XGSPON), ITU-T Recommendation G.9807.1, International Telecommunications Union, Geneva, Switzerland, 2016.

[7] D. Nesset, "NG-PON2 Technology and Standards," *Journal of Lightwave Technology*, vol. 33, no. 5, pp. 1136–1143, 2015. DOI: 10.1109/JLT.2015.2389115.

[8] Y. Luo et al., "Time- and Wavelength-Division Multiplexed Passive Optical Network (TWDM-PON) for Next-Generation PON Stage 2 (NG-PON2)," *Journal of Lightwave Technology*, vol. 31, no. 4, pp. 587–593, 2013. DOI: 10.1109/JLT.2012.2215841.

[9] J. S. Wey et al., "Physical layer aspects of NG-PON2 standards—Part 1: Optical link design [Invited]," *Journal of Optical Communications and Networking*, vol. 8, no. 1, pp. 33–42, 2016. DOI: 10.1364/JOCN.8.000033.

[10] V. Houtsma, D. van Veen, and E. Harstead, "Recent Progress on Standardization of Next-Generation 25, 50, and 100G EPON," *Journal of Lightwave Technology*, vol. 35, no. 6, pp. 1228–1234, 2017. DOI: 10.1109/JLT.2016.2637825.

[11] D. Zhang, D. Liu, X. Wu, and D. Nesset, "Progress of ITU-T higher speed passive optical network (50G-PON) standardization," *Journal of Optical Communications and Networking*, vol. 12, no. 10, pp. D99–D108, 2020. DOI: 10.1364/JOCN.391830.

[12] E. Harstead et al., "From 25 Gb/s to 50 Gb/s TDM PON: transceiver architectures, their performance, standardization aspects, and cost modeling," *Journal of Optical Communications and Networking*, vol. 12, no. 9, pp. D17–D26, 2020. DOI: 10.1364/JOCN.391945.

[13] 50-Gigabit-Capable Passive Optical Networks (50G-PON): Physical Media Dependent (PMD) Layer Specification, ITU-T Recommendation G.9804.3, International Telecommunications Union, Geneva, Switzerland, Sep. 2021.

[14] H. Huang, E. Akbaba, K. Li, H. Akel, T. Tsegaye, and S. Khatana, "First Demonstration of Sensitivity Improvement using an APD Receiver for a 100 Gbit/s Single Channel PAM4 Link," in *2018 Conference on Lasers and Electro-Optics (CLEO)*, 2018, pp. 1–2.

[15] J. Zhang et al., "SOA Pre-Amplified 100 Gb/s/λ PAM-4 TDM-PON Downstream Transmission Using 10 Gbps O-Band Transmitters," *Journal of Lightwave Technology*, vol. 38, no. 2, pp. 185–193, 2020. DOI: 10.1109/JLT.2019.2944558.

[16] L. N. Venkatasubramani, A. Galib Reza, V. S. Mikhrin, A. Gubenko, A. R. Kovsh, and L. Barry, "100 Gbps PAM4 Transmissions over 50 km with 40 dB Power Budget for PON using a High-Gain Quantum Dot SOA," in *2024 Optical Fiber Communications Conference and Exhibition (OFC)*, 2024, pp. 1–3.

[17] G. Rizzelli Martella, A. Nespola, S. Straullu, F. Forghieri, and R. Gaudino, "Scaling Laws for Unamplified Coherent Transmission in Next-Generation Short-Reach and Access Networks," *Journal of Lightwave Technology*, vol. 39, no. 18, pp. 5805–5814, 2021. DOI: 10.1109/JLT.2021.3092523.

[18] E. Agrell et al., "Roadmap on optical communications," *Journal of Optics*, vol. 26, no. 9, p. 093 001, Jul. 2024. DOI: 10.1088/2040-8986/ad261f.

[19] G. Coudyzer et al., "100 Gbit/s PAM-4 Linear Burst-Mode Transimpedance Amplifier for Upstream Flexible Passive Optical Networks," *Journal of Lightwave Technology*, vol. 41, no. 12, pp. 3652–3659, 2023. DOI: 10.1109/JLT.2023.3262319.

[20] M. D. Santa et al., "25Gb/s PAM4 burst-mode system for upstream transmission in passive optical networks," in *2017 Optical Fiber Communications Conference and Exhibition (OFC)*, 2017, pp. 1–3.

[21] S. V. Pato, R. Meleiro, D. Fonseca, P. Andre, P. Monteiro, and H. Silva, "All-Optical Burst-Mode Power Equalizer Based on Cascaded SOAs for 10-Gb/s EPONs," *IEEE Photonics Technology Letters*, vol. 20, no. 24, pp. 2078–2080, 2008. DOI: 10.1109/LPT.2008.2006629.

[22] S. Porto, C. Antony, P. Ossieur, and P. D. Townsend, "An upstream reach-extender for 10Gb/s PON applications based on an optimised semiconductor amplifier cas-

cade," in *2011 37th European Conference and Exhibition on Optical Communication*, 2011, pp. 1–3.

[23] C. Antony, G. Talli, and P. D. Townsend, "SOA based upstream packet equalizer in 10Gb/s extended-reach PONs," in *2009 Conference on Optical Fiber Communication*, 2009, pp. 1–3. DOI: 10.1364/OFC.2009.OThA5.

[24] J. Sugawa and H. Ikeda, "Development of OLT using semiconductor optical amplifiers as booster and preamplifier for loss-budget extension in 10.3-Gb/s PON system," in *OFC/NFOEC*, 2012, pp. 1–3.

[25] M. D. Santa, C. Antony, G. Talli, and P. D. Townsend, "Variable Gain SOA Pre-Amplifier for Optical Equalization of a 25Gb/s Burst-Mode PON Upstream with 10G Optics," in *2019 Optical Fiber Communications Conference and Exhibition (OFC)*, 2019, pp. 1–3.

[26] J. Potet et al., "Assessment of an SOA for Burst Mode Pre-Amplification in Higher Speed PON reaching 30dB of Optical Budget," in *2021 Optical Fiber Communications Conference and Exhibition (OFC)*, 2021, pp. 1–3.

[27] R. Bonk, "SOA for future PONs," in *2018 Optical Fiber Communications Conference and Exposition (OFC)*, 2018, pp. 1–3.

[28] A. Ghazisaeidi and L. A. Rusch, "On the Efficiency of Digital Back-Propagation for Mitigating SOA-Induced Nonlinear Impairments," *Journal of Lightwave Technology*, vol. 29, no. 21, pp. 3331–3339, 2011. DOI: 10.1109/JLT.2011.2165938.

[29] K. Wang, J. Zhang, L. Zhao, X. Li, and J. Yu, "Mitigation of Pattern-Dependent Effect in SOA at O-Band by Using DSP," *Journal of Lightwave Technology*, vol. 38, no. 3, pp. 590–597, 2020. DOI: 10.1109/JLT.2019.2946188.

[30] B. Haq et al., "Micro-Transfer-Printed III-V-on-Silicon C-Band Semiconductor Optical Amplifiers," *Laser & Photonics Reviews*, vol. 14, no. 7, p. 1 900 364, 2020. DOI: 10.1002/lpor.201900364.

[31] R. Koma et al., "Demonstration of Real-Time Burst-Mode Digital Coherent Reception With Wide Dynamic Range in DSP-Based PON Upstream," *Journal of Lightwave Technology*, vol. 35, no. 8, pp. 1392–1398, 2017. DOI: 10.1109/JLT.2016.2637357.

[32] R. Bonk et al., "Perspectives on and the road towards 100Gb/s TDM PON with intensity-modulation and direct-detection," *Journal of Optical Communications and Networking*, vol. 15, no. 8, pp. 518–526, 2023. DOI: 10.1364/JOCN.489228.

[33] K. Deng, X. Li, Y. Li, T. Zhou, J. Li, and M. Luo, "200 G bidirectional simplified coherent PON with a single DFB at the ONU side," *Opt. Express*, vol. 33, no. 6, pp. 13 422–13 429, Mar. 2025. DOI: 10.1364/OE.554552.

[34] Y. Fang et al., "Demonstration of 200G pre-amplified self-coherent PON," *Opt. Express*, vol. 33, no. 4, pp. 7705–7713, Feb. 2025. DOI: 10.1364/OE.547959.

[35] M. Li et al., "400Gb/s real-time coherent PON based on a silicon photonic integrated transceiver," *Opt. Express*, vol. 30, no. 26, pp. 47 847–47 855, Dec. 2022. DOI: 10.1364/OE.476600.

[36] S. Murphy, P. D. Townsend, and C. Antony, "Recurrent Neural Network Equalizer to Extend Input Power Dynamic Range of SOA in 100Gb/s/λ PON," in *2022 Conference on Lasers and Electro-Optics (CLEO)*, 2022, pp. 1–2.

[37] M. Sharif, J. K. Perin, and J. M. Kahn, "Modulation Schemes for Single-Laser 100 Gb/s Links: Single-Carrier," *Journal of Lightwave Technology*, vol. 33, no. 20, pp. 4268–4277, 2015. DOI: 10.1109/JLT.2015.2470523.

[38] B. Kovács et al., "Experimental Demonstration of 50-GBaud 16-QAM Coherent PON with Simplified Receivers," *IEEE Photonics Technology Letters*, vol. 35, no. 21, pp. 1123–1126, 2023. DOI: 10.1109/LPT.2023.3294748.

[39] B. Kovács et al., "200 Gb/s Coherent PON: Bidirectional Demonstration and System Considerations," *Journal of Optical Communications and Networking*, vol. 16, no. 5, B37–B47, 2024. DOI: 10.1364/JOCN.524289.

[40] Cable Television Laboratories, Inc., "Coherent Passive Optical Networks (CPON) Architecture Specification," CableLabs, Tech. Rep. CM-SP-CPON-ARCH-I01-230503, May 2023.

[41] J. G. Proakis and M. Salehi, *Digital Communications*, 5th ed. New York: McGraw–Hill, 2007, ISBN: 9780072957167.

[42] R. A. Shafik, M. S. Rahman, and A. H. M. R. Islam, "On the Extended Relationships Among EVM, BER and SNR as Performance Metrics," in *Proceedings of the 4th International Conference on Electrical and Computer Engineering (ICECE)*, Dhaka, Bangladesh, Dec. 2006, pp. 408–411.

[43] G. Coudyzer, P. Ossieur, J. Bauwelinck, and X. Yin, "A 25Gbaud PAM-4 Linear Burst-Mode Receiver With Analog Gain- and Offset Control in 0.25µm SiGe:C BiCMOS," *IEEE Journal of Solid-State Circuits*, vol. 55, no. 8, pp. 2206–2218, 2020. DOI: 10.1109/JSSC.2020.2987680.

[44] X. Yin, G. Coudyzer, P. Ossieur, L. Breyne, B. Van Lombergen, and J. Bauwelinck, "Linear Burst-Mode Receivers for DSP-Enabled Passive Optical Networks," in *2021 Optical Fiber Communications Conference and Exhibition (OFC)*, 2021, pp. 1–3.

[45] *Implementation agreement for integrated dual polarization intradyne coherent receivers*, OIF, IA OIF-DPC-Rx-01.0, Apr. 2010.

[46] S. M. Sze and K. K. Ng, *Physics of Semiconductor Devices*, 3rd. Hoboken, NJ, USA: John Wiley & Sons, 2007, ISBN: 978-0471143239.

[47] B. Razavi, *Design of Integrated Circuits for Optical Communications*. New York, NY, USA: McGraw-Hill, 2003, ISBN: 978-0071409158.

[48] B. Razavi, *RF Microelectronics*, 2nd. Upper Saddle River, NJ, USA: Prentice Hall, 2012, ISBN: 978-0137134731.

[49] T. Gurne et al., "First Demonstration of a 100 Gbit/s PAM-4 Linear Burst-Mode Transimpedance Amplifier for Upstream Flexible PON," in *2022 European Conference on Optical Communication (ECOC)*, 2022, pp. 1–4.

[50] K. Kikuchi, "Fundamentals of Coherent Optical Fiber Communications," *Journal of Lightwave Technology*, vol. 34, no. 1, pp. 157–179, 2016. DOI: 10.1109/JLT.2015.2463719.

[51] J. K. Fischer, C. Schmidt-Langhorst, C. Schubert, and H. G. Weber, "Bandwidth limitations in coherent optical receivers and their impact on digital signal processing," *Journal of Lightwave Technology*, vol. 32, no. 2, pp. 239–249, 2014. DOI: 10.1109/JLT.2013.2291664.

[52] M. Presi, G. Cossu, E. Riccardi, and P. Poggiolini, "Coherent PON technologies for beyond-100G access networks," *Journal of Optical Communications and Networking*, vol. 10, no. 10, A333–A342, 2018. DOI: 10.1364/JOCN.10.00A333.

[53] G. P. Agrawal, *Fiber-Optic Communication Systems* (Wiley Series in Microwave and Optical Engineering), 4th. Hoboken, NJ: John Wiley & Sons, 2010, ISBN: 978-0-470-50511-3.

[54] A. Kobyakov, M. Sauer, and D. Chowdhury, "Stimulated Brillouin scattering in optical fibers," *Adv. Opt. Photon.*, vol. 2, no. 1, pp. 1–59, Mar. 2010. DOI: 10.1364/AOP.2.000001.

[55] G. P. Agrawal, *Nonlinear Fiber Optics*, 5th ed. Boston: Academic Press, 2013, ISBN: 9780123970237.

[56] V. R. Supradeepa, Y. Feng, and J. W. Nicholson, "Stimulated Brillouin scattering thresholds in optical fibers for lasers linewidth broadened with noise," *Optics Express*, vol. 21, no. 4, pp. 4677–4687, 2013. DOI: 10.1364/OE.21.004677.

[57] Characteristics of a Single-Mode Optical Fibre and Cable, ITU-T Recommendation G.652, International Telecommunications Union, Geneva, Switzerland, Nov. 2016.

[58] D. van Veen and V. Houtsma, "Strategies for economical next-generation 50G and 100G passive optical networks [Invited]," *Journal of Optical Communications and Networking*, vol. 12, no. 1, A95–A103, 2020. DOI: 10.1364/JOCN.12.000A95.

[59] G. Yoffe, S. Zou, S. Rishton, R. Olson, M. Emanuel, and B. Pezeshki, "Widely-tunable 30mW laser source with sub-500kHz linewidth using DFB array," in *LEOS 2008 - 21st Annual Meeting of the IEEE Lasers and Electro-Optics Society*, 2008, pp. 892–893. DOI: 10.1109/LEOS.2008.4688909.

[60] M. M. H. Adib et al., "Colorless Coherent TDM-PON Based on a Frequency-Comb Laser," *Journal of Lightwave Technology*, vol. 40, no. 13, pp. 4287–4299, 2022. DOI: 10.1109/JLT.2022.3164168.

[61] M. M. H. Adib, C. Füllner, H. Peng, C. Koos, W. Freude, and S. Randel, "Coherent time- and wavelength-division multiplexed point-to-multipoint optical access network using low-cost DFB lasers enabled by a frequency comb," *Opt. Express*, vol. 32, no. 22, pp. 38 516–38 530, Oct. 2024. DOI: 10.1364/OE.531344.

[62] B. Zhang, C. Malouin, and T. J. Schmidt, "Design of coherent receiver optical front end for unamplified applications," *Opt. Express*, vol. 20, no. 3, pp. 3225–3234, Jan. 2012. DOI: 10.1364/OE.20.003225.

[63] A. Awny et al., "A Linear Differential Transimpedance Amplifier for 100-Gb/s Integrated Coherent Optical Fiber Receivers," *IEEE Transactions on Microwave Theory and Techniques*, vol. 66, no. 2, pp. 973–986, 2018. DOI: 10.1109/TMTT.2017.2752170.

[64] G. Agrawal and N. Olsson, "Self-phase modulation and spectral broadening of optical pulses in semiconductor laser amplifiers," *IEEE Journal of Quantum Electronics*, vol. 25, no. 11, pp. 2297–2306, 1989. DOI: 10.1109/3.42059.

[65] R. Bonk et al., "Linear semiconductor optical amplifiers for amplification of advanced modulation formats," *Optics Express*, vol. 20, no. 9, pp. 9657–9672, 2012. DOI: 10.1364/OE.20.009657.

[66] R. Giller, R. Manning, and D. Cotter, "Gain and phase recovery of optically excited semiconductor optical amplifiers," *IEEE Photonics Technology Letters*, vol. 18, no. 9, pp. 1061–1063, 2006. DOI: 10.1109/LPT.2006.873474.

[67] J. Wang, A. Maitra, C. G. Poulton, W. Freude, and J. Leuthold, "Temporal Dynamics of the Alpha Factor in Semiconductor Optical Amplifiers," *Journal of Lightwave Technology*, vol. 25, no. 3, pp. 891–900, 2007. DOI: 10.1109/JLT.2006.890439.

[68] T. Vallaitis et al., "Slow and fast dynamics of gain and phase in a quantum dot semiconductor optical amplifier," *Opt. Express*, vol. 16, no. 1, pp. 170–178, Jan. 2008. DOI: 10.1364/OE.16.000170.

[69] I. Fatadin, S. J. Savory, and D. Ives, "Compensation of Quadrature Imbalance in an Optical QPSK Coherent Receiver," *IEEE Photonics Technology Letters*, vol. 20, no. 20, pp. 1733–1735, 2008. DOI: 10.1109/LPT.2008.2004630.

[70] A. Leven, N. Kaneda, U.-V. Koc, and Y.-K. Chen, "Frequency Estimation in Intradyne Reception," *IEEE Photonics Technology Letters*, vol. 19, no. 6, pp. 366–368, 2007. DOI: 10.1109/LPT.2007.891893.

[71] H. Wang et al., "Fast-Convergence Digital Signal Processing for Coherent PON Using Digital SCM," *Journal of Lightwave Technology*, vol. 41, no. 14, pp. 4635–4643, 2023. DOI: 10.1109/JLT.2023.3243828.

[72] M. J. Connelly, "Wideband SOA steady-state numerical model," *IEEE Journal of Quantum Electronics*, vol. 37, no. 3, pp. 439–447, 2001. DOI: 10.1109/3.910455.

[73] G. P. Agrawal and N. K. Dutta, *Semiconductor Lasers*, 2nd ed. New York: Springer, 1993, ISBN: 978-0442012053.

[74] N. K. Dutta and Q. Wang, *Semiconductor Optical Amplifiers*. Singapore: World Scientific, 2006, ISBN: 978-9812567750.

[75] K. Morito, "Output-Level Control of Semiconductor Optical Amplifier by External Light Injection," *Journal of Lightwave Technology*, vol. 23, no. 12, pp. 4332–4341, 2005. DOI: 10.1109/JLT.2005.858248.

[76] M. Lu et al., "Monolithic Integration of a High-Speed Widely Tunable Optical Coherent Receiver," *IEEE Photonics Technology Letters*, vol. 25, no. 11, pp. 1077–1080, 2013. DOI: 10.1109/LPT.2013.2259474.

[77] M. Anagnosti et al., "Record Gain x Bandwidth (6.1 THz) Monolithically Integrated SOA-UTC Photoreceiver for 100-Gbit/s Applications," *Journal of Lightwave Technology*, vol. 33, no. 6, pp. 1186–1190, 2015. DOI: 10.1109/JLT.2014.2372816.

[78] R. Borkowski et al., "Real-time burst-mode operation of an integrated SOA-PIN/TIA receiver for 25 Gbit/s/λ and faster T(W)DM-PON," in *2017 Optical Fiber Communications Conference and Exhibition (OFC)*, 2017, pp. 1–3.

[79] Y. Lei et al., "Monolithic integrated two-stage cascaded SOA-PIN receiver for high-speed optical wireless communication," *Opt. Lett.*, vol. 47, no. 10, pp. 2578–2581, May 2022. DOI: 10.1364/OL.457785.

[80] C. Caillaud et al., "High sensitivity 40 Gbit/s preamplified SOA-PIN/TIA receiver module for high speed PON," in *2014 The European Conference on Optical Communication (ECOC)*, 2014, pp. 1–3. DOI: 10.1109/ECOC.2014.6963903.

[81] M. L. Nielsen, L. Molle, T. Richter, and C. Schubert, "Feasibility study of SOA-preamplified coherent reception for 112 Gb/s DP-QPSK unamplified link," in *2013 Optical Fiber Communication Conference and Exposition and the National Fiber Optic Engineers Conference (OFC/NFOEC)*, 2013, pp. 1–3. DOI: 10.1364/NFOEC.2013.JTh2A.45.

[82] G. Santini et al., "High responsivity coherent photonic receiver integrating an SOA, a 90° hybrid, and high speed UTC photodiodes," *Opt. Express*, vol. 25, no. 21, pp. 25 719–25 724, Oct. 2017. DOI: 10.1364/OE.25.025719.

[83] H. Tang et al., "Semiconductor Optical Amplifiers with Wide Gain Bandwidth and Enhanced Polarization Insensitivity Based on Tensile-Strained Quantum Wells," *Sensors*, vol. 24, no. 11, p. 3285, 2024. DOI: 10.3390/s24113285.

[84] W. P. Wong and K. S. Chiang, "Design of Waveguide Structures for Polarization-Insensitive Optical Amplification," *IEEE Journal of Quantum Electronics*, vol. 36, no. 11, pp. 1243–1250, 2000. DOI: 10.1109/3.890264.

[85] M. Premaratne and G. P. Agrawal, *Semiconductor Optical Amplifiers*. Cambridge, UK: Cambridge University Press, 2011, ISBN: 9780521761891.

[86] C. Tombling, C. Michie, I. Andonovic, and A. E. Kelly, "Recent Advances in Semiconductor Optical Amplifiers," in *Proceedings of the Optical Fiber Communication Conference (OFC)*, Invited paper, Atlanta, USA: IEEE, 2003, pp. 892–893.

[87] A. Borghesani et al., "High Saturation Power (>16.5 dBm) and Low Noise Figure (<6 dB) Semiconductor Optical Amplifier for C-band Operation," in *Proceedings of the Optical Fiber Communication Conference (OFC)*, Atlanta, USA: IEEE, 2003, pp. 534–536.

[88] K. J. Kasunic, K. Tastavridis, C. N. Clark, M. Lestrade, A. Champagne, and R. Maciejko, "The Effects of Quantum-Well Number on Gain Crosstalk in Semiconductor Optical Amplifiers," *IEEE Journal of Quantum Electronics*, vol. 39, no. 7, pp. 897–902, 2003. DOI: 10.1109/JQE.2003.813193.

[89] B.-H. Choi and S. Soo Lee, "Input power dynamic range analysis of SOA and EDFA link extenders on TDM–PON systems without burst effect control," *Optics Communications*, vol. 286, pp. 187–191, 2013, ISSN: 0030-4018. DOI: https://doi.org/10.1016/j.optcom.2012.09.019.

[90] K. Sato and H. Toba, "Reduction of mode partition noise by using semiconductor optical amplifiers," *IEEE Journal of Selected Topics in Quantum Electronics*, vol. 7, no. 2, pp. 328–333, 2001. DOI: 10.1109/2944.954146.

[91] L. Xu, I. Glesk, D. Rand, V. Baby, and P. R. Prucnal, "Suppression of beating noise of narrow-linewidth erbium-doped fiber ring lasers by use of a semiconductor optical amplifier," *Opt. Lett.*, vol. 28, no. 10, pp. 780–782, May 2003. DOI: 10.1364/OL.28.000780.

[92] W. Mathlouthi, F. Vacondio, P. Lemieux, and L. A. Rusch, "SOA gain recovery wavelength dependence: simulation and measurement using a single-color pump-probe technique," *Opt. Express*, vol. 16, no. 25, pp. 20 656–20 665, Dec. 2008. DOI: 10.1364/OE.16.020656.

[93] K. Kuroda and Y. Yoshikuni, "Gain saturation and recovery of an erbiumdoped fiber amplifier measured by temporally resolved probe techniques," in *2016 21st OptoElectronics and Communications Conference (OECC) held jointly with 2016 International Conference on Photonics in Switching (PS)*, 2016, pp. 1–3.

[94] M. J. Connelly, *Semiconductor Optical Amplifiers*. Boston / Dordrecht / London: Kluwer International Publishing, 2002, ISBN: 0792376579, 9780792376576.

[95] R. J. Manning and D. A. O. Davies, "Three-wavelength device for all-optical signal processing," *Opt. Lett.*, vol. 19, no. 12, pp. 889–891, Jun. 1994. DOI: 10.1364/OL.19.000889.

[96] H. Friis, "Noise Figures of Radio Receivers," *Proceedings of the IRE*, vol. 32, no. 7, pp. 419–422, 1944. DOI: 10.1109/JRPROC.1944.232049.

[97] K. Carney, R. Maldonado-Basilio, S. Philippe, and P. Landais, "Noise controlled semiconductor optical amplifier based on lateral . . .," *Electronics Letters*, vol. 46, no. 18, 2010. DOI: 10.1049/el.2010.1978.

[98] R. Lennox, K. Carney, R. Maldonado-Basilio, S. Philippe, A. L. Bradley, and P. Landais, "Impact of bias current distribution on the noise figure and power saturation of a multicontact semiconductor optical amplifier," *Opt. Lett.*, vol. 36, no. 13, pp. 2521–2523, Jul. 2011. DOI: 10.1364/OL.36.002521.

[99] K. Obermann et al., "Noise characteristics of semiconductor-optical amplifiers used for wavelength conversion via cross-gain and cross-phase modulation," *IEEE*

Photonics Technology Letters, vol. 9, no. 3, pp. 312–314, 1997. DOI: 10.1109/68.556057.

[100] M. Fujiwara and R. Koma, "Long-Reach and High-Splitting-Ratio WDM/TDM-PON Systems Using Burst-Mode Automatic Gain Controlled SOAs," *Journal of Lightwave Technology*, vol. 34, no. 3, pp. 901–909, 2016. DOI: 10.1109/JLT.2015.2501432.

[101] N. Calabretta, W. Miao, K. Mekonnen, and K. Prifti, "SOA Based Photonic Integrated WDM Cross-Connects for Optical Metro-Access Networks," *Applied Sciences*, vol. 7, no. 9, 2017, ISSN: 2076-3417. DOI: 10.3390/app7090865.

[102] X. Xue and N. Calabretta, "Nanosecond optical switching and control system for data center networks," *Nature Communications*, vol. 13, 2022, ISSN: 2041-1723. DOI: 10.1038/s41467-022-29913-1.

[103] A. Sakaguchi et al., "Nonlinear feedforward enabling quantum computation," *Nature Communications*, vol. 14, 2023, ISSN: 2041-1723. DOI: 10.1038/s41467-023-39195-w.

[104] A. Troncoso-Costas, A. Sarmiento, M. Morant, A. Saleh, and I. T. Monroy, "SOA-Amplified 100 Gbit/s/λ PAM-8 WDM Transmission for Optical Access Networks," in *Proc. Optical Fiber Communication Conference (OFC)*, Optica Publishing Group, San Diego, CA, USA, 2023, Th2A.27. DOI: 10.1364/OFC.2023.Th2A.27.

[105] X. Xu, P. Girouard, M. P. Yankov, M. Galili, L. K. Oxenløwe, and P. Guan, "PAM8 WDM Transmission Based on a Single Time-Lens Source with Geometric Shaping," in *Proc. Optical Fiber Communication Conference (OFC)*, Optica Publishing Group, San Diego, CA, USA, 2023, Tu1H.2. DOI: 10.1364/OFC.2023.Tu1H.2.

[106] A. Martínez-Curipoma and F. Arévalo, "Performance Analysis of a 200 Gb/s PAM-4 / PAM-8 WDM-PON," *Journal of Optical Communications and Networking*, vol. 15, no. 8, pp. 599–608, 2023, Preprint available on ResearchGate: https://www.researchgate.net/publication/368837773. DOI: 10.1364/JOCN.2023.XXXXXX.

[107] J. Lu, C. Huang, T. Wang, Q. Li, and J. Xu, "High-speed PAM8 Silicon-Photonics IM-DD System with Neural-Network-Based Equalization," in *Proc. SPIE 13236, Silicon Photonics XVII*, 2024, 132360H. DOI: 10.1117/12.3036347.

[108] G. Huang, X. Liu, Y. Zhang, M. Zhu, and H. Li, "300-Gbit/s/λ 8-Level Pulse-Amplitude-Modulation (PAM8) Transmission Enabled by Deep-Learning Equalization," *Optics Communications*, vol. 553, p. 129 898, 2024. DOI: 10.1016/j.optcom.2023.129898.

[109] J. Justice, C. Bower, M. Meitl, M. B. Mooney, M. A. Gubbins, and B. Corbett, "Wafer-Scale Integration of Group III–V Lasers on Silicon Using Transfer Printing of Epitaxial Layers," *Nature Photonics*, vol. 6, pp. 610–614, 2012. DOI: 10.1038/nphoton.2012.187.

[110] Y. Shi et al., "Integration of III-V Lasers on Silicon Based on InP Quantum Dots," *Optica*, vol. 4, no. 12, pp. 1468–1473, 2017. DOI: 10.1364/OPTICA.4.001468.

[111] A. Rahim, T. Spuesens, R. Baets, and W. Bogaerts, "Open-Access Silicon Photonics: Current Status and Emerging Initiatives," *Proceedings of the IEEE*, vol. 106, no. 12, pp. 2313–2330, 2018. DOI: 10.1109/JPROC.2018.2873278.

[112] K. Van Gasse, R. Wang, and G. Roelkens, "III-V-on-Silicon High-Gain Semiconductor Optical Amplifiers for Microwave Photonics," *Optics Express*, vol. 27, no. 3, pp. 293–302, 2019. DOI: 10.1364/OE.27.000293.

[113] X. Sun, H. C. Liu, and A. Yariv, "Adiabaticity Criterion and the Shortest Adiabatic Mode Transformer in a Coupled-Waveguide System," *Optics Letters*, vol. 34, no. 3, pp. 280–282, 2009. DOI: 10.1364/OL.34.000280.

[114] G.-H. Duan et al., "Hybrid III-V on Silicon Lasers for Photonic Integrated Circuits on Silicon," *IEEE Journal of Selected Topics in Quantum Electronics*, vol. 20, no. 4, p. 158, 2014. DOI: 10.1109/JSTQE.2014.2313214.

[115] G. Roelkens, A. Abassi, P. Cardile, U. Dave, A. De Groote, Y. De Koninck, et al., "III–V-on-Silicon Photonic Devices for Optical Communication and Sensing," *Photonics*, vol. 2, no. 3, pp. 969–1004, 2015. DOI: 10.3390/photonics2030969.

[116] H. Park, A. W. Fang, O. Cohen, R. Jones, M. J. Paniccia, and J. E. Bowers, "A Hybrid AlGaInAs-Silicon Evanescent Amplifier," *IEEE Photonics Technology Letters*, vol. 19, no. 4, pp. 230–232, 2007. DOI: 10.1109/LPT.2006.891137.

[117] M. L. Davenport, S. Skendi, N. Volet, J. C. Hulme, M. J. R. Heck, and J. E. Bowers, "Heterogeneous Silicon Photonics for the Generation and Processing of Microwave Signals," *IEEE Journal of Selected Topics in Quantum Electronics*, vol. 22, no. 6, p. 78, 2016. DOI: 10.1109/JSTQE.2016.2598441.

[118] Q. Zhuge, "Cost-efficient architectures and signal processing for coherent PON systems," in *Proceedings of the European Conference on Optical Communication (ECOC)*, Dublin, Ireland, 2019.

[119] D. van Veen and V. Houtsma, "Strategies for economical next-generation 50G and 100G passive optical networks [Invited]," *Journal of Optical Communications and Networking*, vol. 12, no. 1, A95–A103, 2020. DOI: 10.1364/JOCN.12.000A95.

[120] D. van Veen and V. Houtsma, "Transceiver Technologies for Next-Generation PON (Tutorial)," in *2020 Optical Fiber Communications Conference and Exhibition (OFC)*, 2020, pp. 1–28.

[121] S. Sakano, T. Tsuchiya, M. Suzuki, S. Kitajima, and N. Chinone, "Tunable DFB laser with a striped thin-film heater," *IEEE Photonics Technology Letters*, vol. 4, no. 4, pp. 321–323, Apr. 1992.

[122] Y. Kotaki, S. Ogita, M. Matsude, Y. Kuwahara, and H. Ishikawa, "Tunable, narrow-linewidth and high-power lambda/4-shifted DFB laser," *Electronics Letters*, vol. 25, no. 15, pp. 990–992, 1989.

[123] G. Yoffe, S. Zou, S. Rishton, R. Olson, M. Emanuel, and B. Pezeshki, "Widely-tunable 30 mW laser source with sub-500 kHz linewidth using DFB array," in

Proceedings of the IEEE 21st Annual Meeting of the Lasers and Electro-Optics Society, 2008, pp. 892–893.

[124] V. Sales, J. Segarra, V. Polo, J. C. Velásquez, and J. Prat, "UDWDM-PON using low-cost coherent transceivers with limited tunability and heuristic DWA," *IEEE/OSA Journal of Optical Communications and Networking*, vol. 8, no. 8, pp. 582–599, Aug. 2016.

[125] Z. Xu et al., "High-speed WDM-PON using CW injection-locked Fabry-Pérot laser diodes," *Opt. Express*, vol. 15, no. 6, pp. 2953–2962, Mar. 2007. DOI: 10.1364/OE.15.002953.

[126] P. Healey et al., "Spectral slicing WDM-PON using wavelength-seeded reflective SOAs," *Electronics Letters*, vol. 37, no. 19, pp. 1181–1182, 2001. DOI: 10.1049/el:20010799.

[127] J. E. Simsarian, J. Gripp, S. Chandrasekhar, and P. Mitchell, "Fast-tuning coherent burst-mode receiver for metropolitan networks," *IEEE Photonics Technology Letters*, vol. 26, no. 8, pp. 813–816, Apr. 2014. DOI: 10.1109/LPT.2014.2306805.

[128] V. Torres-Company et al., "Laser Frequency Combs for Coherent Optical Communications," *Journal of Lightwave Technology*, vol. 37, no. 7, pp. 1663–1670, 2019. DOI: 10.1109/JLT.2019.2894170.

[129] J. Zhou, C. Li, H. Wang, Z. Liu, and C. Yu, "Burst-Mode Digital Signal Processing for Coherent Optical Time-Division Multiple Access," *arXiv preprint arXiv:2410.10080*, 2024, Coherent BM-DSP for CO-TDMA; addresses estimation of SOP, frequency offset, equalization for bursts.

[130] H. Wang et al., "Preamble Design and Burst-Mode DSP for Upstream Reception of 200G Coherent TDM-PON," *arXiv preprint arXiv:2405.19133*, 2024, Burst-mode DSP and preamble design for coherent TDM-PON upstream, including SOP and frequency estimation.

[131] J. Zhang, Z. Jia, M. Xu, H. Zhang, and L. A. Campos, "Efficient Preamble Design and Digital Signal Processing in Upstream Burst-Mode Detection of 100G TDM Coherent-PON," *Journal of Optical Communications and Networking*, vol. 13, no. 2, A135–A143, 2021, Burst-mode coherent PON detection requiring frame sync, polarization, and frequency DSP functions.

List of Publications

[A1] **F. Jamali**, S. L. Murphy, C. Antony, and P. D. Townsend, "SOA-Based Power Equalisation for 100 Gb/s Passive Optical Network," in *2023 Conference on Lasers and Electro-Optics Europe European Quantum Electronics Conference (CLEO/Europe-EQEC)*, 2023, pp. 1–1. DOI: 10.1109/CLEO/Europe-EQEC57999.2023.10231954.

[A2] **F. Jamali**, S. L. Murphy, C. Antony, and P. D. Townsend, "SOA-based optical burst power equalization for high-speed next generation passive optical networks," *Opt. Express*, vol. 33, no. 11, pp. 24 084–24 097, Jun. 2025. DOI: 10.1364/OE.561120.

[A3] S. Murphy, **F. Jamali**, P. D. Townsend, and C. Antony, "High Dynamic Range 100 Gbit/s PAM4 PON with SOA Preamplifier using Gated Recurrent Neural Network Equaliser," in *2022 European Conference on Optical Communication (ECOC)*, 2022, pp. 1–4.

[A4] S. L. Murphy, **F. Jamali**, P. D. Townsend, and C. Antony, "High Dynamic Range 100G PON Enabled by SOA Preamplifier and Recurrent Neural Networks," *Journal of Lightwave Technology*, vol. 41, no. 11, pp. 3522–3532, 2023. DOI: 10.1109/JLT.2023.3249046.

[A5] S. L. Murphy, **F. Jamali**, P. D. Townsend, and C. Antony, "Adaptive Neural Network Equalisation Using Skip Connections for Future 100 Gbit/s/λ Passive Optical Networks," in *European Conference on Optical Communications*, Optica Publishing Group, 2023.

[A6] E. Roshanshomal, S. L. Murphy, S. O. Ayat, **F. Jamali**, P. D. Townsend, and C. Antony, "Low-Complexity FPGA-Accelerated NN-Based Adaptive Equalizer for 100 Gb/s IMDD PON," in *2025 IEEE International Conference on Machine Learning for Communication and Networking (ICMLCN)*, 2025, pp. 1–5. DOI: 10.1109/ICMLCN64995.2025.11140557.